MICCAI 2019 Workshop Proceedings

Computational Biomechanics for Medicine XIV

Karol Miller, Grand Joldes, Martyn Nash, Poul M.F. Nielsen, Adam Wittek

http://cbm.mech.uwa.edu.au/CBM2019

MICCAI

Preface:

Computational Biomechanics for Medicine Workshop series was established in 2006 with the first meeting held in Copenhagen. The fourteenth (CBM XIV) workshop was held in conjunction with the Medical Image Computing and Computer Assisted Intervention Conference (MICCAI 2019) in Shenzhen on 13 October 2019. It provided an opportunity for specialists in a wide area of computational sciences to present and exchange opinions and ideas on the possibilities of applying their techniques to computer- integrated medicine.

Computational Biomechanics for Medicine XIV proceedings are organized into two parts: 1) "Computational Solid Mechanics" and 2) "Topics in patient-specific computations". Some of the interesting topics discussed include application of advanced computational methods in the following areas:

- Medical image analysis;
- Image-guided surgery;
- Surgical intervention planning;
- Disease prognosis and diagnosis;
- Cell biomechanics;
- Soft tissue biomechanics;
- Injury mechanism analysis

After rigorous review of full manuscripts we accepted seven papers, collected in this volume.

Information about Computational Biomechanics for Medicine Workshops, including Proceedings of the previous meetings is available at http://cbm.mech.uwa.edu.au/.

We would like to thank the MICCAI 2019 organizers for help with administering the Workshop, invited lecturers for deep insights into their research fields, the authors for submitting high quality work, and the reviewers for helping with paper selection.

Karol Miller, Perth, WA, Australia
Adam Wittek, Perth, WA, Australia
Grand Joldes, Perth, WA, Australia
Martyn Nash, Auckland, New Zealand
Poul M.F. Nielsen, Auckland, New Zealand

Contents:

Keynote

1. What has image-based modelling of cerebrospinal fluid flow in chiari malformation taught us about syringomyelia mechanisms? V

Lynne Bilston, Sydney, Australia

Part 1: Computational Solid Mechanics

2. Lung Tumour Tracking Based on Patient-Specific Biomechanical Model of the Respiratory System.

Hamid Ladjal, Lyon, France

3. Simulation of soft tissue deformation in real-time using domain decomposition.

Ryadh Hafessas, Strasbourg, France

4. Design of Auxetic Coronary Stents by Topology Optimization.

Zhen Luo, Sydney, Australia

5. Physics-based Deep Neural Network for Real-Time Lesion Tracking in Ultrasound-guided Breast Biopsy.

Andrea Mendizabal, Strasbourg, France

Part 2: Topics in patient-specific computations

6. Towards Visualising and Understanding Patient-Specific Biomechanics of Abdominal Aortic Aneurysms.

Kiara Beinart, Perth, Australia

7. Pipeline for 3D reconstruction of lung surfaces using intrinsic features under pressure-controlled ventilation.

Samuel Richardson, Auckland, New Zealand

8. A Flux-Conservative Finite Difference Scheme for Anisotropic Bioelectric Problems.
   George Bourantas, Perth, Australia

Keynote

What has image based modelling of cerebrospinal fluid flow in Chiari Malformation taught us about syringomyelia mechanisms?

Lynne E Bilston

Neuroscience Research Australia and Prince of Wales Clinical School, UNSW

Abstract

Chiari Malformation is a congenital disorder of the hindbrain, in which the cerebellar tonsils protrude through the foramen magnum, impeding normal cerebrospinal fluid (CSF) flow into the spinal canal. It is associated with pain, dizziness and headaches, particularly related to coughing and straining. The mechanisms by which Chiari malformation gives rise to these symptoms are not understood. In a large proportion of patients, a fluid-filled cavity develops in the spinal cord, called a syrinx. Syrinxes can cause additional neurological deficits, including sensory changes, weakness and upper limb pain. Syrinxes are associated with disturbances to normal CSF dynamics, usually as a result of obstructions in the spinal canal, but precisely how this occurs is not known. Animal studies suggest that fluid transport into the spinal cord is increased in the presence of spinal canal obstructions, likely via annular spaces surrounding penetrating arteries (perivascular spaces). Human phase contrast magnetic resonance imaging studies can quantify both cardiac driven motion of cerebrospinal fluid flow, and, more recently, respiratory and other influences. These data can be used to generate subject-specific computational fluid dynamics models of the hindbrain and spinal canal to estimate spinal canal pressure dynamics in patients with Chiari malformation, patients with syrinxes, and healthy controls. Computational models of perivascular space flow can be linked to these macroscopic models, to enable investigation of the feasibility of hypotheses about mechanisms of syrinx formation. To date, these studies have demonstrated that several popular hypotheses about Chiari mechanisms and syrinx formation are inconsistent with the mechanics of CSF flow, and generated novel mechanistic hypotheses. Subject-specific image based modelling provide a useful adjunct to human and animal experimental research into CSF flow disorders such as Chiari malformation and syringomyelia.

Part 1.

Computational Solid Mechanics

Lung Tumor Tracking Based on Patient-Specific Biomechanical Model of the Respiratory System

Hamid Ladjal, Michael Beuve and Behzad Shariat

1 Introduction

Organ motion due to patient breathing introduces a technical challenge for dosimetry and lung tumor treatment by radiation therapy. Accurate dose distribution estimation requires patient-specific information on tumor position, size and shape as well as information regarding the material density and stopping power of the media along the beam path. In order to calculate and to ensure sufficient dose coverage throughout the treatment, the internal margin (IM) and setup margin (SM) are added to the clinical target volume (CTV) to compensate for the breathing movement and to obtain target volume (PTV). Generally, the addition of different margins leads to an excessively large PTV that would go beyond the patient's tolerance, and does not reflect the actual clinical consequences [1]. In the case of moving tumors, the PTV is increased so that the tumor lies inside the treatment field at all times. Breathing is an active and a complex process where the respiratory motion is non-reproducible, and the breathing periodicity, amplitude and motion path of patients' organs are observed during the respiration [2, 3]. Various different types of correspondence models that have been used and developed in the literature (linear, piece-wise linear, polynomial, B-spline, neural networks, etc.) in order to correlate the internal motion to respiratory surrogate signals. For more information on the correspondence models please see the complete review in chapter III of Ehrhardt Lorenz 2013 [3].
The biomechanical approaches aim at identification and taking into account the different anatomical and physiological aspects of breathing dynamics. These approaches attempt to describe respiratory-induced organ motion through a mathematical formulation based on continuum media mechanics solved generally on Finite Element Meth-

Hamid Ladjal, and Behzad Shariat are at LIRIS, Laboratoire d'InfoRmatique en Image et Systs d'information CNRS UMR 5205, University of Lyon, Université Claude Bernard Lyon 1.
Hamid Ladjal and Michael Beuve are at IPNL CNRS UMR 5822, F-69622, University of Lyon, Université Claude Bernard Lyon 1, France
e-mail: hamid.ladjal@liris.cnrs.fr
e-mail: hamid.ladjal@univ-lyon1.fr

ods (FEM) [4, 5, 6]. Unfortunately, most of the time, the authors have used a single organ (lung) with nonrealistic of boundary conditions, or the lung motion is simulated by using simple displacement boundary conditions which are not realistic and do not take into account the real physiological respiratory dynamics. However, in [7] the authors present an ad-hoc evolutionary algorithm designed to explore a search space with 15 dimensions for the respiratory system including different organs. The method tries to estimate the parameters of a complex organ behavior model (15 parameters). The authors in [8] have proposed a FE model of the lung motion using a generic pressure-volume curve, which is not patient specific. Recently, the authors in [9] have proposed patient specific biomechanical model of the lung motion from 4D CT images for half respiratory cycle, where the motion is not constrained by any fixed boundary condition. The authors have used 4 and 16 pressure zones on the sub-diaphragm and thoracic cavity, respectively. Unfortunately, none of these methods take into account the real physiological respiratory properties, and are not able (or difficult) to be controlled or monitored by the external parameters. In this chapter, we evaluate the 3D tumor trajectories from patient-specific biomechanical models of the respiratory system for a whole respiratory cycle, based on personalized physiological pressure-volume curve [10]. This model has coupled an automatic tuning algorithm to calculate the personalized lung pressure and diaphragm force parameters .

2 MATERIALS AND METHODS

2.1 Anatomy and physiology of the respiratory system

The lung is a passive organ which is divided into two halves, the right and left lung. It is situated in the thorax on either side of the heart. The pleural cavity is surrounded by the the chest wall on the sides, and the diaphragm on the bottom. This space contains pleural fluid which facilitates near frictionless sliding at this boundary. The diaphragm is a dome-shaped musculofibrous membrane concave toward the lungs which separates the thorax from the abdominal cavity (Fig.1). It is composed of a peripheral part (muscular fibre) and a central part (tendon). Lungs are linked to the diaphragm and to the ribs through the pleura. The mechanics of human breathing involves two steps that alternate with each other: inhalation (inspiration) and exhalation (expiration). Negative pressure in the pleural cavity (natural breathing) initiates when the diaphragm and chest wall move away from the lung. The negative pressure expands lung volume, dropping the internal lung pressure, allowing air to enter passively in the lung. The ability of the lungs to expand is expressed by using a measure known as the lung compliance. Lung compliance is the relationship between how much pressure is required to produce a degree of volume change of the lungs. It is affected by the elastic properties of the lung. The pulmonary compliance therefore reflects the lungs ability to develop in response to an increase in pressure.

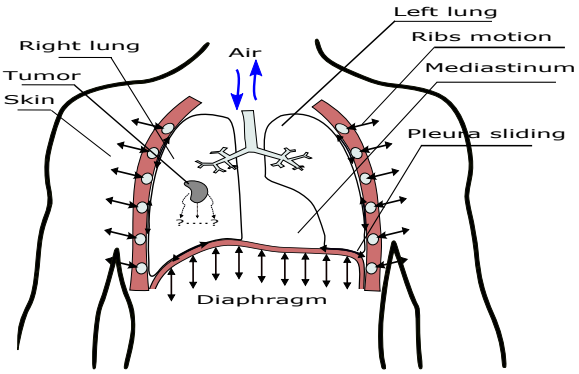

Fig. 1 Respiratory mechanics: the role of the diaphragm and thorax in breathing.

2.2 3D Segmentation and CAD reconstruction

Biomechanical modeling of the respiratory system necessitates the geometrical modeling of involved organs. For this purpose a correct segmentation of organs on CT images is necessary. Various approaches for multi-organ and lung segmentation have been developed based on CT images, which include gray-level thresholding, region growing, edge tracking. In this paper, the thorax, the lungs and the external skin are segmented automatically using gray-level thresholds algorithms available within ITK-SNAP library[1]. Automatic segmentation of the diaphragm is difficult due the lack of image contrast of the diaphragm with its surrounding organs as well as the respiration-induced motion artifacts in 4D CT images. The diaphragms were manually segmented within ITK-SNAP [11, 12]. In order to extract the mediastinum structure, we have used the different segmentation masks of the lungs, thorax, the inner thoracic region and the diaphragm. The accurate segmentation of lung tumors remains quite challenging, and the correct segmentation can only be achieved by medical experts.
After segmentation, a 3D surface mesh and a CAD-based approach has been developed. The organs shape are reconstructed as a solid using non-uniform rational B-spline (NURBS) curves. Using the resulting smooth surface, a quality mesh using a first-order tetrahedra elements (C3D4) is generated using Abaqus packages (Fig.2).

2.3 Biomechanical patient-specific model of the respiratory system

The organs are considered as isotropic, elastic and hyperelastic materials. For an isotropic elastic or hyperelastic material, the elastic energy, denoted W, may be written as:

[1] ITK-SNAP is a software application used to segment structures in 3D medical images

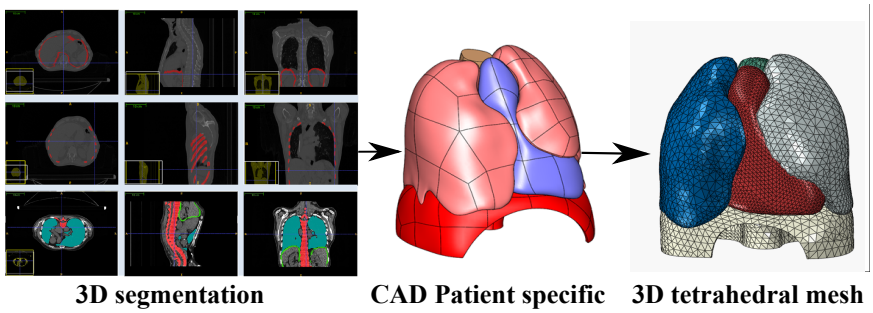

Fig. 2 3D Segmentation, CAD reconstruction and 3D mesh patient specific adapted for finite element simulation.

$$W(\mathbf{E}) = \frac{\lambda}{2}(tr\,\mathbf{E})^2 + \mu\,(tr\,\mathbf{E}^2) \tag{1}$$

where $\mathbf{E}$ is the Green-Lagrange strain tensor, λ and μ are the Lame coefficients. The Lame coefficients can be written in terms of Young's modulus, E, and Poisson's ratio, ν.

$$\mu = \frac{E}{2(1+\nu)} \qquad \lambda = \nu\frac{E}{(1-2\nu)(1+\nu)} \tag{2}$$

The second Piola-Kirchhoff stress tensor and the Green-Lagrange strain tensor given by:

$$\mathbf{S} = \lambda\,(tr\,\mathbf{E})\,\mathbf{I} + 2\,\mu\,\mathbf{E} \tag{3}$$

For dynamic simulation using FEM, the equation of motion of a vertex l of the organ mesh can be written:

$$M^l\{\ddot{\mathbf{u}}_l\} + \gamma^l\{\dot{\mathbf{u}}_l\} + \sum_{\tau\in\nu_l}\left(\{\mathbf{F}_l^{int}\}\right) = \left\{\mathbf{F}_{ext}^l\right\} \tag{4}$$

Where M^l, γ^l are respectively the mass and damping coefficients of each vertex. The ν_l is the neighborhood of vertex l (i.e. the tetrahedra containing node l). To solve the dynamic system, we have chosen the implicit finite difference scheme in time for more stability.

In our simulation, the mass density of each tissue is patient-specific, calculated and determined directly from CT scan images, based on the density mapping algorithm defined and developed in our previous works [14]: First, organs tetrahedral meshes are generated from segmented CT scanner images. Next, the Hounsfield values issued from CT scanner images are converted into density values that are mapped to the node of the mesh, respecting the principles of mass conservation(Fig.3). For more information related to density mapping algorithm, one may refer to [13, 14].

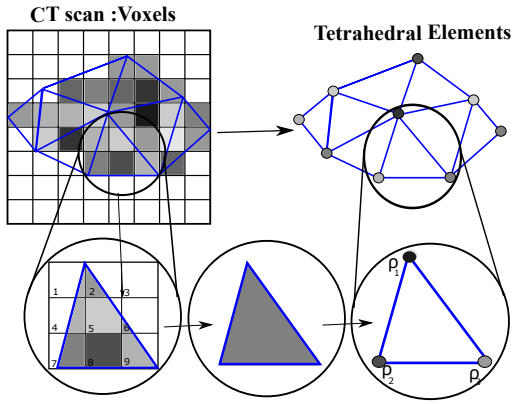

Fig. 3 Tetrahedral density map generation.The mass of a tetrahedral element equals the sum of the masses of volumes of intersection between the tetrahedron and the grid of voxels: $m(T_k) = m(I_k^1) + m(I_k^2) + m(I_k^4) + m(I_k^5) + m(I_k^6) + m(I_k^8) + m(I_k^9)$.

2.4 The boundary conditions

The developed biomechanical respiratory model is monitored directly by simulated actions of the breathing muscles; the diaphragm and the intercostal muscles/the rib cage. For the diaphragm, we have applied the radial direction of muscle forces, which corresponds anatomically to the direction of muscle fibers. The pressure is applied on the muscular part of the diaphragm and a simple homogeneous Dirichlet boundary conditions is applied in the lower part of the diaphragm and the Lagrange multiplier's method used for the contact model. In order to simulate the sliding of the lungs, a surface-to-surface contact model is applied on the lung-chest cavity, as well as lung-diaphragm cavity. The frictionless contact surfaces are used to simulate the pleural fluid behavior.

In our previous works [15, 11, 12], we have presented a methodology to study rib kinematics, using the finite helical axis method, where ribs could be considered as rigid bodies compared to other surrounding anatomical elements. The idea is to predict, from the transformation parameters, the rib positions and orientation at any time. Each rib transformation parameter is automatically computed between the initial and final states (Fig.4). Then, we have applied a linear interpolation of the transformation to predict the rib motion at any intermediate breathing states. For more details about finite helical axis method, one can refer to [15].

In this work, the amplitude of the lung pressure and diaphragm force are patient specific, they are determined at different respiratory states by an optimization framework based on inverse finite element method [10]. The model is controlled by personalized pressure-volume curves (semi-static compliance), calculated by $C_{ss} = \frac{3(1-2\nu)}{E V_{t-1}}$ at different states. Where E, ν, V_{t-1} are Young's modulus, Poisson's ratio and lung volume at step $t-1$ respectively. The mechanical properties and behaviors of the different organs used in our simulations are settled in the Table.1.

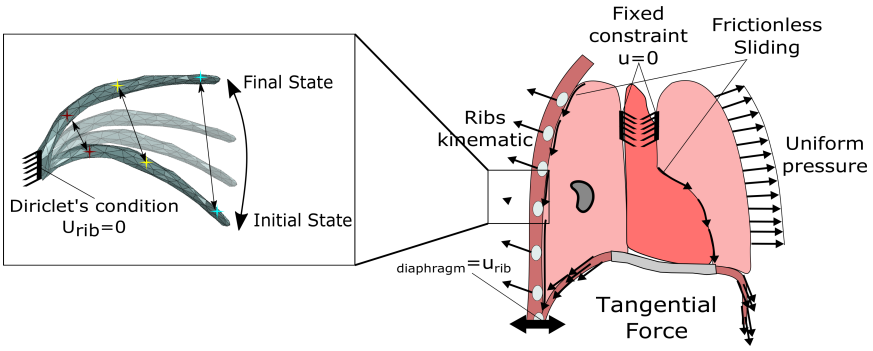

Fig. 4 The boundary conditions (BC) of our patient specific biomechanical model of the respiratory system.

Table 1 Mechanical properties of breathing system: LE Linear Elastic, HVSK Hyperelastic Saint Venant Kirchhoff, E Young's modulus, ν Poisson's ratio, ρ volumetric density [11, 12, 10]

Tissues	Mechanical behavior	E (MPa)	ν	ρ (kg/m^3)
Lungs	HSVK	$3.74 * 10^{-3}$	0.3	$3 * 10^2$
Lung tumor	LE	49	0.4	$1.5 * 10^3$
Mediastinum	LE	$5.87 * 10^{-3}$	0.4	$1 * 10^2$
Diaphragm muscle	HSVK	5.32	0.33	$1 * 0^3$
Diaphragm tendon	LE	33	0.33	$1 * 0^3$
Ribs	LE	5000	0.3	$1.5 * 0^3$
Cartilage	LE	49	0.3	$1 * 0^3$
Body of sternum	LE	11500	0.3	$1.5 * 0^3$
Thoracic vertebra	LE	9860	0.3	$1.5 * 0^3$
Flesh	LE	5.32	0.4	$1 * 0^6$

3 Results and experimental validation

Patients	Mean ± SD (mm)					Mean	Amplitude
	T10	T20	T30	T40	T50	All states	
Patient 1	2,0 ± 1,5	2,1 ± 1,2	2,1 ± 1,5	1,6 ± 1,3	1,2 ± 0,8	1,7± 1,3	10.9 (mm)
Patient 10	2,1 ± 1,5	2,2 ± 1,2	2,1 ± 1,6	1.6 ± 1,5	1.1 ± 0.8	1.8±1.3	26,06 (mm)

Table 2 Average landmark lung error (mm) during exhalation at different respiratory states: the first state T00, the end inspiration (T50), the end expiration (T10)

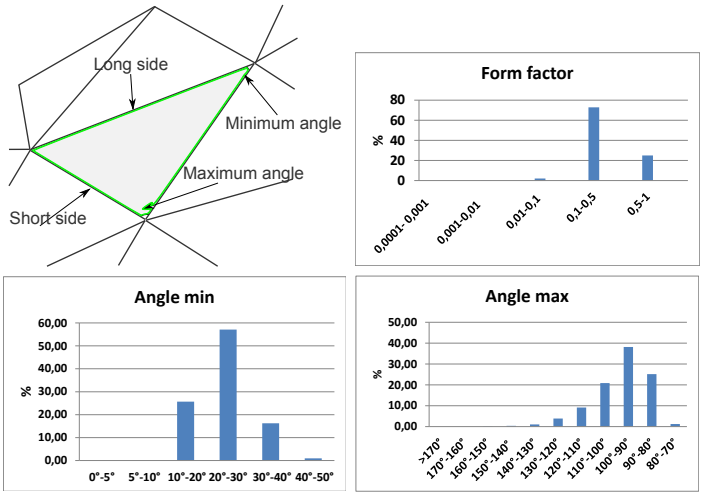

Fig. 5 Some criteria of mesh quality of tetrahedral elements. The triangular mesh element showing the longest side, shortest side, maximum interior angle and the minimum interior angle.

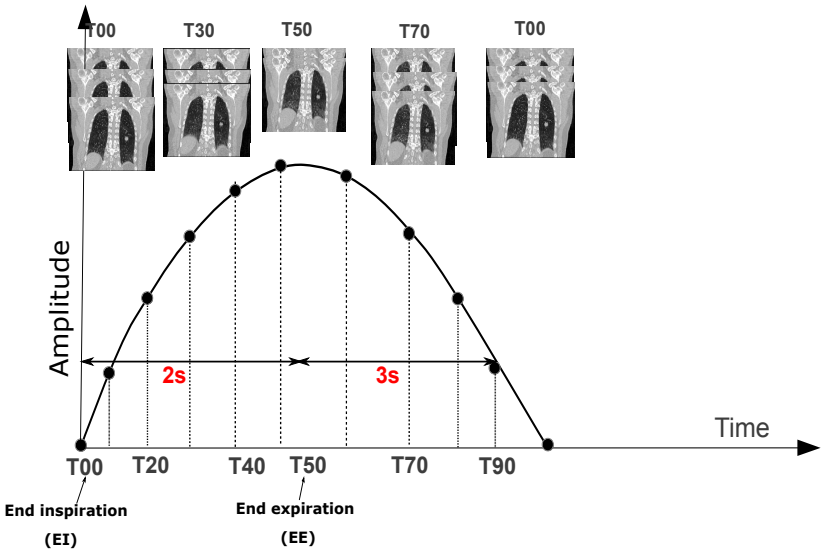

Fig. 6 Lung deformations during the full breathing cycle and intermediate states (10 states). Image slices of a patient case are taken from the DIR-lab data base [16]. The curve is only for illustration purposes .

3.1 Mesh quality

The quality of the mesh plays a significant role in the accuracy and stability of the numerical computation. In our simulation, we have used the linear tetrahedral continuum

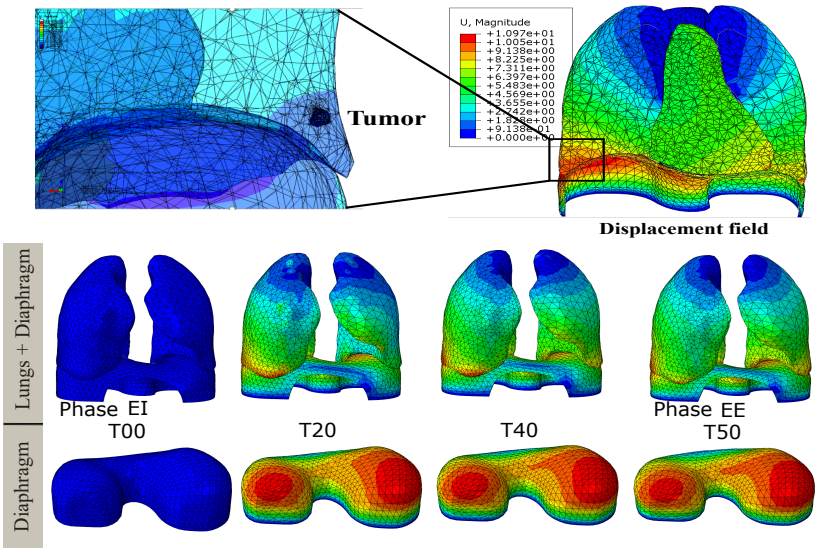

Fig. 7 Qualitative analysis of patient specific biomechanical simulation; lungs and diaphragm deformations from the end inhalation (EI) to end exhalation (EE), T00, T20, T40 and T50 are the intermediate states of the respiration between the EI to EE.

elements (C3D4). These elements permit mesh refinement around areas of high stress concentration. By default, poor quality elements are those that fulfill one or several of the following criteria: jacobian greater than 0.6, ratio of the maximum side length to the minimum side length larger than 10, the shape factor ranges from 0 to 1, minimum interior angle smaller than 20 degrees, and maximum interior angle larger than 120 degrees.

In this chapter, the mesh quality Fig.5 is performed using Abaqus packages. The above criteria for these elements are: $97,83\%$ of the elements with shape factor $(\frac{EV}{OEV})^2$ between 0.1 and 1, $82,95\%$ elements with minimum angle≥ 20, $99,5\%$ with maximum angle ≤ 140, $95,9\%$ with minimum length edge $\geq 3mm$, $99,1\%$ with maximum length edge $\leq 15mm$. From DIR-Lab Dataset [16], we have evaluated the motion estimation accuracy on two selected patients, with small and large breathing amplitudes (Patient1 = 10.9 mm, Patient10 = 26.06mm). In our finite element simulation, we simulate the full breathing cycle, including 10 intermediate states(see Fig.6). We define the simulation time for the inspiration phase is 2 seconds and for the expiration phase is 3 seconds. The Fig.7 shows the displacement field of the lungs and diaphragm during breathing. For the diaphragm, we can observe the maximum displacement on the right-posterior (RP) and left-posterior (LP) sides. It is also possible to notice a slightly larger (RP) side motion than (LP) side motion, according to the physiological anatomy. For the lungs deformation, the maximum displacement occurring in the posterior region

[2] EV: element volume and OEV: Optimal element volume is the volume of an equilateral tetrahedron with the same circumradius as the element. (The circumradius is the radius of the sphere passing through the four vertices of the tetrahedron.)

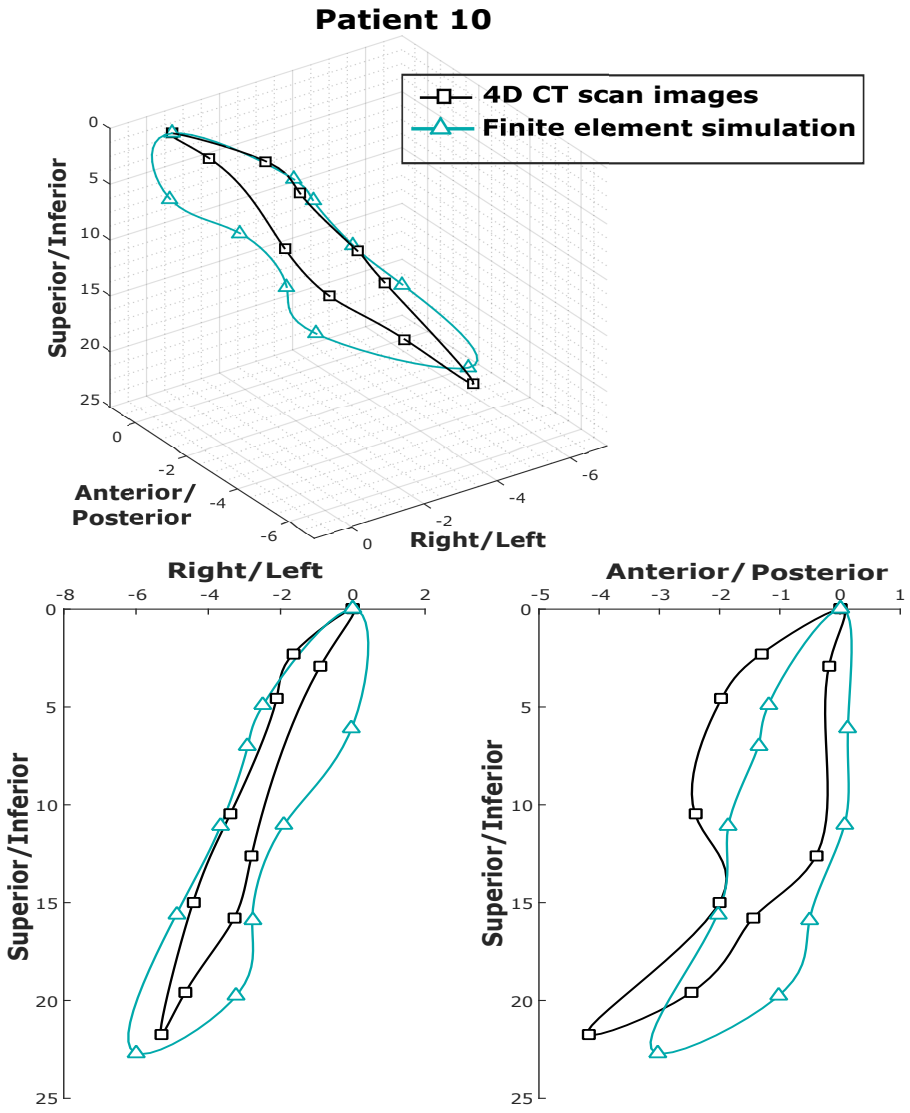

Fig. 8 3D lung tumor trajectory (in mm) issued from 4D CT scan images compared to the trajectory calculated by biomechanical finite element model including rib kinematics for patient P10 from DirLab data set [16].

along the superior-inferior (SI) direction (diaphragm direction).
Preliminary study was conducted to verify the efficiency of the developed finite element model and to evaluate lung tumor motion during full breathing cycle. In this order, the 3D lung tumor trajectories identified from 4D CT scan images were used

as reference and compared with the 3D lung tumor trajectories estimated from finite element simulation during the whole cycle of breathing (10 phases between the EI and EE). The accuracy of the proposed tumor tracking method is evaluated by comparing and calculating the average Euclidean distance between the 3D mesh surface of the segmented tumor and predicted FE lung tumor. The Fig.8 shows a comparison study between the hysteresis trajectories of the lung tumor during the whole cycle of the breathing compared to the trajectory calculated directly from 4D CT images. The results illustrate that our patient specific biomechanical model for tumor lung tracking is accurate and the average mean error is less than $1.8 \pm 1.3mm$.

4 Discussion and conclusion

In this research work, we have developed a patient specific biomechanical model of the respiratory system for lung tumor tracking for the whole respiratory cycle. Our preliminary results are quite realistic compared to the 4D CT scan images. This could be a potential tool to provide valuable tumor motion information for physician to reduce the margins between clinical target volume (CTV) and planning target volume (PTV). One of the limitations of our work that the multiple organ shape reconstruction is time consuming and manual operations for each patient. In order to avoid manual contouring and 3D geometry segmentation for different organs, and to reduce the computational costs without lowering the quality, we plan to develop and use a realistic atlas-based 3D shape reconstruction of the respiratory system based on statistical training or machine learning, to get a fast and automatic patient-specific model. Also, the use of few patients is another limitation of the presented work. Future work could investigate more patients from DirLab data set [16] or other data bases. Currently, we are working on the optimization of our model. The goal is to produce a novel 4D computational patient specific model using non-invasive surrogates to predict and to monitor lung tumor motion during the treatment.

Acknowledgements This research is supported by the LABEX PRIMES (ANR-11-LABX-0063), within the program Investissements dAvenir(ANR-11-IDEX- 0007) operated by the French National Research Agency (ANR) and by France Hadron.

References

1. ICRU 50 Prescribing, Recording, and Reporting Photon Beam Therapy (ICRU Report, Technical Report vol 50) (Bethesda, MD: International Commission on Radiation Units and Measurements), 1993.
2. H. Shirato et al, 'Speed and amplitude of lung tumor motion precisely detected in four-dimensional setup and in real-time tumor-tracking radiotherapy'. Int. J. Rad Onco Biol. Phys. 64(4): 1229-1236,2006.
3. J. Ehrhardt, C.Lorenz, 4D Modeling and Estimation of Respiratory Motion for Radiation Therapy, Springer, ISBN 978-3-642-36441-9, 2013.

4. M. Behr, J. Ps, M. Llari, Y. Godio, Y. Jammes, C. Brunet, 'A three-dimensional human trunk model for the analysis of respiratory mechanics', Journal of biomechanical engineering 132, 014501-1-014501-4, 2010.
5. M. Pato et al, 'Finite element studies of the mechanical behaviour of the diaphragm in normal and pathological cases', CMBBE 14(6), 505-513, 2011.
6. A. Al-Mayah , J. Moseley , M. Velec, K. Brock , Toward efficient biomechanical-based deformable image registration of lungs for imageguided radiotherapy, Phys. Med. Biol. volume 56, number 15, 56 4701, 2011.
7. F. Vidal, P-F. Villard, E. Lutton. Tuning of patient specific deformable models using an adaptive evolutionary optimization strategy. IEEE Transactions on Biomedical Engineering, 59 (10), pp.2942 - 2949. 2012.
8. J. Eom et al, Predictive modelling of lung motion over the entire respiratory cycle using measured pressure-volume data, 4DCT images, and finite-element analysis. Medical physics, vol. 37, no. 8, pages 4389-4400, 2010.
9. B. Fuerst, T. Mansi, F. Carnis, M. Saelzle, T. Zhang, J. Declerck, T. Boettger, J. Bayouth, N. Navab, A. Kamen Patient-Specific Biomechanical Model for the Prediction of Lung Motion from 4D CT Images, IEEE Transactions on Medical Imaging, Volume:34 Issue:2, pp 599 - 607, 2015.
10. M. Giroux, H. Ladjal, M. Beuve, B. Shariat Biomechanical Patient-Specific Model of the Respiratory System Based on 4D CT Scans and Controlled by Personalized Physiological . Medical Image Computing and Computer Assisted Intervention - MICCAI 2017 - 20th International Conference, Quebec (Canada), pp. 216-223, 13 septembre 2017.
11. H. Ladjal, B. Shariat, J. Azencot, M. Beuve, Appropriate Biomechanics and kinematics Modeling of the respiratory System: Human Diaphragm and Thorax. IEEE IROS 2013.
12. H. Ladjal, J, Azencot, M. Beuve, P.Giraud, J.M. Moreau, B. Shariat ,Biomechanical Modeling of the Respiratory System: Human Diaphragm and Thorax, Computational Biomechanics for Medicine New Approaches and New Applications, p101-115, 15p, 2015.
13. P. Manescu, H. Ladjal, J. Azencot, M. Beuve and B. Shariat, Human liver multiphysics modeling for 4d dosimetry during hadrontherapy, in IEEE 10th International Symposium on Biomedical Imaging (ISBI), pp. 472-475, 2013.
14. P. Manescu, H. Ladjal, J. Azencot, M. Beuve, E. Testa and B. Shariat and Behzad Shariat, Four-dimensional radiotherapeutic dose calculation using biomechanical respiratory motion description, International Journal of Computer Assisted Radiology and Surgery pp. 1-9, 2013.
15. A.L. Didier, P.F. Villard, J.Saade, J.M. Moreau, M. Beuve, B. Shariat, A chest wall model based on rib kinematics, in 'IEEE ICV, pp. 159-164, 2009.
16. Castillo E, et al, Four-dimensional deformable image registration using trajectory modeling. Phys Med Biol 55 305-327, (2009).

Simulation of soft tissue deformation in real-time using domain decomposition

Ryadh Hafessas[1], Pierre-Henri Tournier[2], and Frédéric Nataf[2] Stéphane Cotin[1]

[1] INRIA France
{ryadh.haferssas,stephane.cotin}@inria.fr
[2] Sorbonne Université
{frederic.nataf,tournier}@sorbonne-universite.fr

Abstract. Non-linear models used in dynamic simulations usually require the solution of multiple large and sparse linear systems in a successive manner. In this paper, we conduct a study of numerical solvers in the framework of real-time soft tissue deformation. Domain Decomposition paradigm has the potential of providing parallelism at both levels of equation assembling and linear system solving. In our case domain decomposition is employed to solve a non-linear model in a dynamic simulation in order to meet real-time computation by using parallel architecture. Numerical test on liver deformations using a non-linear deformation model is presented to evaluate the acceleration impact of the domain decomposition paradigm. Performances tests clearly show the efficiency of using a domain decomposition approach for real-time feedback.

Keywords: soft tissue deformation · non-linear model · linear systems · domain decomposition

1 Introduction

Image-guided therapy has revolutionized medicine, in its ability to provide care that is both efficient and effective. However, images acquired during an intervention are either incomplete, under-exploited, or can induce adverse outcomes. This can be due, for instance, to the lack of dimensionality of X-ray images and the associated radiation exposure for the patient. In the same time, the scientific computing community developed a particular interest in medical models which attempt to provide numerical simulation to reproduce living anatomy or physiology of the specific patient. The main challenge is to combine numerical models with data extracted from intra-operative images and deliver efficient per-operative guidance to clinicians.

In this paper, we are mainly interested in the simulation of soft tissue, in the context described above. Whether we consider augmented reality or simply real-time elastic registration, the constraints are similar. Models that aim to mimic the mechanical behavior of complex anatomical structures must be accurate enough to predict the location of internal structures invisible in the intra-operative image

while providing visual feedback in real-time. This makes the rise of simulation constraints at several levels: mechanical modeling, equation discretization, and linear solvers. As a result, any simulation attempt would be necessarily looking for the best compromise between accuracy and computation time. At the mechanical level, there are several instances in the literature of real-time simulation of deformable object which rely on linear elasticity like in [3]. The first limitation is inherent to the small strain assumption: to keep a linear model, the magnitude of deformation must be very small. Non-linear models do not suffer from this constraint but they introduce an extra computational cost. At the time discretization level, one of the most known strategies to deal with real-time computation of the liver tissue deformations is based on an explicit integration scheme, as proposed in [14, 13]. Explicit integration methods are particularly well suited for some applications like the real-time non-rigid registration of the brain shift during surgery [9]. However, liver tissues are often very soft, but in most of the pathologic cases, these tissues are much stiffer. That makes the critical time step very small (about $10^{-6} sec$) which would not correspond to the real dynamics. Implicit integration allows the use of larger time steps (about $2 \cdot 10^{-2}$ sec) without any stability issues. The counterpart is a heavier computation at each time step.

In practice, implicit integration schemes require to solve large systems of linear or non-linear equations. In both cases, we need to use a solver of linear systems in a successive manner to compute a solution that represents the state of the simulated model. The computation time of this part is the most important fold of the overall simulation computation time. The main interest which has driven our work in this paper is the efficiency in solving a large algebraic linear system in parallel computation. During these last few years, the computational power available within the hardware of computers is evolving in a different way. Due to frequency and heat-dissipation limits, the current trend is focused on increasing the number of computation units rather than their individual speed. Nowadays, one or two quadcore processors can be found in standard desktop computers. Two families of methods are traditionally used to solve a large linear system arising from discretization of mechanical models on a parallel machine: direct and iterative solvers. Direct solvers are known to be very robust. However, the memory requirement becomes significant with larger systems. On the other hand, iterative solvers [15] e.g., GMRES, CG, are less memory consuming and naturally parallel but they suffer from a lack of robustness. Domain Decomposition method [19, 4] as well as multigrid [8] method are hybrid methods that can take advantage of direct solvers and iterative solvers in the same algorithm. These two groups of approaches are described as hybrid methods because they are ultimately used as a preconditioner for the linear system during an iterative method, but direct methods are also used within the definition of the global preconditioner on some smaller subsystems or auxiliary problems. Such a hybridization provides highly concurrent methods that are robust enough to solve complex real-life problems [12, 6, 18].

In this paper, we aim to assess and achieve performance gain in a typical case of liver deformation simulation using a non-linear model with implicit integration scheme. To this end, we propose to adopt a domain decomposition paradigm that introduces parallelism at two different levels, first at the model assembling then at equation solves. Such a strategy opens new opportunities to deal with accurate real-time simulations of soft organs, in particular in the context of complex interactions.

2 Method

In this section, we summarize the continuum framework, introduce a constitutive model along with the boundary value problem, and its numerical discretization.

2.1 Biomechanical model

To describe the mechanical behavior of the liver, we use a total Lagrangian formalism. In general, we consider a body whose reference configuration is Ω_0 at time t_0, subjected to a force per unit mass $\boldsymbol{f}$, its boundary surface $\partial\Omega$ is divided into a Dirichlet part Γ_0^D constrained by a displacement $\overline{\boldsymbol{y}}$ and a Neumann part Γ_0^N subjected to a traction force $\overline{\boldsymbol{T}}$, the continuum equations stated in the strong form are

$$\begin{aligned} \rho_0 \ddot{\boldsymbol{y}} - \nabla \cdot \boldsymbol{\Sigma} &= \rho_0 \boldsymbol{f} \qquad \text{in } \Omega_0, \\ \boldsymbol{\Sigma} \cdot \boldsymbol{n} &= \overline{\boldsymbol{T}} \qquad \text{on } \Gamma_0^N, \\ \boldsymbol{y} &= \overline{\boldsymbol{y}} \qquad \text{on } \Gamma_0^D. \end{aligned} \tag{1}$$

In these relations ρ_0 is the density, $\boldsymbol{\Sigma}$ is the second Piola-Kirchhoff stress tensor, and $\boldsymbol{n}$ is the unit surface normal in the reference configuration.

Space integration In order to discretize problem (1) by a finite element method, consider a tetrahedral mesh $\{\mathcal{T}_h\}_{h>0}$ of the computational domain Ω_0. The discretized finite element formulation results in a nonlinear system of algebraic equations

$$M\ddot{Y} + F^{int}(Y) = F^{ext}, \quad \forall t \in [0, T], \tag{2}$$

where initial, internal and external forces are respectively given by

$$\begin{aligned} M\ddot{Y} &= \int_{\mathcal{T}_h} \rho_0 N_i N_j dV \ddot{Y}, \\ F_i^{int} &= \int_{\mathcal{T}_h} \boldsymbol{\Sigma} : \nabla N_i dV, \\ F_i^{ext} &= \int_{\mathcal{T}_h} \rho_0 \boldsymbol{f} \cdot N_i dV + \int_{\Gamma_{0h}^N} \overline{\boldsymbol{T}} \cdot N_i^S dS, \end{aligned} \tag{3}$$

where M is the mass matrix, N_i is the conventional shape function corresponding to node $i \in [1, N]$ with N the number of nodes. $Y \in \mathbb{R}^N$ is the vector of the current nodal positions.

Time integration : We chose a conventional implicit integration scheme provided by Newmark [1]. To this end, we consider a positive integer N and define $\Delta t = T/N$, $t_n = n\Delta t$, for $n = 0, 1, ..., N$. We compute the approximation Y^n by using the following second-order Newmark scheme

$$\begin{aligned} Y^{n+1} &= Y^n + \Delta t \dot{Y}^n + (1/4)\Delta t^2 \ddot{Y}^n, \\ \dot{Y}^{n+1} &= Y^n - (1/2)\Delta t \ddot{Y}^n, \\ M\ddot{Y}^{n+1} &+ F^{int}(Y^{n+1}) = F^{ext}_{n+1}. \end{aligned} \tag{4}$$

In hyperelastic models, the internal forces are provided by a non-linear function F^{int}. Here, we use the Newton-Raphson method to address the non-linearity at each time step.

The fully discretized problem (4) gives rise to a linear system of the form $Au = b$ which needs to be solved for each simulation time step and more than ones in case of non-linear models. Solving such a linear system could become extremely expensive from the computational point of view. Medical simulations are constrained by the need for real-time computation to enable interactivity of the simulation, this requirement translates into solving concurrently multiple linear systems under a very challenging time constraint.

Traditionally, to solve these linear systems, two types of approaches are used: direct and iterative solvers. Direct solvers provide the solution in a fixed number of steps. It mainly involves two phases: first, the factorization phase, e.g., $LU, LDL^\intercal$, then, the solving phase. The factorization phase is independent of the right hand side and is computationally more expensive than the solving phase. Iterative solvers, e.g., GMRES, on the other hand, do not modify the matrix and rely solely on matrix-vector products and other basic algebra operations. However, for an iterative solver to be efficient, choosing a good preconditioner [15] is imperative, but in some cases finding a good preconditioner is a difficult task.

To overcome the disadvantages of iterative solvers and to take advantage of the desirable features of direct solvers in the framework of parallel computing, there has been an increasing focus on the so-called hybrid methods such as domain decomposition and multigrid methods. For this paper, we adopt in the numerical implementation a parallel strategy based on domain decomposition method.

2.2 Domain decomposition solver

Domain decomposition methods are known to be a divide & conquer paradigm to accelerate numerical simulations. In our simulation context, we choose to use an overlapping Schwarz method. To describe it, we first divide the mesh $\{\mathcal{T}_h\}_{h>0}$ in N non-overlapping meshes (the sub-domains) $\{\mathcal{T}_i\}_{1 \leqslant i \leqslant N}$ using standard graph partitioners, e.g., METIS [11]. If δ is a positive integer, the overlapping decomposition $\left\{\mathcal{T}_i^\delta\right\}_{1 \leqslant i \leqslant N}$ is defined recursively as follows: $\mathcal{T}_i^\delta$ is obtained by including

all elements of $\mathcal{T}_i^{\delta-1}$ plus all adjacent elements of $\mathcal{T}_i^{\delta-1}$. For $\delta = 0$, $\mathcal{T}_i^{\delta} = \mathcal{T}_i$. Let $\left\{\mathcal{V}_i^{\delta}\right\}_{1\leqslant i\leqslant N}$ be the local deformation FE spaces defined on $\left\{\mathcal{T}_i^{\delta}\right\}_{1\leqslant i\leqslant N}$.

Now, consider the restrictions $\{R_i\}_{1\leqslant i\leqslant N}$ from $\mathcal{V}_h$ to $\left\{\mathcal{V}_i^{\delta}\right\}_{1\leqslant i\leqslant N}$ and a local partitions of unity $\{D_i\}_{1\leqslant i\leqslant N}$ such that:

$$\sum_{j=1}^{N} R_j^{\intercal} D_j R_j = Id_{n\times n},$$

where Id denotes the identity matrix and n is the global number of unknowns in the deformation space. Algebraically speaking, if n is the global number of deformation unknowns and $\{n_i\}_{1\leqslant i\leqslant N}$ are the numbers of degrees of freedom in each local deformation FE space, then R_i is a Boolean matrix of size $n_i \times n$, and D_i is a diagonal matrix of size $n_i \times n_i$, for all $1 \leqslant i \leqslant N$.

Using the partition of unity, one can use the one-level preconditioner, Restricted Additive Schwarz (RAS) method, proposed by Cai and Sarkis [2]:

$$\mathcal{M}_{\text{RAS}}^{-1} = \sum_{i=1}^{N} R_i^{\intercal} D_i A_i^{-1} R_i, \tag{5}$$

where the $\{A_i\}_{1\leqslant i\leqslant N}$ are local operators defined by the submatrices $\{R_i A R_i^{\intercal}\}_{1\leqslant i\leqslant N}$. In this case, we thus chose to use a more sophisticated multilevel domain decomposition method using the GenEO approach [17, 6]. This preconditioner, $\mathcal{M}_{\text{GenEO}}^{-1}$, uses a spectral coarse grid to better couple all sub-domains.

3 Results

This section aims to assess the efficiency of linear solvers described in the previous section in the presence of non-linear deformation model. To this end, we consider Saint-Venant Kirchhoff as a constitutive law to model the liver mechanical response. The Saint-Venant Kirchhoff law is given by the following potential:

$$W(e) = \frac{\lambda}{2}(Tr(e))^2 + \mu(Tr(e^2)), \tag{6}$$

where e is the Green Lagrange tensor $e = \frac{1}{2}\Big(\nabla \boldsymbol{y} + (\nabla \boldsymbol{y})^{\intercal} + (\nabla \boldsymbol{y})^{\intercal} \cdot \nabla \boldsymbol{y}\Big)$. Then the second Piola stress tensor is given by $\boldsymbol{\Sigma} = \frac{\partial W}{\partial e}$. λ and μ are the Lamé coefficients that can be determined from the Youngs modulus E and Poissons ratio ν.

The geometry of the model is segmented from a patient pre-operative Computed Tomography (CT) image. The domain is then meshed in a set of linear tetrahedral elements using GMSH [5]. In all the following simulations, we use two different mesh discretizations. An initial tetrahedral mesh with 3316 elements which yields a linear system A with 2000 unknowns. Then, we refine the same mesh by splitting each element into multiple smaller elements to get a

finer mesh with 22208 elements, which yields a linear system A with 12321 unknowns. For domain decomposition purpose, the mesh is decomposed using the graph partitioner METIS [11] (figure 1). The resulting finite element linear system is preconditioned with $\mathcal{M}^{-1}_{\text{GenEO}}$, and the GMRES solver is stopped when the relative preconditioned residual is lower than 10^{-6}

To implement the physical model, we have employed the open source simulation software FreeFem [7]. The linear solvers and the preconditioners are implemented in HPDDM [10]. We used the PARDISO [16] library for direct solver. Results were obtained on a standard desktop machine equipped with Intel with 6 Intel cores clocked at 3.2 GHz.

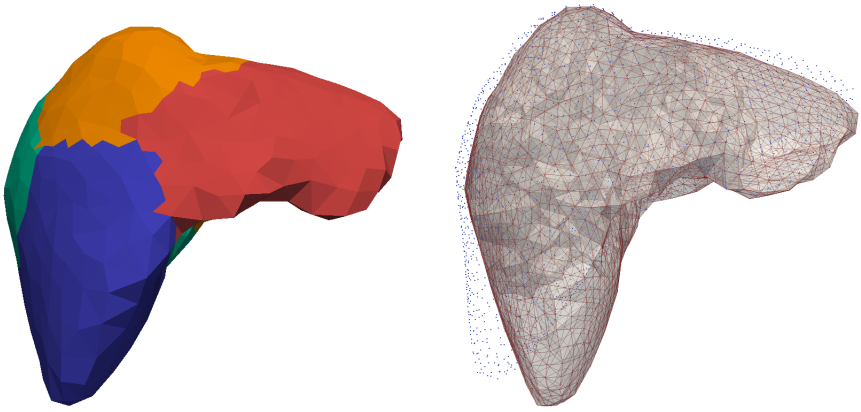

(a) Liver domain decomposition in 4 sub domains.

(b) Liver deformation estimated by a non linear model.

Fig 1: Left: liver computational domain decomposed in 4 sub-domains using the graph partitioner METIS [11] - Right: Liver deformation estimated by the non-linear Saint-Venant Kirchhoff law (the initial configuration is represented by blue points).

3.1 Static non-linear deformation

In this paragraph we evaluate the performances of pure direct solver versus domain decomposition solver for static deformation using a Newton-Raphson algorithm. We simulated an entire liver deformation. A volumic force of $100Pa$ in the $(x + y)$ direction is uniformly applied to the liver while several selected vertices of a plane are fixed (representing the ligament and veins). We considered Young modulus $E = 3 \cdot 10^3$ and Poisson ratio $\nu = 0.35$. We do not consider the liver as a fully incompressible material in this test. The simulated deformation is shown in Fig. 1b, where the deformed mesh is ploted as well as the intial liver configuration (represented by blue points).

N	# d.o.f per sub.	Prec(ms).	Solves(ms).	Total(ms).	# Newton iterations	# Iterations per Newton it	Speedup	# of d.o.f.
1	1998	0.00	47.96	47.96	3	1	-	
2	1263	16.50	11.05	27.55	3	8	1.7	$2.00 \cdot 10^3$
4	897	12.88	7.89	20.77	3	9	2.3	
1	12321	0.00	421.97	421.97	4	1	-	
2	7056	142.68	105.86	248.54	4	10	1.7	$12.32 \cdot 10^3$
4	4494	99.00	94.92	193.91	4	13	2.1	

Table 1: Breakdown of the time spent in solver steps for 3D non-linear solver with respect to the number of subdomains, the second column corresponds to the maximum number of unknowns per subdomain, the third column is the time spent in building the DDM preconditioner, and the fourth column corresponds to the time spent in solving the multiple Newton inner linear systems.

In Table 1, we report the time spent in all subroutines included during the multiples Newton iterations solve with respect to the number of subdomains N. The case $N = 1$ corresponds direct solver case, where the system is first factorized with and $LDL^\intercal$ than solved. For $N \geq 2$, the system is solved using GMRES with a domain decomposition preconditioner $\mathcal{M}^{-1}_{\text{GenEO}}$. Very few Newton iterations (column number 6) are needed for the solver to converge, independently of the number of subdomains (first column). The scalability of the solving approach is reported in the table using the run of the direct solver (a.k.a $N = 1$) as a reference. For each mesh, we ensure that we are calculating the same solution regardless of the linear solver type (direct or domain decomposition solver). To do that, we make sure that L_2 norm of the final deformation is the same during each scalbility test.

We notice that domain decomposition approach is already providing a reasonable speedup with respect to the number of subdomains. Moreover, we observe that using a simple direct solver approach requires to build the factorization again for each inner Newton iteration with the same high cost. Whereas with domain decomposition approach the same preconditioner is reused for all the Newton iterations with no significant impact on the GMRES solver, thanks to the robustness of the DD preconditioner, the number of Krylov iterations remains stable. This suggests that we can take more benefits in a scenario of dynamic deformations, where we need to solve more linear systems successively through both Newton iterations and time integration algorithm.

The scalability is impacted by the number of unknowns per subdomain, which is not scaling linearly with the number subdomains. This fact is first due to the load balancing provided by the graph partitioner and also due to the overlapping regions between subdomains, which seems to be more critical in case of small meshes. We also notice that the increase in the number of unknowns from 2000 to 12321 leads to the increase of the computation time. This happens because the convergence of the iterative solvers is influenced by the condition number

of the stiffness matrix, and the condition number will increase with a decreased element size for a given object.

3.2 Dynamic non-linear deformation

The main objective of this paragraph is to show that the cost of the domain decomposition preconditioner is quickly amortized in the scenario of successive solutions of linear systems. Typically in case of stiff elastic deformation where the implicit integration method is more appropriate. To this end, we solve the entire discretized problem (4), where, a Newmark, implicit time integration scheme is used with a time step of 0.01s, in this scenario, the same volume force as the one used in the static case is again uniformly applied to the liver (Fig. 1b) for 0.03s than released to let the system reaches the equilibrium state. We simulate the liver deformation for both discretizations with coarse mesh yielding a system of 2000 unknowns and refined mesh yielding a system of 12321 unknowns. In Fig 2, we show the behavior of computational time spent in solving the successive linear system. The red and blue curves represent, respectively, the coarse and fine mesh discretization. The global domain has been decomposed in 4 subdomains allowing the simulation to run on 4 processors. For each time step, the Newton-Raphson

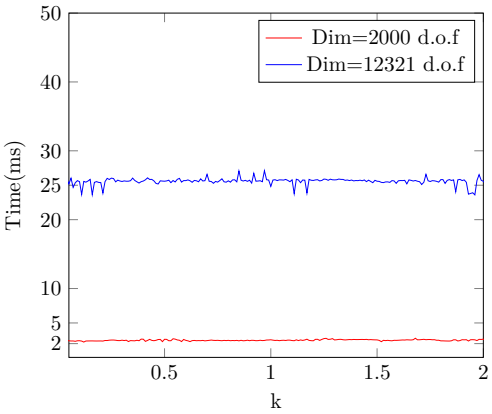

Fig 2: Performances of domain decomposition solver during the simulation of a dynamic non-linear deformation liver response. Using the Saint-Venant Kirchhoff model. Red and blue curves represent the computation time per Newton iteration over time steps with resp to coarse mesh (2000 unknowns) and refined mesh (12321 unknowns).

algorithm is performed to update the deformation state. We use the domain decomposition approach as a solver, where preconditioner $\mathcal{M}^{-1}_{\text{GenEO}}$ is built at the first time step than used for preconditioning all the following Newton inner linear systems

3.3 Contact & deformation

While keeping the context of simulating the behavior of soft tissues, we can point out the importance of providing methods and models to simulate the mechanical interactions on the organ model: interactions with the surrounding anatomical structures (i.e. contacts), interactions with different surgical instruments leading to contacts or other types of complex interactions. Simulating these interactions necessitate to detect them, to model them, and then to solve them with adapted numerical methods. In practice the numerical system to solve is an augmented version of linear systems that we have solved in previous paragraphs. If we consider the case of a two-body interaction, the augmented system takes the following form

$$AU = b + J^T \lambda \tag{7}$$

which can be formulated as

$$\begin{bmatrix} A_1 & 0 & J_1^T \\ 0 & A_2 & J_1^T \\ J_1 & J_2 & 0 \end{bmatrix} \begin{bmatrix} \boldsymbol{y}_1 \\ \boldsymbol{y}_2 \\ \lambda \end{bmatrix} = \begin{bmatrix} b_1 \\ b_2 \\ -\delta \end{bmatrix} \tag{8}$$

A_1 and A_2 correspond to the linear operators of each body J_1, J_1 model the interaction, then the unknowns are the $\boldsymbol{y}_1$, $\boldsymbol{y}_2$ are respectively the displacement of the two bodies and λ is the vector of contact forces. We believe that in such case if interaction, domain decomposition approach has a tremendous potential for solving problem (7). And more than accelerating the linear solves, domain decomposition can be specifically designed to consider the interaction area as a single sub-domain domain. This possibility would allow a partial updating of the global operator, and is likely to lead to a substantial gain in simulation time.

4 Conclusion

In this work, we have investigated the computational expense of solving linear systems resulting from a combination of non-linear model and dynamic integration. We showed that employing hybrid solver like a domain decomposition method has a real potential to harness the capability of small parallel machines since it takes full advantage in making the solving procedure fully parallel. On the other hand, the robustness of domain decomposition preconditioners makes it possible to reuse the preconditioner for successive solves. These two strategies combined open up the possibility to significantly accelerate the computation for complex simulation and meet the real-time feedback, which is a hard constraint in surgical training or intra-operative guidance.

The next step will be to integrate the domain decomposition paradigm with fast hyperelastic FEM models and implicit contact schemes. We will also investigate further the limited scalability of the current approach when dealing with real-time applications, which is likely due to load balancing. This can be improved by a better tuning of the graph partitioner .

Bibliography

[1] Bathe, K.J.: Finite element procedures. Klaus-Jurgen Bathe (2006)

[2] Cai, X.C., Sarkis, M.: A restricted additive Schwarz preconditioner for general sparse linear systems. SIAM Journal on Scientific Computing **21**, 239–247 (1999)

[3] Cotin, S., Delingette, H., Ayache, N.: Real-time elastic deformations of soft tissues for surgery simulation. IEEE transactions on Visualization and Computer Graphics **5**(1), 62–73 (1999)

[4] Dolean, V., Jolivet, P., Nataf, F.: An introduction to domain decomposition methods. Society for Industrial and Applied Mathematics (SIAM), Philadelphia, PA (2015), algorithms, theory, and parallel implementation

[5] Geuzaine, C., Remacle, J.F.: Gmsh: A 3-d finite element mesh generator with built-in pre-and post-processing facilities. International journal for numerical methods in engineering **79**(11), 1309–1331 (2009)

[6] Haferssas, R., Jolivet, P., Nataf, F.: An additive schwarz method type theory for lions's algorithm and a symmetrized optimized restricted additive schwarz method. SIAM Journal on Scientific Computing **39**(4), A1345–A1365 (2017)

[7] Hecht, F.: New development in FreeFem++. J. Numer. Math. **20**(3-4), 251–265 (2012)

[8] Henson, V.E., Yang, U.M.: *BoomerAMG*: A parallel algebraic multigrid solver and preconditioner. Applied Numerical Mathematics **41**(1), 155–177 (2002)

[9] Joldes, G.R., Wittek, A., Miller, K.: Suite of finite element algorithms for accurate computation of soft tissue deformation for surgical simulation. Medical Image Analysis **13**(6), 912–919 (2009)

[10] Jolivet, P., Hecht, F., Nataf, F., Prud'homme, C.: Scalable domain decomposition preconditioners for heterogeneous elliptic problems. In: Proceedings of the 2013 ACM/IEEE conference on Supercomputing. pp. 80:1–80:11. SC13, ACM (2013)

[11] Karypis, G., Kumar, V.: METIS: A software package for partitioning unstructured graphs, partitioning meshes, and computing fill-reducing orderings of sparse matrices. Tech. rep., Department of Computer Science, University of Minnesota (1998)

[12] Klawonn, A., Lanser, M., Rheinbach, O.: Nonlinear feti-dp and bddc methods. SIAM Journal on Scientific Computing **36**(2), A737–A765 (2014)

[13] Miller, K., Joldes, G., Lance, D., Wittek, A.: Total lagrangian explicit dynamics finite element algorithm for computing soft tissue deformation. Communications in numerical methods in engineering **23**(2), 121–134 (2007)

[14] Picinbono, G., Delingette, H., Ayache, N.: Real-time large displacement elasticity for surgery simulation: Non-linear tensor-mass model. In: International Conference on Medical Image Computing and Computer-Assisted Intervention. pp. 643–652. Springer (2000)

[15] Saad, Y.: Iterative Methods for Sparse Linear Systems. PWS Publishing Company (1996)
[16] Schenk, O., Gärtner, K., Fichtner, W.: Efficient sparse LU factorization with left-right looking strategy on shared memory multiprocessors. BIT Numerical Mathematics **40**(1), 158–176 (2000)
[17] Spillane, N., Dolean, V., Hauret, P., Nataf, F., Pechstein, C., Scheichl, R.: Abstract robust coarse spaces for systems of PDEs via generalized eigenproblems in the overlaps. Numer. Math. **126**(4), 741–770 (2014)
[18] Sundar, H., Biros, G., Burstedde, C., Rudi, J., Ghattas, O., Stadler, G.: Parallel geometric-algebraic multigrid on unstructured forests of octrees. In: Proceedings of the 2012 ACM/IEEE conference on Supercomputing. SC12, IEEE Computer Society (2012)
[19] Toselli, A., Widlund, O.: Domain Decomposition Methods - Algorithms and Theory, Springer Series in Computational Mathematics, vol. 34. Springer (2005)

Design of Auxetic Coronary Stents by Topology Optimization

Huipeng Xue, Zhen Luo*

School of Mechanical and Mechatronic Engineering, University of Technology Sydney, 15 Broadway, Ultimo, NSW 2007, Australia

* Corresponding author: zhen.luo@uts.edu.au

Abstract: Coronary artery stents are the most important implantation devices for the practice of the interventional cardiology to treat coronary artery disease (CAD) since the mid-1980s. However, the problems of stent thrombosis (ST) and in-stent restenosis (ISR) still exist. In addition to the reasons of implanted materials and coatings, mechanical and structural factors are also important factors and responsible for the complications, such as inadequate stent expansion, incomplete stent apposition and stent fracture in design. This research aims to develop a concurrent topology optimization by a parametric level set method associated with numerical homogenization method to generate novel architectures for self-expanding (SE) stents with mechanical auxetic metamaterials. The topological design is firstly implemented in MATLAB, and then the optimized architecture is further improved and optimized in the commercial software ANSYS. The final stenting structure is numerically validated to demonstrate the effectiveness of the design method.

Keywords: Self-expanding stents, Auxetics, level sets, Topology optimization

1 Introduction

Coronary artery disease (CAD) also known as ischemic heart disease (IHD) has a high mortality even nowadays. Percutaneous coronary intervention (PCI) technology has been widely accepted as an effective treatment after 40 years development [1, 2]. Among that, the implantation of coronary stents can significantly de-

crease the rates of restenosis and abrupt closure of arteries to increase life expectancy of patients [3, 4].

In the early days, bare-metal stents (BMS) were used in conjunction with angioplasty due to successful results in treating abrupt and susceptible vessel closure [5, 6]. However, the incidence of stent thrombosis (ST), in-stent restenosis (ISR) and other complications [7] resulted in the generation of drug-eluting stents (DES) [8]. DES are superior to BMS in that it can reduce the rate of ISR but have a higher risk of ST in the late thrombosis [9, 10], due to drug coatings. Even for the new generation of biodegradable stents (BDS) and bioresorbable vascular scaffolds (BVS), these drawbacks still remain [11, 12]. Compared with the risk of ST in the late healing stage, DES show an obvious decrease of ISR in the short-term treatment without brachytherapy or intracoronary radiation. This is the reason why DES are more popular recently. Nevertheless, it has been reported that DES result in a higher risk of late thrombosis compared with BMS. The much higher cost of DES doesn't lead to a significant increase in life expectancy than other stents [13].

According to different expansion mechanisms, stents can also be divided into self-expanding (SE) and balloon-expandable (BE) stents. In 1986, stents with self expanding properties were firstly introduced into balloon angioplasty for treating abrupt closure of arteries [3]. The characteristics of positive supporting and shape memory metal materials [15] gave good short-term treatment results. The most advantages of SE stents can be summarized as: (1) The gradual expansion manner of SE stents leads to a lower incidence of edge dissections. It can avoid immediate vessel wall injury compared with BE stents, which makes SE stents more suitable for treating small-diameter vessels [16], (2) The good conformability makes it easily to match different lesion shapes, which is superior to any other stent for treating vulnerable plaques and bifurcation lesions, as well as preventing inadequate stent expansion, and (3) The used superelastic materials exhibit much better mechanical properties than materials of BE stents with respect to fracture toughness, flexibility, fatigue strength and corrosion resistance.

However, some unfavorable features [17, 18] of SE stents limit their clinical use. First, the SE stents are usually hosed into cumbersome catheters during the implantation, which makes the delivery difficult. Second, the complicated placement demands high accuracy due to the phenomenon of foreshortening after deployment. Third, the continual outward supporting of conventional SE stents is not adaptive and difficult to accurately control, which may lead to a larger luminal diameter than the original size that will further pose a thrombotic threat.

Besides biological factors, structural or mechanical aspects also play an important role in stents, and they can trigger serious complications finally leading to ST and ISR, such as inadequate stent expansion, incomplete stent apposition and stent fracture in design [14]. These issues can be addressed via new stenting structures, new artificial materials or new expansion methods. Hence, the alternative designs that can avoid or help reduce these complications are still in demands.

In this paper, we will focus on the development of a novel family of SE stents using topological design optimization technology together with a new type of me-

chanical metamaterials—auxetics, with a view to generating new stenting structural architectures, to help reduce the occurrence of ST and ISR after implantation.

Compared to most conventional materials with positive Poisson's ratios, auxetics are a special kind of mechanical metamaterials artificially designed to exhibit negative Poisson's ratios (NPR) [19, 20]. Auxetic materials will contract in transverse directions when they are compressed uniaxially. Auxetics provides enhanced mechanical properties such as indentation resistance, fracture toughness, and shear stiffness, which greatly facilitate a range of applications, including energy absorption, anti-impact, thermal isolation and biomedical applications [21, 22].

Topology optimization provides an efficient way to find the best material distributions under the boundary and loads conditions in the design domain. It has been wildly used in the structural and material designs over the past two decades, and several popular methods have been developed, such as the solid isotropic material with penalization (SIMP) method [23, 24], the evolutionary structural optimization (ESO) method [25], and level set method (LSM) [26-28].

The numerical homogenization method [29, 30] has been developed to evaluate the effective properties of microstructures. It is usually combined with other topology optimization methods for the design of microstructures and the related cellular composites. This kind of cellular composites mostly consists of periodic microstructures and the microstructures can be given special properties such as auxetics. The topological design of multifunctional cellular composites enables many applications in engineering [31].

LSM is one of the recently developed method for topological shape optimization of structures. It has shown excellent ability to capture geometry and shape of the design. The key concept is to embed the design boundary of a structure as the zero-level set of a higher-dimensional level set function. Since the evolution of the level set function can be described by the Hamilton-Jacobi Partial Differential Equation (PDE) [32], the dynamic motion of the level set function can be tracked by solving this equation. However, some strict conditions are required during the numerical implementation of the H-J PDE, such as the Courant-Friedrichs-Lewy (CFL) condition, boundary velocity extensions, and re-initializations [32]. As one of the alternative LSMs, the parametric level set method (PLSM) [33-35] has shown it is high efficiency in solving topology optimization [36] and this paper will apply the PLSM to design the stenting structural architectures.

To realize the design of ASE stents, a concurrent topological design method will be applied to find auxetic stenting architecture as microstructures, and at the same time the compliance of the macro stenting structure is considered to maintain the stiffness requirement of stents. Topology optimization will be applied to explore the best material layout for the SE stents, and the auxetics will be included into the biocompatible materials to enable an adaptive "self-expanding" procedure of stenting structures. The structure periodically consists of identical auxetic unit cells. This will deliver a new kind of auxetic SE (ASE) stents to address the above problems relevant to ST and ISR due to the mechanical and structural issues of the current stenting designs. The topological optimization can help find the most efficient stenting structures, and auxetics will make SE stents much smaller when

compressed, beneficial to deliverability. The optimized ASE stents can also eliminate the foreshortening to help the deployment. Moreover, the auxetic behavior can also enhance the flexibility, conformability, and fatigue strength of SE stents.

2 Parametric level-set method

The unique characteristic of the level set method is the implicit description of the structural boundary, which is presented at the zero level set of a higher-dimensional level set function $\Phi(x)$, as shown in Eq. (2.1) As a 2D example illustrated in Fig.2.1, $\Phi(x)=0$ shows the boundary of a structure located at zero level set.

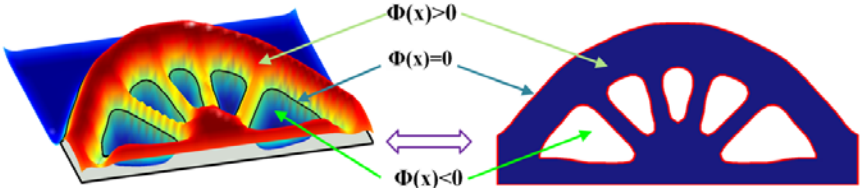

Fig. 2.1 Level set function (left) and design domain located at zero level set (right).

$$\begin{cases} \Phi(x) > 0 & x \in \Omega \setminus \partial\Omega & (Material) \\ \Phi(x) = 0 & x \in \partial\Omega & (Boundary) \\ \Phi(x) < 0 & x \in D \setminus (\Omega \bigcup \partial\Omega) & (Void) \end{cases} \tag{2.1}$$

where x is the point in the space D, Ω and $\partial\Omega$ denote the design domain and the boundary, respectively. The dynamic motion of the design domain Ω can be achieved by solving Hamilton-Jacobi PDE, as shown in (2.2). In that process, the normal velocity filed V_n of the boundary $\partial\Omega$ is used to enable the dynamic motion of the level set function.

$$\frac{\partial \Phi(x,t)}{\partial t} - V_n \left| \nabla \Phi(x,t) \right| = 0 \tag{2.2}$$

The interpolation of the level set function $\Phi(x)$ by using CSRBFs $\varphi(x)$ based on the fixed knots in the design domain can be described as Eq. (2.3).

$$\Phi(x,t) = \varphi(x)^T \alpha(t) = \sum_{i=1}^{N} \varphi_i(x) \alpha_i(t) \tag{2.3}$$

where N is the total number of fixed knots in the design domain, $\alpha_i(t)$ is the expansion coefficient of the interpolation with respect of the ith knot, and the CSRBFs of the ith knot used with C2 continuity is given by:

$$\begin{aligned} \varphi_i(x) &= max\left\{0,\left(1-r_i(x)\right)^4\right\}\left(4r_i(x)+1\right) \\ r_i(x) &= d_I / d_{mI} = \sqrt{(x-x_i)^2+(y-y_i)^2}\Big/ d_{mI} \end{aligned} \tag{2.4}$$

where d_I denotes the distance between the current sample knot (x, y) and the ith knot (x_i, y_i), and d_{mI} denotes the radius of the support domain of the ith knot.

Then, the conventional Hamilton–Jacobi PDE is transformed as Eq. (2.5), and the new velocity field V_n can be described as (2.6). Therefore, the dynamic motion of level set function $\Phi(x)$ is only related to the design variables expansion coefficient vector $\alpha(t)$. Because $\alpha(t)$ is being evaluated by all knots in the design domain, no addition extension scheme is required. In this way, the standard LSM is converted into a parametric form.

$$\varphi(X)^T \dot{\alpha}(t) - V_n \left|(\nabla\varphi)^T \alpha(t)\right| = 0 \tag{2.5}$$

$$V_n = \frac{\varphi(X)^T}{\left|(\nabla\varphi)^T \alpha(t)\right|}\dot{\alpha}(t), \quad \text{where } \dot{\alpha}(t) = \frac{d\alpha(t)}{dt} \tag{2.6}$$

3 Numerical homogenization method

The numerical homogenization method has been widely used to approximate the effective properties of microstructures. The effective elasticity tensor D^H_{ijkl} of a 2D microstructure can be calculated by:

$$D^H_{ijkl} = \frac{1}{\left|\Omega^{MI}\right|}\int_{\Omega^{MI}} \left(\varepsilon^{0(ij)}_{pq} - \varepsilon^{*(ij)}_{pq}\left(u^{MI(ij)}\right)\right) D_{pqrs} \left(\varepsilon^{0(kl)}_{rs} - \varepsilon^{*(kl)}_{rs}\left(u^{MI(ij)}\right)\right) H(\Phi^{MI}) d\Omega^{MI} \tag{3.1}$$

where the superscript '*MI*' indicates the quantities in the microscale; Ω^{MI} is the design domain of the microstructure; $|\Omega^{MI}|$ is the area of the microstructure; and Φ^{MI} is the level set function in the microscale. i, j, k, l=1, 2. D_{pqrs} is the elasticity tensor of the base material. $H(\Phi^{MI})$ is the Heaviside function[27]. $\varepsilon^{0(ij)}_{pq}$ is the test unit strain field, where $(1,0,0)^T$, $(0,1,0)^T$ and $(0,0,1)^T$ are used in 2D models; $\varepsilon^{*(ij)}_{pq}$ is the locally varying strain fields and defined by:

$$\varepsilon_{pq}^{*(ij)}\left(u^{MI(ij)}\right)=\frac{1}{2}(u_{p,q}^{MI(ij)}+u_{q,p}^{MI(ij)}) \tag{3.2}$$

By using the virtual displacement field $v^{MI(kl)}$ in $\bar{U}(\Omega^{MI})$ that is the space consisting of all the kinematically admissible displacements in Ω^{MI}, the displacement field $u^{MI(ij)}$ can be calculated through finite element analysis using the periodical boundary conditions of the microstructure:

$$\int_{\Omega^{MI}}(\varepsilon_{pq}^{0(ij)}-\varepsilon_{pq}^{*(ij)}(u^{MI(ij)}))D_{pqrs}\varepsilon_{rs}^{*(kl)}(v^{MI(kl)})H(\Phi^{MI})d\Omega^{MI}=0,\ \forall\, v^{MI(kl)}\in\bar{U}(\Omega^{MI}) \tag{3.3}$$

4 The 1stoptimization stage forthe design ofauxetics

4.1 Theconcurrent optimization scheme

The concurrent topology optimization scheme is defined as a multi-objective optimization problem to find an expansion coefficient vector α_n^{MI} for microstructure to obtain negative Poisson's ratios, and minimum the compliance of the macrostructure. A piece of the stent approximated as rectangle shape is used as the micro design domain consisted of one unique microstructure, shown in Fig.4.1; two coordinates are used to describe the design domains: the macrostructure(X_1, X_2) and microstructure(Y_1, Y_2); the vertical degree of freedom is fixed at the top and bottom edges of the macro structure, while two unit forces F are applied on the left and right edges in the horizontal direction. 2D four-node rectangle elements is adopted and each element has a unit length, height. The artificial base material model with Young's modulus 1 and Poisson's ratio 0.3 used. The numerical design scheme can be described as Eq. (4.1).

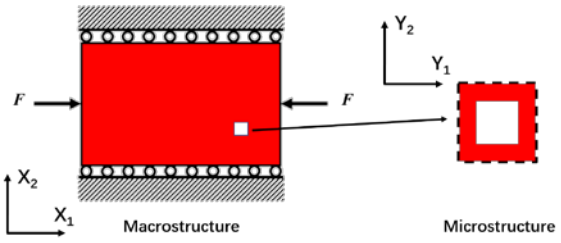

Fig.4.1 The macrostructure(left) and microstructure(right).

$$
\begin{aligned}
&\text{Find} \quad \alpha_n^{MI}\,(n = 1, 2, \ldots, N)\\
&\text{Min} \quad J = J^{MA} + J^{MI}\\
&\text{S.T.} \quad G = \int_{\Omega^{MI}} H(\Phi^{MI})\,d\Omega^{MI} \le V^{max}\\
&\qquad a^{MA}(u^{MA}, v^{MA}) = l^{MA}(v^{MA}),\ \forall\, v^{MA} \in \overline{U}(\Omega^{MA})\\
&\qquad a^{MI}(u^{MI}, v^{MI}, \Phi^{MI}) = l^{MA}(v^{MA}, \Phi^{MI}),\ \forall\, v^{MI} \in \overline{U}(\Omega^{MI})\\
&\qquad \alpha_{min}^{MI} \le \alpha_n^{MI} \le \alpha_{max}^{MI}
\end{aligned}
\tag{4.1}
$$

where,

$$
\begin{aligned}
J^{MA} &= \frac{1}{2}\int_{\Omega^{MA}} \varepsilon_{ij}(u^{MA}) D_{ijkl}^{H} \varepsilon_{kl}(u^{MA})\,d\Omega^{MA}\\
J^{MI} &= (D_{12}^{H} / D_{11}^{H} + 1)^2 + (D_{12}^{H} / D_{22}^{H} + 1)^2
\end{aligned}
$$

where, the superscript '*MA*' and '*MI*' denotes the macro and micro quantities, respectively. The expansion coefficients of the CSRBF interpolation α_n^{MI} is the design variable in the microscale, which are within α_{min}^{MI} and α_{max}^{MI}. N is the total number of fixed knots in the micro design domain. J is the total objective function, which is comprised of the macro objective function J^{MA} the compliance of the macrostructure, and micro objective function J^{MI} the Poisson's ratios of the microstructure. D_{11}^{H}, D_{12}^{H}, D_{22}^{H} are specific values of the effective elasticity tensor of the microstructure. Here, the optimized microstructure is defined as isotropic or orthotropic material, thus there are two Poisson's ratios defined the in micro objective function. G is the volume constraint and the upper limitation is defined as V^{max}. u and v are the real and virtual displacement fields.

The bilinear energy and the linear load forms of the finite element model in the macroscale can be described as:

$$
a^{MA}(u^{MA}, v^{MA}) = \int_{\Omega^{MA}} \varepsilon_{ij}(u^{MA}) D_{ijkl}^{H} \varepsilon_{kl}(v^{MA})\,d\Omega^{MA} \tag{4.2}
$$

$$
l^{MA}(v^{MA}) = \int_{\Omega^{MA}} p v^{MA}\,d\Omega^{MA} + \int_{\Omega^{MA}} \tau v^{MA}\,d\Gamma^{MA} \tag{4.3}
$$

where p is the body force and τ is the traction of the boundary Γ^{MA}. The bilinear energy and the linear load forms of finite element model in the microscale can be described as:

$$
a^{MI}(u^{MI}, v^{MI}, \Phi^{MI}) = \int_{\Omega^{MI}} \varepsilon_{ij}^{*(ij)}(u^{MI(ij)}) D_{pqrs} \varepsilon_{kl}^{*(kl)}(v^{MI(kl)}) H(\Phi^{MI})\,d\Omega^{MI} \tag{4.4}
$$

$$
l^{MI}(v^{MI}, \Phi^{MI}) = \int_{\Omega^{MI}} \varepsilon_{ij}^{0(ij)} D_{pqrs} \varepsilon_{kl}^{*(kl)}(v^{MI(kl)}) H(\Phi^{MI})\,d\Omega^{MI} \tag{4.5}
$$

4.2 The sensitivity analysis

Based on the concurrent topology optimization model presented in section 4.1, the sensitivity analysis of the design variables is required. It is divided into two parts due to the two different scales and calculated based on the first-order derivatives of the objective function with respect to the expansion coefficients α_n^{MI}. The sensitivity in the macro-scale is:

$$\frac{\partial J^{MA}}{\partial \alpha_n^{MI}} = \frac{1}{2}\int_{\Omega^{MA}} \varepsilon_{ij}(u^{MA}) \frac{\partial D_{ijkl}^H}{\partial \alpha_n^{MI}} \varepsilon_{kl}(u^{MA}) d\Omega^{MA} \tag{4.6}$$

Since the elastic system is self-adjoint[37], the shape derivative of the elasticity tensor D_{ijkl}^H can be calculated by:

$$\frac{\partial D_{ijkl}^H}{\partial t} = -\frac{1}{\left|\Omega^{MI}\right|}\int_{\Omega^{MI}} \beta(u^{MI})\varphi^{MI}(x)^T V_n \left|(\nabla \Phi^{MI})^T\right| \delta(\Phi^{MI}) d\Omega^{MI} \tag{4.7}$$

where $\delta(\Phi^{MI})$ is the derivative of the Heaviside function $H(\Phi^{MI})$, and $\beta(u^{MI})$ is:

$$\beta(u^{MI}) = (\varepsilon_{pq}^{0(ij)} - \varepsilon_{pq}^{*(ij)}(u^{MI(ij)}))D_{pqrs}(\varepsilon_{rs}^{0(kl)} - \varepsilon_{rs}^{*(kl)}(u^{MI(kl)})) \tag{4.8}$$

Substituting the normal velocity V_n^{MI} defined in Eq. (2.6) into Eq. (4.8):

$$\frac{\partial D_{ijkl}^H}{\partial t} = -\sum_{n=1}^{N}\left(\frac{1}{\left|\Omega^{MI}\right|}\int_{\Omega^{MI}} \beta(u^{MI})\varphi^{MI}(x)^T \delta(\Phi^{MI}) d\Omega^{MI}\right)\dot{\alpha}_n^{MI}(t) \tag{4.9}$$

While, the first-order derivative of the effective elasticity tensor D_{ijkl}^H with respect to t can be directly obtained by the chain rule:

$$\frac{\partial D_{ijkl}^H}{\partial t} = \sum_{n=1}^{N} \frac{\partial D_{ijkl}^H}{\partial \alpha_n^{MI}} \dot{\alpha}_n^{MI}(t) \tag{4.10}$$

Comparing (4.9) and (4.10), the derivative of the effective elasticity tensor D_{ijkl}^H with respect to the design variables α_n^{MI} can be calculated as:

$$\frac{\partial D_{ijkl}^H}{\partial \alpha_n^{MI}} = -\frac{1}{\left|\Omega^{MI}\right|}\int_{\Omega^{MI}} \beta(u^{MI})\varphi^{MI}(x)^T \delta(\Phi^{MI}) d\Omega^{MI} \tag{4.11}$$

Then the derivative of the macro objective function J^{MA} with respect to the design variables α_n^{MI} can be obtained by Substituting Eq. (4.11) into (4.6). Similarly, the derivative of the micro objective function J^{MI} with respect to the design variables can be calculated as shown in (4.12), and the derivative of the volume constrains G with respect to the design variables are given by (4.13)

$$\frac{\partial J^{MI}}{\partial \alpha_n^{MI}} = \frac{\partial (D_{12}^H / D_{11}^H + 1)^2}{\partial \alpha_n^{MI}} + \frac{\partial (D_{12}^H / D_{22}^H + 1)^2}{\partial \alpha_n^{MI}} \tag{4.12}$$

$$\frac{\partial G}{\partial \alpha_n^{MI}} = \int_{\Omega^{MI}} \varphi^{MI}(x)^T \delta(\Phi^{MI}) d\Omega^{MI} \tag{4.13}$$

4.3 Numerical results

One of the main purposes of ISR is to implanting materials into the vessels, so the design of a stent usually uses as less material as possible to decrease the contacts between the stent and vessel walls. Meanwhile, the volume fraction of 35% is used for the microstructure design to ensure structural stiffness. To evaluate the numerical result, two values of Poisson's ratios ***Mu1*** and ***Mu2*** in two directions are defined as Eq. (4.15).

$$Mu1 = D_{12}^H / D_{11}^H, \quad Mu2 = D_{12}^H / D_{22}^H \tag{4.15}$$

Different discretized size of micro design domain will lead to different results, that is because more elements used in the design domain may capture more details of the optimized structure. Therefore, three different size of discretization 60×60, 100×100, 40×40 are used, and the relevant results are list in the table 4.1. All three results are of clear and smooth boundaries of the microstructures, and exhibit NPR properties in both two directions. The material of the stent should be uniformly distributed. In the result of 100×100, the bridges in the middle, top and bottom are too thin compared with other parts, so this is not a very good choice.

Mu1 and *Mu2* are used to illustrate the Poisson's ratios in two directions, where *Mu1* can be used to evaluate the deformation along the horizontal direction when deformed in the vertical direction, and *Mu2* is used to describe the opposite situation. Although both negative values of *Mu1* and *Mu2* are desired to obtain a smaller volume of stent when compressed, a smaller absolute value of *Mu1* can lead to a smaller deformation in the axis direction when stent supporting the vessel, which will prevent the shortening of the stent in axis direction. Hence, the result of 40×40 is better than 60×60. From that, we can see more elements may cap-

ture more details of the structure, but it may also lead to a complex or ununiform distribution of material which may not suitable for the stent design.

Table 4.1 Three numerical optimization results for auxetic microstructures.

Size	Microstructure	Level set surface	Effective elasticity tensor	Poisson's ratio
40×40		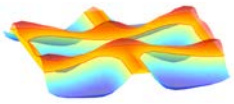	$\begin{bmatrix} 0.1473 & -0.0352 & 0 \\ -0.0352 & 0.0342 & 0 \\ 0 & 0 & 0.0043 \end{bmatrix}$	$Mu1 = -0.2390$ $Mu2 = -1.0292$
60×60		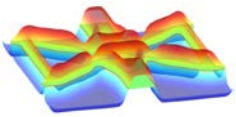	$\begin{bmatrix} 0.0578 & -0.0362 & 0 \\ -0.0362 & 0.0395 & 0 \\ 0 & 0 & 0.0023 \end{bmatrix}$	$Mu1 = -0.6263$ $Mu2 = -0.9165$
100×100	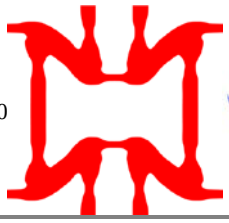	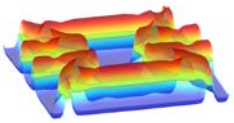	$\begin{bmatrix} 0.0509 & -0.0438 & 0 \\ -0.0438 & 0.0518 & 0 \\ 0 & 0 & 0.0021 \end{bmatrix}$	$Mu1 = -0.8605$ $Mu2 = -0.8456$

The optimized structure of 40×40 element scale is adopted in the first numerical optimization stage, as shown in Fig.4.2. From the figure, we can see the microscale is much smaller than the macroscale. However, as mentioned before, if much smaller microstructures are used, the one piece of the stent will be fully filled with the material as the left figure shown in Fig. 4.2. By doing this, the flexibility and conformability of the stent will decrease, and the incidence of ISR will significantly increase. Therefore, the optimized microstructure will be regarded as a smaller periodical macro unit cell in the macroscale.

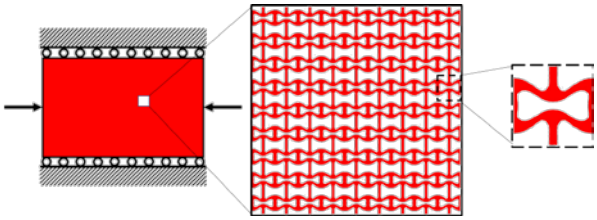

Fig.4.2 The macro structure (left), 9×9 microstructures (middle), and the unit cell of microstructure (right)

5 The 2nd optimization stage and the numerical validation

Since the mechanical behavior of a stent is more similar to a shell that the dimension of the thickness is much smaller than the dimensions of the length and width. 2D four-node rectangle element is used in the first step due to the computational efficiency, while the shell element needs to be adopted in the second stage of the optimization to amend the accuracy of the final design. Thus, the commercial software ANSYS v19.2 is utilized to preform topology optimization for a stent again with shell elements, based on the optimized result from the first stage. The geometry is built by 12 unit cells along the circumference and 16 unit cells along the axis, and 10 times bigger than the real stent as shown in Fig.5.1.

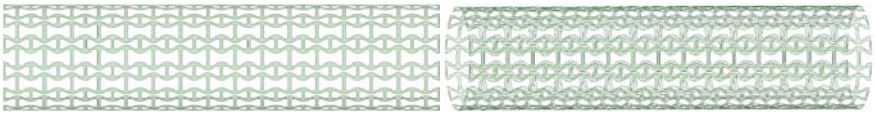

Fig.5.1 The stent structure built by the first design result

The volume fraction of the microstructure is specified as 35% in the first stage, and not too much material needs to be removed in the current stage. Hence, 10% volume fraction is used to maximum the global compliance of the stent in the second stage. The optimized result can be seen in Fig.5.2, and we can see small holes are generated in all the joints of the unit cells.

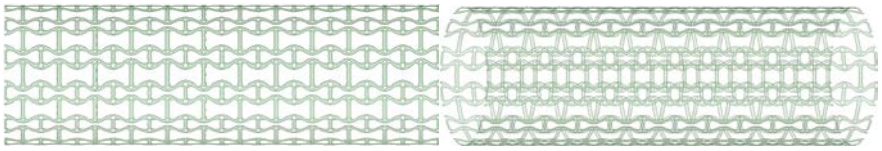

Fig.5.2 The result of the second topology optimization

The numerical validation is performed to test the auxetic property of the optimized stent in ANSYS. In the simulation, the degree of freedom in the X direction of the left edge and one point in the left end is fixed and a force applied on the right edge of the stent to compress or stretch it. The test under pression is shown in Fig. 5.3. The colourful structure shows deformed stent, while the grey colour shows undeformed stent. From the figure we can see the stent contract in the radial directions when they are compressed uniaxially. In the right-side view, the diameter become smaller compared with the original size of the stent.

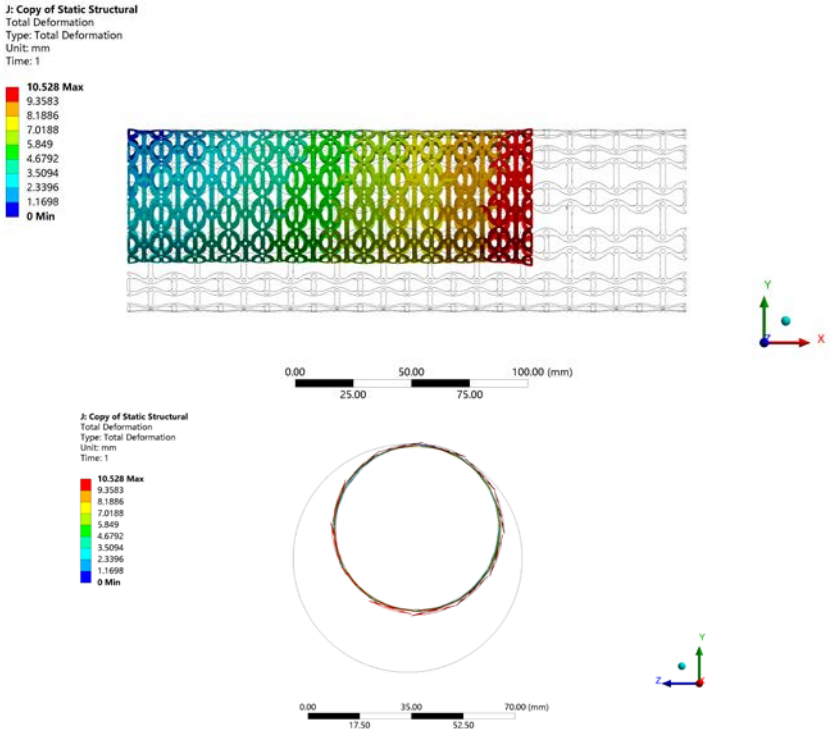

Fig.5.3 The pression test: the front view(left) and the right view(right)

Then, a stretching test is also performed, the result as shown in Fig. 5.4. The stent expanded in the radial directions when they are stretched uniaxially. Therefore, both compression and stretching test performed for the optimized stent illustrate a significant auxetic property.

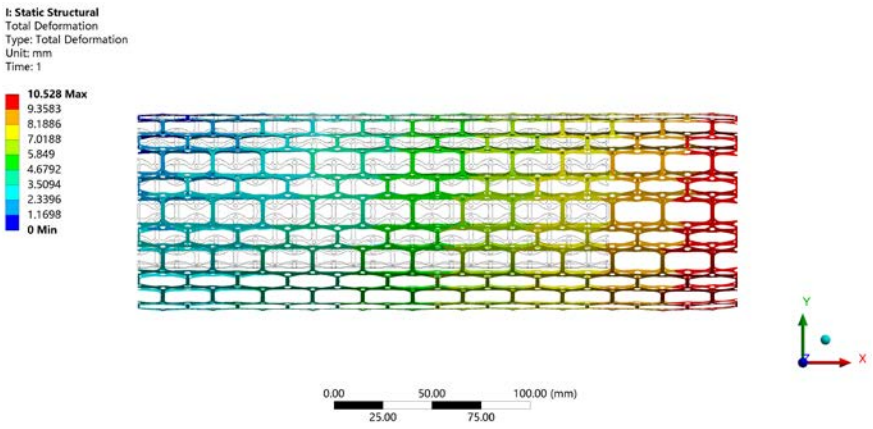

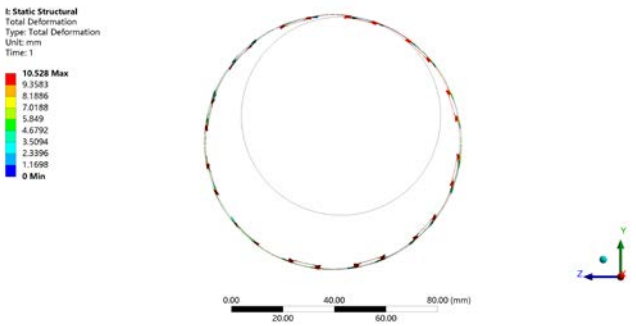

Fig.5.4 The stretching test: the front view(left) and the right view(right)

6 Conclusion

The properties of auxetic structures can well satisfy the mechanic requirements of SE coronary artery stents and enhance their abilities of dealing with the mechanical factors of ST and ISR. The stent design using parametric level set topology optimization method provides a concurrent design of both material microstructures and macro meta-structure, which benefits the stent designs for applications in practice. However, another important characteristic of the materials of SE stents is the property of shape memory, and it will influence the deformation mechanism during the expanding. Therefore, the shape memory behaviour may need to be integrated into the auxetic design of SE stent in the near future.

References

[1]Dotter, C.T. and M.P. Judkins, *Transluminal treatment of arteriosclerotic obstruction: description of a new technic and a preliminary report of its application.* Circulation, 1964. **30**(5): p. 654-670.

[2]Grüntzig, A., *Transluminal dilatation of coronary-artery stenosis.* The Lancet, 1978. **311**(8058): p. 263.

[3]Sigwart, U., et al., *Intravascular stents to prevent occlusion and re-stenosis after transluminal angioplasty.* New Engl. J. Med., 1987. **316**(12): p. 701-706.

[4]Roubin, G.S., et al., *Intracoronary stenting for acute and threatened closure complicating percutaneous transluminal coronary angioplasty.* Circulation, 1992. **85**(3): p. 916-927.

[5]Serruys, P.W., et al., *A comparison of balloon-expandable-stent implantation with balloon angioplasty in patients with coronary artery disease.* New Engl. J. Med., 1994. **331**(8): p. 489-495.

[6]Fischman, D.L., et al., *A randomized comparison of coronary-stent placement and balloon angioplasty in the treatment of coronary artery disease.* New Engl. J. Med., 1994. **331**(8): p. 496-501.

[7]Moliterno, D.J., *Healing Achilles—sirolimus versus paclitaxel*. 2005, Mass Medical Soc.

[8]Stettler, C., et al., *Outcomes associated with drug-eluting and bare-metal stents: a collaborative network meta-analysis.* The Lancet, 2007. **370**(9591): p. 937-948.

[9]Mauri, L., et al., *Stent thrombosis in randomized clinical trials of drug-eluting stents.* New Engl. J. Med., 2007. **356**(10): p. 1020-1029.

[10]Cook, S., et al., *Correlation of intravascular ultrasound findings with histopathological analysis of thrombus aspirates in patients with very late drug-eluting stent thrombosis.* Circulation, 2009. **120**(5): p. 391-399.

[11]McMahon, S., et al., *Bio-resorbable polymer stents: a review of material progress and prospects.* Progress in Polymer Science, 2018. **83**: p. 79-96.

[12]Siiki, A., J. Sand, and J. Laukkarinen, *A systematic review of biodegradable biliary stents: promising biocompatibility without stent removal.* European journal of gastroenterology & hepatology, 2018. **30**(8): p. 813-818.

[13]Kang, S.-H., et al., *Biodegradable-polymer drug-eluting stents vs. bare metal stents vs. durable-polymer drug-eluting stents: a systematic review and Bayesian approach network meta-analysis.* European heart journal, 2014. **35**(17): p. 1147-1158.

[14]Garg, S. and P.W. Serruys, *Coronary stents: current status.* J. Am. Coll. Cardiol., 2010. **56**(10 Supplement): p. S1-S42.

[15]Duerig, T., D. Tolomeo, and M. Wholey, *An overview of superelastic stent design.* Minim. Invasive Ther. Allied Technol., 2000. **9**(3-4): p. 235-246.

[16]Joner, M., et al., *Histopathologic evaluation of nitinol self-expanding stents in an animal model of advanced atherosclerotic lesions.* EuroIntervention: journal of EuroPCR in collaboration with the Working Group on Interventional Cardiology of the European Society of Cardiology, 2010. **5**(6): p. 737-744.

[17]Schatz, R.A., et al., *Clinical experience with the Palmaz-Schatz coronary stent. Initial results of a multicenter study*. Circulation, 1991. **83**(1): p. 148-161.

[18]Garg, S. and P.W. Serruys, *Coronary stents: looking forward.* J. Am. Coll. Cardiol., 2010. **56**(10 Supplement): p. S43-S78.

[19]Lakes, R., *Advances in negative Poisson's ratio materials.* Advanced Materials, 1993. **5**(4): p. 293-296.

[20]Evans, K.E. and A. Alderson, *Auxetic materials: functional materials and structures from lateral thinking!* Advanced materials, 2000. **12**(9): p. 617-628.

[21]Lakes, R., *Response: negative Poisson's ratio materials.* Science, 1987. **238**(4826): p. 551-551.

[22]Yang, W., et al., *Review on auxetic materials.* Journal of materials science, 2004. **39**(10): p. 3269-3279.

[23]Zhou, M. and G. Rozvany, *The COC algorithm, Part II: topological, geometrical and generalized shape optimization.* Computer Methods in Applied Mechanics and Engineering, 1991. **89**(1-3): p. 309-336.

[24]Bendsøe, M.P. and O. Sigmund, *Material interpolation schemes in topology optimization.* Archive of applied mechanics, 1999. **69**(9-10): p. 635-654.

[25]Xie, Y.M. and G.P. Steven, *A simple evolutionary procedure for structural optimization.* Computers & structures, 1993. **49**(5): p. 885-896.

[26]Sethian, J.A. and A. Wiegmann, *Structural boundary design via level set and immersed interface methods.* J. Comput. Phys., 2000. **163**(2): p. 489-528.

[27]Wang, M.Y., X. Wang, and D. Guo, *A level set method for structural topology optimization.* Computer methods in applied mechanics and engineering, 2003. **192**(1-2): p. 227-246.

[28]Allaire, G., F. Jouve, and A.-M. Toader, *Structural optimization using sensitivity analysis and a level-set method.* J. Comput. Phys., 2004. **194**(1): p. 363-393.

[29]Guedes, J. and N. Kikuchi, *Preprocessing and postprocessing for materials based on the homogenization method with adaptive finite element methods.* Computer methods in applied mechanics and engineering, 1990. **83**(2): p. 143-198.

[30]Sigmund, O., *Materials with prescribed constitutive parameters: an inverse homogenization problem.* International Journal of Solids and Structures, 1994. **31**(17): p. 2313-2329.

[31]Chen, J., Y. Huang, and M. Ortiz, *Fracture analysis of cellular materials: a strain gradient model*. J. Mech. Phys. Solids, 1998. **46**(5): p. 789-828.

[32]Osher, S. and J.A. Sethian, *Fronts propagating with curvature-dependent speed: algorithms based on Hamilton-Jacobi formulations.* J. Comput. Phys., 1988. **79**(1): p. 12-49.

[33]Luo, Z., et al., *Shape and topology optimization of compliant mechanisms using a parameterization level set method.* J. Comput. Phys., 2007. **227**(1): p. 680-705.

[34]Luo, Z., et al., *A level set-based parameterization method for structural shape and topology optimization.* International Journal for Numerical Methods in Engineering, 2008. **76**(1): p. 1-26.

[35]Luo, Z., L. Tong, and Z. Kang, *A level set method for structural shape and topology optimization using radial basis functions.* Computers & Structures, 2009. **87**(7-8): p. 425-434.

[36]Wendland, H., *Computational aspects of radial basis function approximation*, in *Studies in Computational Mathematics.* 2006, Elsevier. p. 231-256.

[37]Wang, X., Y. Mei, and M.Y. Wang, *Level-set method for design of multi-phase elastic and thermoelastic materials.* International Journal of Mechanics and Materials in Design, 2004. **1**(3): p. 213-239.

Physics-based Deep Neural Network for Real-Time Lesion Tracking in Ultrasound-guided Breast Biopsy

Andrea Mendizabal[1,*], Eleonora Tagliabue[2,*], Jean-Nicolas Brunet[1], Diego Dall'Alba[2], Paolo Fiorini[2], and Stéphane Cotin[1]

[1] INRIA Strasbourg
andrea.mendizabal@inria.fr
[2] Università degli Studi di Verona
eleonora.tagliabue@univr.it
* A. Mendizabal and E. Tagliabue contributed equally to the paper.

Abstract. In the context of ultrasound (US) guided breast biopsy, image fusion techniques can be employed to track the position of US-invisible lesions previously identified on a pre-operative image. Such methods have to account for the large anatomical deformations resulting from probe pressure during US scanning within the real-time constraint. Although biomechanical models based on the finite element (FE) method represent the preferred approach to model breast behavior, they cannot achieve real-time performances. In this paper we propose to use deep neural networks to learn large deformations occurring in ultrasound-guided breast biopsy and then to provide accurate prediction of lesion displacement in real-time. We train a U-Net architecture on a relatively small amount of synthetic data generated in an offline phase from FE simulations of probe-induced deformations on the breast anatomy of interest. Overall, both training data generation and network training are performed in less than 5 hours, which is clinically acceptable considering that the biopsy can be performed at most the day after the pre-operative scan. The method is tested both on synthetic and on real data acquired on a realistic breast phantom. Results show that our method correctly learns the deformable behavior modelled via FE simulations and is able to generalize to real data, achieving a target registration error comparable to that of FE models, while being about a hundred times faster.

Keywords: Ultrasound-guided Breast Biopsy · Deep Neural Networks · Real-time Simulation.

1 Introduction

Breast biopsy is the preferred technique to evaluate the malignancy of screening-detected suspicious lesions. To direct the needle towards the target, biopsy procedures are performed under image guidance, normally done with ultrasound (US) probes due to their ability to provide real-time visualization of both the

needle and the internal structures [18]. However, proper needle placement with US remains a challenging task. First, malignant lesions cannot always be adequately visualized due to the poor image contrast of US. Furthermore, navigation towards complex 3D lesion geometries is commonly achieved using 2D freehand US (FUS) systems, which provide information in a lower-dimensional space [11]. Since highly sensitive pre-operative images (such as MRI or CT) can provide accurate positions of the lesions, finding a method to update these positions from real-time US images during an intervention would highly benefit current biopsy procedures. Several commercial and research platforms have implemented image fusion techniques that align pre-operative and intra-operative data, exploiting rigid or affine registration methods [6]. However, when dealing with breast anatomy, large deformations arise due to compression forces applied by the US probe. To provide accurate probe-tissue coupling and acceptable image quality, an appropriate alignment procedure of the pre-operative and US data is required.

Accurate modelling of soft tissue deformation in real-time is a far-from-being-solved problem. Biomechanical models relying on the finite element method (FEM) realistically calculate soft tissue deformations by using a mathematical model based on continuum mechanics theory. Although these models have been successfully employed for multimodal breast image registration, they have never been applied to registration between pre-operative data and intra-operative US, due to difficulties in providing a prediction within real-time constraints [8]. This is especially true when considering large, non-linear deformations which involve hyperelastic objects, as it is the case for the breast.

In order to meet real-time compliance, various techniques have been proposed to simplify the computational complexity of FEM. Some of them have focused on optimizing linear solvers (the main bottleneck of FEM) or the formulation itself, such as corotational [5] and multiplicative jacobian energy decomposition [13]. Very efficient implementations also exist, like Total Lagrangian explicit dynamics (TLED) [15], which can achieve real-time performances when coupled with explicit time integration and GPU-based solvers [10]. Another possible option to lower the simulation time is through dimensionality reduction techniques, like Proper Orthogonal Decomposition (POD), where the solution to a high-dimensional problem is encoded as a subset of precomputed modes. The most optimized approach used to model breast biomechanics is the one proposed by Han et al. in [7], which relies on GPU-based TLED formulation. Despite the significant simulation speedup achieved, solving the FE system took around 30s, which is still not compatible with real-time. Modelling methods that do not rely on continuum mechanics laws have also been used to approximate soft tissues behavior. Among these, the position-based dynamics (PBD) approach has been used to predict breast lesions displacement due to US probe pressure in real-time, providing comparable accuracy with FE models [21]. However, not being based on real mechanical properties, such model requires an initial optimization of simulation parameters to obtain a realistic description of the deformation.

An emerging approach which has the potential of being both accurate and fast, exploits neural networks to estimate soft tissue behavior. Machine learning-based methods have proven successful to predict the entire 3D organ deformation starting either by applied surface forces [17, 22] or by acquired surface displacements [19, 1]. Being networks trained with synthetic data generated from FE simulations, they can reproduce a realistic physics-based description of the organ mechanical behavior. Using FE simulations for model training in the context of MRI-US deformable image registration has already been proposed in [9], where the authors build a statistical model of prostate motion which can account for different properties and boundary conditions. In the case of the breast, the potentiality of employing machine learning techniques has been already shown in [14], where several tree-based methods have been employed to estimate breast deformation due to compression between biopsy plates. These methods have been trained on 10 different patient geometries with a very specific FE simulation, where the upper plate is displaced vertically towards the lower one.

Similarly to works in [19, 1], we propose an approach where a neural network is trained to predict the deformation of internal breast tissues starting from the acquired surface displacements induced by the US probe. Our network can be seen as a patient-specific model. We train it on a single patient geometry before surgery, with a relatively small amount of training data. However, in contrast to the work of [14], FE simulations that compose the training set are generated with several random input displacements, making our approach able to generalize to different probe positions and compression extents.

The proposed method consists in a U-Net architecture, described in Sect. 2.2, and an immersed boundary method used for generating patient-specific simulations, described in Sect. 2.3. Results presented in Sect. 3 show the efficiency of the method when applied to both synthetic and ex vivo scenarios. Our contribution consists of a novel method to generate a real-time capable soft tissue model to improve target visualization during needle-based procedures. The position of lesions identified beforehand on pre-operative images can be updated from intra-operative ultrasound data and visualized by the surgeon in real-time.

2 Methods

This work presents a data-driven method to estimate in real-time the displacement of the breast internal structures due to probe pressure during US scanning. In our pipeline, we assume to have a patient-specific geometric model of the breast, obtained from pre-operative imaging such as MRI, and to know the position and orientation of the US probe at each time, thanks to a spatial tracking system. If the tracking coordinate system and the coordinate system of pre-operative imaging are registered, knowledge about the 3D pose and the geometry of the US probe directly allows to identify the contact surface between the breast and the probe. Since the US probe is represented as a rigid body, we can reasonably assume that when the anatomy is deformed by the probe during the image acquisition process, points on the breast surface below the US

probe will be displaced to the same exact extent as the probe itself. As a consequence, our method can predict the displacements of all the points within the anatomy given as input the displacement of the surface nodes in contact with the US probe. The decision of relying on surface displacement inferred from the spatial tracking of the US probe instead of directly tracking surface deformations (through, for example, an RGBD camera) was taken from the fact that probe-induced deformations are large but local, and the probe itself would occlude most of the deformed surface to the sensor, thus preventing an accurate estimation of the contact surface displacements.

2.1 The U-Net architecture

The objective of our work is to find the relation function f between the partial surface deformation under the US probe and the deformation inside the breast. Let $\mathbf{u_s}$ be the surface deformation and $\mathbf{u_v}$ the volumetric displacement field. In order to find f a minimization is performed on the expected error over a training set $\{(\mathbf{u_s}^n, \mathbf{u_v}^n)\}_{n=1}^N$ of N samples:

$$\min_{\theta} \frac{1}{N} \sum_{n=1}^{N} \| f(\mathbf{u_s}^n) - \mathbf{u_v}^n \|_2^2 \tag{1}$$

where θ is the set of parameters of the network f. We propose to use the same architecture as in [1], that is a U-Net [20] adapted to our application (see Fig. 1). The network consists of an encoding path that reduces the high dimensional input into a reduced space, and a decoding path that expands it back to the original shape. The skip connections transfer features along matching levels from the encoding path to the decoding path through crop and copy operations. As

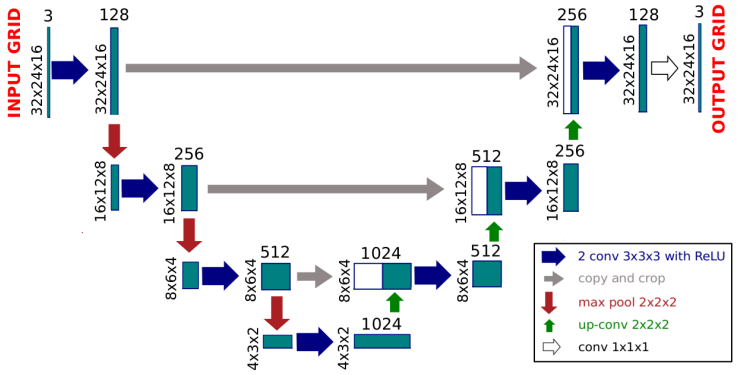

Fig. 1. U-Net architecture for a padded input grid of size $32 \times 24 \times 16$.

Fig. 1 shows, the encoding path consists of k sequences ($k = 3$ in our case)

of two padded $3 \times 3 \times 3$ convolutions and a $2 \times 2 \times 2$ max pooling operation. At each step, each feature map doubles the number of channels and halves the spatial dimensions. In the lower part of the U-Net there are two extra $3 \times 3 \times 3$ convolutional layers leading to a 1024-dimensional array. In a symmetric manner, the decoding path consists of k sequences of an up-sampling $2 \times 2 \times 2$ transposed convolution followed by two padded $3 \times 3 \times 3$ convolutions. At each step of the decoding path, each feature map halves the number of channels and doubles the spatial dimensions. There is a final $1 \times 1 \times 1$ convolutional layer to transform the last feature map to the desired number of channels of the output (3 channels in our case). The design of the U-Net is based on a grid-like structure due to this up- and down-sampling process. Hence we directly mesh our deformable object with regular hexahedral elements as explained in the next section.

2.2 Simulation of breast tissue using hexahedral grids

The training data set consists of pairs of $(\mathbf{u_s}, \mathbf{u_v})$ where $\mathbf{u_s}$ is the input partial surface displacement and $\mathbf{u_v}$ is the volumetric displacement field. Even though the data generation process takes place in an offline phase, in order to generate enough training data with FE simulations within clinically acceptable times (the intervention can be performed on the day after pre-operative scan is acquired), it is important to have simulations that are both accurate and computationally efficient.

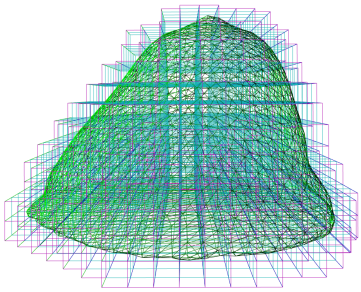

Fig. 2. Breast surface mesh obtained from a pre-operative CT scan immersed in a hexahedral grid for FEM computations.

We consider the boundary value problem of computing the deformation on a domain Ω under both Dirichlet and Neumann boundary conditions. Let Γ be the boundary of Ω (in our case, Γ corresponds to breast external surface, while Ω represents the entire breast volume). We assume that Dirichlet boundary conditions are applied to Γ_D and are a-priori known, whereas Neumann boundary conditions are applied to Γ_N, a subset of Γ that represents probe-tissue contact area and changes depending on current US probe position. In this work, training data for the network are generated by solving the discretized version of the

following boundary value problem, exploiting the FE method:

$$\begin{cases} -\boldsymbol{\nabla} \cdot \boldsymbol{\sigma} = \mathbf{0} \; in \; \Omega \\ \mathbf{u} = 0 \; on \; \Gamma_D \\ \boldsymbol{\sigma}\mathbf{n} = \mathbf{t} \; on \; \Gamma_N \end{cases} \tag{2}$$

where $\boldsymbol{\sigma}$ is the Cauchy stress tensor, $\mathbf{n}$ is the unit normal to Γ_N and $\mathbf{t}$ is a traction force applied to the boundary. Note that in (2) we neglect all time-dependent terms and we do not apply any body force like gravity, since our geometric model already accounts for the effect of gravity force. The relation between stress and strain is described through the Saint Venant-Kirchhoff model, which is the simplest and most efficient extension of a linear elastic material to the nonlinear regime. This choice is motivated by the fact that a simple linear elastic model would not be able to appropriately describe the large deformations undergone by the breast. An iterative Newton-Raphson method is used to solve the non-linear system of equations approximating the unknown displacement.

We choose to discretize the domain into 8-node hexahedral elements not only for their good convergence properties and lock-free behavior, but also because it is the required structure for the input to the network. To do that, the 3D breast geometry is embedded in a regular grid of hexahedral elements (see Fig. 2) and we use an immersed-boundary method to correctly approximate the volume of the object in the FE method computations.

2.3 Data generation

The input to the network corresponds to the displacement $\mathbf{u_s}$ of the points belonging to the breast-probe contact area. The punctual displacements are spread to the nodes of the surrounding cuboid cell through a barycentric mapping and the corresponding volume displacement $\mathbf{u_v}$ is obtained by the previously explained FE approach in response to $\mathbf{u_s}$. The data used to train the network must be representative of the application scenario and must allow the network to extract the pertinent features of the tissue behavior. In order to train our model to estimate breast volume deformation in response to pressure imposed with the US probe, we simulate several random probe-induced deformations using the following strategy:

- Select a random node p in the breast surface
- Select an oriented bounding box A centered in point p and normal to the breast surface, whose dimensions match those of the US probe lower surface, which represents current probe-tissue contact area
- Select all the surface points P falling within the box A
- Select as force direction $\boldsymbol{d}$ the normal to the surface at point p plus a random angle α ($\alpha \in \left[-\frac{\pi}{4}, \frac{\pi}{4}\right]$)
- Apply the same force $\boldsymbol{f}$ of random magnitude ($|f| \in [0.0, 0.8]$) along direction $\boldsymbol{d}$ to the P selected points simultaneously
- Store the displacement at the set of points P (input to the network) and the displacement of all the points in the volume (output to the network)

– Repeat the procedure until $N + M$ samples are generated

The choice of applying force $\boldsymbol{f}$ allowing some angle deviation from normal direction enables us to include in our dataset samples where the probe compression is not precisely normal to the surface, as it can be the case in freehand US acquisitions. The maximal force magnitude (e.g. $0.8\,N$) is set such that the amount of maximal deformation reproduced in the training dataset never exceeds too much that observed in real clinical settings. The described strategy is used to generate the set $\{(\mathbf{u_s}^n, \mathbf{u_v}^n)\}_{n=1}^{N}$ of N samples which is used to train the network, and the set $\{(\mathbf{u_s}^n, \mathbf{u_v}^n)\}_{n=1}^{M}$ of M samples which is left for validation. The training dataset is generated with the SOFA framework [3] on a laptop equipped with an Intel i7-8750H processor and 16GB RAM.

3 Experiments and Results

The network presented in this work is used to predict US probe-induced deformations of a realistic multi-modality breast phantom (Model 073; CIRS, Norfolk, VA, USA). The 3D geometry model of the phantom surface and 10 inner lesions (diameter of 5-10mm) is obtained by segmenting the corresponding CT image, relying on ITK-SNAP and MeshLab frameworks [24, 2]. A Freehand Ultrasound System (FUS) based on a Telemed MicrUs US device (Telemed, Vilnius, Lithuania) equipped with a linear probe (model L12-5N40) is used to acquire US images of the 10 segmented lesions. The dimension of the probe surface is (5x1cm). For each lesion, we acquire US images in correspondence of four different input deformations. The MicronTracker Hx40 (ClaronNav, Toronto, Canada) optical tracking system is used to track US probe in space (Fig. 3(a)). The overall probe spatial calibration error is below 1mm (± 0.7147), estimated through the PLUS toolkit [12]. Landmark-based rigid registration is performed to refer the CT-extracted 3D model, the US probe and the US images to the same common coordinate system, exploiting 3D Slicer functionalities [4]. The registration process does not only enable us to extract the breast-probe contact area, as described in Section 2, but also to know in real-time the 3D position of any point belonging to the US image. In this way, it is possible to refer lesions position extracted from US images to the 3D space.

3.1 Predict displacement on synthetic data sets

Elastic properties of the physics model used to generate training data are set in accordance with the values estimated in [23] for the same breast phantom considered in this study. However, as we are imposing surface displacements, the values of the elasticity parameters do not affect the displacement field inside the simulated volume as long as the ratio of the different stiffness values is maintained [16], thus making the method reliable for any patient specificity. Dirichlet boundary conditions are imposed by constraining the motion of all the nodes belonging to the lowest phantom surface.

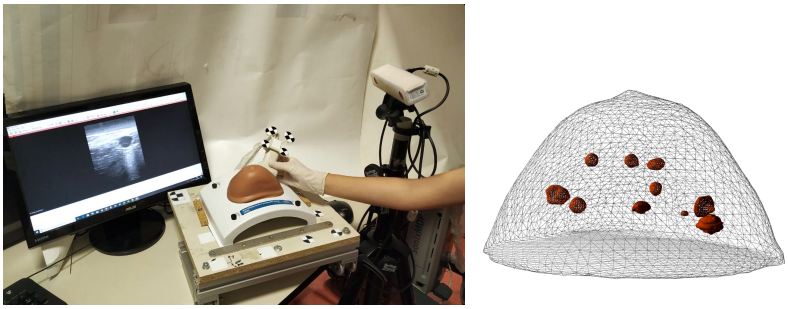

(a) (b)

Fig. 3. (a)Experimental setup. From left to right: monitor showing real-time US images; CIRS breast phantom during FUS acquisition; optical tracking system that allows to map the real positions of the CIRS breast phantom and the US probe to the pre-operative geometry model. (b)External surface and inner lesions of the CIRS breast phantom.

Using the method described in Sect. 2.2 and 2.3, we discretized the breast phantom into 2174 hexahedral elements and we simulated several probe-induced displacements. Overall we generated $N = 800$ samples for training and $M = 200$ samples for testing. The U-Net is trained in a GeForce GTX 1080 Ti using a batch size of 4, 100000 iterations and the Adam optimizer. We used a Pytorch implementation of the U-Net. To assess the learning capability of the network, we perform a statistical analysis of the *mean norm error* e over the testing data set. Let ${\mathbf{u_v}}^m$ be the ground truth displacement tensor for sample m generated using the finite element method described in Sect. 2.2 and $f({\mathbf{u_s}}^m)$ the U-Net prediction. The mean norm error between ${\mathbf{u_v}}^m$ and $f({\mathbf{u_s}}^m)$ for sample m reads as:

$$e({\mathbf{u_v}}^m, f({\mathbf{u_s}}^m)) = \frac{1}{n}\sum_{i=1}^{n} |{\mathbf{u_v}}_i^m - f({\mathbf{u_s}}^m)_i|. \tag{3}$$

where n is the number of degrees of freedom of the mesh. We compute the average $\bar{e}$, standard deviation $\sigma(e)$ and maximal value of such norm over the testing data set. The obtained results are shown in Table 1. The maximal error is of only $0.266\,mm$ and corresponds to the sample shown in Fig. 4(b). The most striking result is the small computation time required to make the predictions: only $3.14 \pm 0.56\,ms$. In contrast, the FE method takes on average $407.7 \pm 64\,ms$ to produce the solution. Obviously, the resolution of the FE mesh could be reduced to accelerate the computations but at the cost of an accuracy loss.

3.2 Predict displacement on phantom data

In our experiments, we consider one lesion at a time and we reposition the US probe on the surface of the breast such that the lesion considered is visible on the US image. In order to validate our model, we manually extract lesions position

$\overline{e}$ (mm)	$\sigma(e)$ (mm)	$\max_{m \in M} e$ (mm)	Prediction time (ms)	Total training time (min)
0.052	0.050	0.266	3.14 ± 0.56	278

Table 1. Error measures over the testing data set for a breast having 2174 H8 elements, with maximal nodal deformation of $79.09\,mm$.

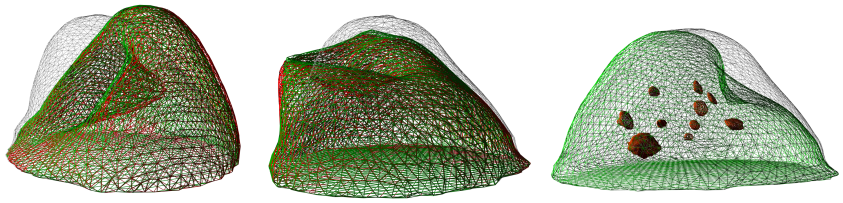

(a) (b) (c)

Fig. 4. (a) Sample with maximal deformation ($79.09\,mm$). (b) Sample with maximal *mean norm error* ($0.266\,mm$). The green mesh is the U-Net prediction and the red mesh is the FEM solution. The initial rest shape is shown in grey. (c) U-Net prediction on phantom data.

from US image acquired at rest (i.e., without applying any deformation, when the probe is only slightly touching the surface) and we consider it as a landmark to track. We then impose four deformations of increasing extent for each lesion, and we compare the U-Net-predicted displacement with real displacements extracted from US images. The comparison is performed computing target registration error (TRE) between the predicted position of the lesion and its ground-truth position. The performance of our method is compared to that of the FE model used for data generation. In Table 2 are shown the target registration errors for each phantom lesion with respect to the applied deformation. The input deformations are classified into five ranges based on the probe displacements. Displacement ranges indicated as D15, D20 and D25 have a fixed length of 5 mm each and are centered at 15, 20 and 25 mm respectively. D10 and D30 contain the extreme cases under 12.5 mm or above 27.5 mm.

Values in Table 2 highlight that the average TRE for all the tumors and for all the deformations is smaller than $6.194\,mm$ which is comparable to the maximum value obtained with the FE method ($6.080\,mm$). The average error increases with the deformation range just like in the FE method. There is no significant difference between the values of the two tables, meaning that in terms of accuracy, our method is comparable to the data generation method used to train it. In order to compute each deformation, the FE method needs about $407.7\,ms$ whereas the U-Net predicts the deformation in only $3\,ms$.

Table 2. Target registration errors in millimeters for different tumors and different deformation ranges in the breast phantom. The first table is for the proposed method, while the second table reports results obtained with the FE model used for data generation. Not-acquired data is reported as (-).

U-Net predictions

TumorID	D10	D15	D20	D25	D30	Mean	STD
1	-	1.936	2.002	1.506	3.053	2.124	0.569
2	3.211	2.905	4.068	-	4.137	3.580	0.534
3	2.032	-	4.709	7.134	10.90	6.194	3.262
4	0.505	2.225	5.313	5.903	-	3.486	2.217
5	0.932	2.768	3.454	-	4.893	3.012	1.425
6	3.923	6.349	5.625	-	6.724	5.655	1.075
7	3.454	3.864	4.543	6.710	-	4.643	1.255
8	2.422	3.261	4.320	5.136	-	3.785	1.030
9	-	3.928	4.214	4.578	4.858	4.394	0.353
10	5.529	3.272	3.940	4.846	-	4.397	0.860
Mean	2.751	3.390	4.219	5.116	5.761		
STD	1.638	1.294	1.007	1.854	2.788		

FE method

TumorID	D10	D15	D20	D25	D30	Mean	STD
1	-	1.326	2.151	2.075	3.759	2.328	0.887
2	1.956	2.738	3.945	-	4.025	3.166	0.865
3	1.595	-	4.748	7.044	10.932	6.080	3.404
4	0.755	1.991	4.544	5.120	-	3.103	1.795
5	1.029	2.863	3.330	-	4.541	2.941	1.262
6	2.579	3.409	2.871	-	2.337	2.799	0.400
7	2.605	3.219	4.095	6.750	-	4.167	1.582
8	2.695	2.748	4.321	5.411	-	3.794	1.139
9	-	2.745	2.497	2.510	4.193	2.986	0.704
10	2.916	2.542	3.015	3.868	-	3.085	0.485
Mean	2.016	2.620	3.552	4.682	4.964		
STD	0.765	0.593	0.856	1.803	2.757		

4 Conclusion

In this work we have proposed to use a deep neural network to learn the deformable behavior of the breast from numerical simulations based on the finite element method, in order to bypass the high computational cost of the FEM. Our approach represents an interface between precise biomechanical FE modeling (not capable of real time) and clinical applications requiring both high accuracy and very high speed. We have shown that our framework allows for extremely fast predictions of US probe-induced displacements of the breast during US scanning, achieving comparable accuracy to other existing methods. Therefore, it has the potential to be employed to update in real-time the estimated position of breast lesions identified on a pre-operative scan on US images, en-

abling continuous visualization of the biopsy target, even when sonography fails to render it.

Although the FE model used to train our network does not perform in real-time, its prediction delay of less than 1 s might be considered already acceptable for our specific application. However, such good computational performance is achieved since in this preliminary evaluation we use a very simplistic model, that does not account for heterogeneity or complex boundary conditions happening in clinical cases. Usage of a more complex FE model will certainly cause an increase of computation load. On the contrary, an important feature of our approach is that the prediction time remains close to 3 ms regardless of the grid resolution and of the biomechanical model used for the data generation process. This means that increasing the complexity of the model used to generate the data set will not affect the prediction speed. Moreover, our pipeline allows the method to be insensitive to patient specific elastic properties as it imposes surface displacements. It is worth noting that for inhomogeneous objects, the displacement field still depends on the ratio of the different stiffnesses [16]. Another advantage of our method is the easy meshing process. Any geometry can be embedded in a sparse grid and through the use of immersed boundary simulations the deformations are correctly estimated.

The main limitation of our method remains the training process, which is burdersome and has to be repeated for every new geometry or application. However, we have shown that a limited amount of training data can be sufficient to train a U-Net such that it obtains accurate prediction within clinically acceptable times. As a future work, we plan to use a more general training strategy leading to a network model able to predict deformations induced by any type and number of compression tools (for example, different probe shapes or the two biopsy compression plates).

Bibliography

[1] Brunet, J.N., Mendizabal, A., Petit, A., Golse, N., Vibert, E., Cotin, S.: Physics-based deep neural network for augmented reality during liver surgery. MICCAI (2019)

[2] Cignoni, P., Callieri, M., Corsini, M., Dellepiane, M., Ganovelli, F., Ranzuglia, G.: MeshLab: an Open-Source Mesh Processing Tool. In: Scarano, V., Chiara, R.D., Erra, U. (eds.) Eurographics Italian Chapter Conference. The Eurographics Association (2008)

[3] Faure, F., Duriez, C., Delingette, H., et al.: Sofa: A multi-model framework for interactive physical simulation. In: Soft tissue biomechanical modeling for computer assisted surgery, pp. 283–321. Springer (2012)

[4] Fedorov, A., Beichel, R., Kalpathy-Cramer, J., Finet, J., Fillion-Robin, J.C., Pujol, S., Bauer, C., Jennings, D., Fennessy, F., Sonka, M., Buatti, J., Aylward, S., Miller, J., Pieper, S., Kikinis, R.: 3d slicer as an image computing

platform for the quantitative imaging network. Magnetic resonance imaging **30**(9), 1323–1341 (2012)
[5] Felippa, C.A., Haugen, B.: A unified formulation of small-strain corotational finite elements: I. theory. Computer Methods in Applied Mechanics and Engineering **194**(21-24), 2285–2335 (2005)
[6] Guo, R., Lu, G., Qin, B., Fei, B.: Ultrasound imaging technologies for breast cancer detection and management: A review. Ultrasound in medicine & biology (2017)
[7] Han, L., Hipwell, J.H., Eiben, B., et al.: A nonlinear biomechanical model based registration method for aligning prone and supine mr breast images. IEEE transactions on medical imaging **33**(3), 682–694 (2013)
[8] Hipwell, J.H., Vavourakis, V., Han, L., et al.: A review of biomechanically informed breast image registration. Physics in Medicine & Biology **61**(2), R1 (2016), http://stacks.iop.org/0031-9155/61/i=2/a=R1
[9] Hu, Y., Ahmed, H.U., Taylor, Z., Allen, C., Emberton, M., Hawkes, D., Barratt, D.: Mr to ultrasound registration for image-guided prostate interventions. Medical image analysis **16**(3), 687–703 (2012)
[10] Joldes, G.R., Wittek, A., Miller, K.: Real-time nonlinear finite element computations on gpu–application to neurosurgical simulation. Computer methods in applied mechanics and engineering **199**(49-52), 3305–3314 (2010)
[11] Krücker, J., Xu, S., Venkatesan, A., Locklin, J.K., Amalou, H., Glossop, N., Wood, B.J.: Clinical utility of real-time fusion guidance for biopsy and ablation. J Vasc Interv Radiol **22**(4), 515–524 (2011)
[12] Lasso, A., Heffter, T., Rankin, A., Pinter, C., Ungi, T., Fichtinger, G.: Plus: open-source toolkit for ultrasound-guided intervention systems. IEEE Transactions on Biomedical Engineering **61**(10), 2527–2537 (2014)
[13] Marchesseau, S., Heimann, T., Chatelin, S., Willinger, R., Delingette, H.: Multiplicative jacobian energy decomposition method for fast porous visco-hyperelastic soft tissue model. In: MICCAI. pp. 235–242. Springer (2010)
[14] Martínez-Martínez, F., Rupérez-Moreno, M.J., Martínez-Sober, M., et al.: A finite element-based machine learning approach for modeling the mechanical behavior of the breast tissues under compression in real-time. Computers in biology and medicine **90**, 116–124 (2017)
[15] Miller, K., Joldes, G., Lance, D., Wittek, A.: Total lagrangian explicit dynamics finite element algorithm for computing soft tissue deformation. Communications in numerical methods in engineering **23**(2), 121–134 (2007)
[16] Miller, K., Lu, J.: On the prospect of patient-specific biomechanics without patient-specific properties of tissues. Journal of the mechanical behavior of biomedical materials **27**, 154–166 (2013)
[17] Morooka, K., Chen, X., Kurazume, R., Uchida, S., Hara, K., Iwashita, Y., Hashizume, M.: Real-time nonlinear fem with neural network for simulating soft organ model deformation. In: MICCAI. pp. 742–749. Springer (2008)
[18] O'Flynn, E., Wilson, A., Michell, M.: Image-guided breast biopsy: state-of-the-art. Clinical radiology **65**(4), 259–270 (2010)
[19] Pfeiffer, M., Riediger, C., Weitz, J., Speidel, S.: Learning soft tissue behavior of organs for surgical navigation with convolutional neural networks. IJCARS pp. 1–9 (2019)

[20] Ronneberger, O., Fischer, P., Brox, T.: U-net: Convolutional networks for biomedical image segmentation. MICCAI pp. 234–241 (2015)
[21] Tagliabue, E., Dall'Alba, D., Magnabosco, E., Tenga, C., Peterlik, I., Fiorini, P.: Position-based modeling of lesion displacement in ultrasound-guided breast biopsy. IJCARS (2019)
[22] Tonutti, M., Gras, G., Yang, G.Z.: A machine learning approach for real-time modelling of tissue deformation in image-guided neurosurgery. Artificial intelligence in medicine **80**, 39–47 (2017)
[23] Visentin, F., Groenhuis, V., Maris, B., et al.: Iterative simulations to estimate the elastic properties from a series of mri images followed by mri-us validation. Medical and biological engineering and computing **194**(21-24), 1–12 (2018)
[24] Yushkevich, P.A., Piven, J., Cody Hazlett, H., et al.: User-guided 3D active contour segmentation of anatomical structures: Significantly improved efficiency and reliability. Neuroimage **31**(3), 1116–1128 (2006)

Part 2.

Topics in patient-specific computations

Towards Visualising and Understanding Patient-Specific Biomechanics of Abdominal Aortic Aneurysms.

K. R. Beinart, G. Bourantas, K. Miller

Abstract An abdominal aortic aneurysm (AAA) is a permanent and irreversible dilation of the lower aortic region. The current clinical rupture risk indicator for AAA repair is an anterior-posterior AAA diameter exceeding 5.5 cm. This is an inadequate rupture risk indicator given that 60 % of AAAs with larger diameters than 5.5 cm often remain stable for the patient's lifetime while 20 % of smaller AAAs have ruptured. A more robust predictor of rupture risk is therefore crucial to save lives and reduce medical costs worldwide. Rupture is a local failure of the wall that occurs when local mechanical stress exceeds local wall strength. A comparison of the AAA tension and stretch during the cardiac cycle will provide the indication of wall structural integrity necessary for reliable rupture risk stratification. Employing engineering logic, mismatches between tension and stretch are likely to indicate localized wall weakening and the likelihood of rupture (e.g. a high stretch resulting from a low tension). Biomechanics based Prediction of Aneurysm Rupture Risk (BioPARR) is an AAA analysis software application that currently only determines aneurysm wall tension. This study seeks to investigate the feasibility of determining surface stretches within the AAA wall using methods compatible with clinical practices. It additionally aims to create and validate a new procedure for AAA rupture risk stratification.

Keywords abdominal aortic aneurysm, rupture, computed tomography angiography, time-resolved, four-dimensional, synthetic, tension, stretch

1. Introduction

An abdominal aortic aneurysm (AAA) is a permanent and irreversible dilation of the lower aortic region. The condition is usually symptomless and is typically detected during an unrelated procedure. If left untreated, the aneurysm can dissect or rupture with the high mortality rates of approximately 80-90 % [1]. Considering the dangers and expenses related to the surgical treatment, rupture risk classification is

essential. If this rupture risk outweighs the risk of surgery, the patient will be considered for endovascular (EVAR) or open repair surgery.

The current clinical rupture risk indicator for repair is an anterior-posterior AAA diameter exceeding 5.5 cm or a diameter growth rate greater than 1cm/year [2]. This is an inadequate rupture risk indicator given 60 % of AAAs with larger diameters than 5.5 cm often remain stable for the patient's lifetime [3] while 20 % of smaller AAAs have ruptured [4]. Additionally, AAA rupture has been linked to other risk factors, including: genetic history, smoking, high mean arterial pressure (MAP), gender, vessel asymmetry, growth of intraluminal thrombus (ILT) and increased metabolic activity [5, 6]. Simplistic conclusions based on diameter alone are thus inadequate. A more robust and reliable predictor of rupture risk is therefore crucial to save lives and reduce medical costs worldwide.

Many researchers believe that a patient specific biomechanics-based approach is a promising alternative that could significantly improve the clinical management of AAA patients. With recent advancements in medical imaging and analysis software, geometrically accurate patient specific AAA three-dimensional (3D) models can now be constructed for the purpose of computer simulations that calculate wall stress. Studies have demonstrated that peak wall stress is a better indicator of individual rupture risk compared to aortic diameter [7]. Stress alone, however, will not provide an accurate estimation of rupture risk as mechanical failure of the wall is dependent on both local wall stress and local wall strength. Vande Geest et al derived a statistical model for the non-invasive estimation of wall strength [8]. This strength model, however, is population-based, not patient specific and moreover not localized.

Many studies have utilized displacement tracking algorithms on time-resolved (4D) ultrasound scans to investigate local AAA wall deformations [9]. High local strains alone, however, cannot provide an indication of wall strength, as they may be generated by high local wall tensions.

AAA rupture is a local failure of the wall that occurs when local mechanical stress exceeds local wall strength [10]. This study proposes that a comparison of AAA tension with stretch during the cardiac cycle will provide the indication of wall structural integrity necessary for reliable rupture risk stratification. It is hypothesized that mismatches between local tension and resulting tangential stretch, such as high stretch with low tension, indicate localised wall weakening and the likelihood of rupture.

Biomechanics based Prediction of Aneurysm Rupture Risk (BioPARR) is an existing, free and semi-automatic AAA analysis software application that currently only determines aneurysm wall tension [11]. This study seeks to investigate the feasibility of determining surface stretches within the AAA wall using methods compatible

with clinical practice. It additionally aims to validate the approach of pairing surface stretches with tension as a measure of AAA rupture potential.

A variety of approaches have been utilized by researchers to obtain ground truth data for validation purposes. Most methods are inaccurate and inefficient due to the errors introduced by reference tracking algorithms, sparse location of reference markers and the bias introduced by these markers on the tracking problem. Additionally, fabrication of physical phantoms to simulate realistic physiological deformation is both challenging and expensive.

Synthetic data provides a valuable reference for assessing the accuracy of tracking algorithms due to knowledge of the exact deformation. In this case, the reference displacement field is unbiased by any motion estimation algorithm. Additionally, exact deformation is known at each voxel. Furthermore, a wide range of digital data can easily be created by researchers thus eliminating the requirement for complex experimental phantoms. The usefulness of synthetic data as a validation tool, however, is highly dependent on the degree of realism of the generated synthetic scans.

One method of creating synthetic datasets involves the use of algorithms that simulate the physics of the imaging process. Models of virtual patient anatomy can consequently be 'imaged' using these projection algorithms. Models of the patient anatomy are only simplified geometries that have been mathematically derived and are therefore largely unrealistic. Furthermore, the organs and substructures are modelled as homogenous with constant pixel intensity. Image artefacts introduced by the heterogenous tissues are not simulated [12]. Therefore, although these phantoms can be used for dosimetry studies, they are inadequate for reliably assessing techniques dependent on image quality.

In the pursuit of increasingly realistic synthetic data, new techniques use biomechanical models extracted from the segmentation of real patient anatomy. A single static real medical scan is then warped with the deformation field of this model [13]. The use of real scans enables more accurate synthetic data creation by accounting for the heterogeneous tissue voxel intensities. Exact and simple methods to achieve this have not been clearly outlined in the literature. Additionally, these methods have mainly been restricted to the modelling of cardiac motion using only echocardiography and MRI [13]. This study therefore additionally aims to extend the existing literature by developing and clearly outlining simple methods for the simulation of realistic CT images using open source software for the given application of AAA.

2. Methods

2.1. Synthetic Data

A simple method of creating a synthetic 4D CT dataset was developed. This was achieved by warping a static CT scan using the transformation matrices obtained after modelling the pulsatile motion of the abdominal aortic aneurysm geometry.

One abdominal aortic aneurysm computed tomography angiography DICOM scan was provided by Dr Hozan Mufty of UZ Leuven academic hospital, Belgium. A 3D model of the AAA was created by segmenting the CT scan in 3D Slicer 4.10.1, a free open source medical image analysis and visualization software package.

The outer wall of the abdominal aortic aneurysm model was imported into Abaqus Explicit 2018. This was taken as the geometry that had been pre-loaded with the diastolic pressure. A linear tetrahedral element mesh was used due to its compatibility with Abaqus Explicit. The mesh contained approximately 4×10^6 nodes. The simulation consisted of a periodic loading cycle using an internal pulsatile pressure of 10 kPa. This represents a high pulse pressure that would realistically be observed in AAA patients. The upper and lower ends of the aneurysm were constrained in all directions using fixed boundary conditions (Figure 1). Non-linear, hyper-elastic material properties were used to model the aneurysm tissue using the strain energy function presented by Raghavan and Vorp [14]. This strain energy function (W) shown below, was obtained by the researchers after examining the mechanical properties of excised AAA tissue.

$$W = a(I_{1c} - 3) + b(I_{1c} - 3)^2 \quad (1)$$

a and b are the material properties and I_{1c} is the first invariant of the right Cauchy-Green tensor. Most of the aneurysm tissue was modelled using a=113.4 kPa, b=9.2 kPa and a density of 1000 kg/m^3 [15]. A randomly chosen local region of the aneurysm model was purposely weakened by halving each of these material parameters. In addition to location, the extent and range of weakening was arbitrarily selected. The local weakened and healthier tissue regions are indicated in Figure 1 in red and green respectively.

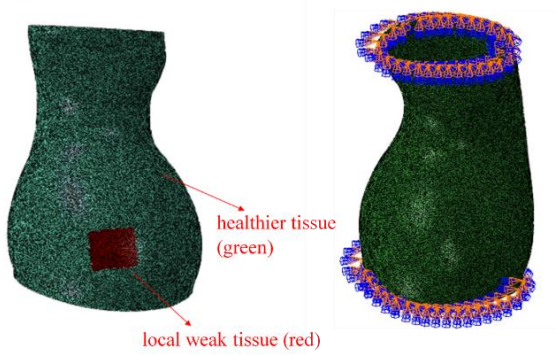

Figure 1. Left: The local weakened (red) and healthier (green) tissue regions of the model. Right: Fixed Boundary Conditions applied to the ends of the AAA model.

Mesh nodal coordinates from five phases of the pulsating biomechanical model, between the two extremes of 'diastole' and 'systole', were extracted and exported from Abaqus to 3D Slicer. The transformation matrices, mapping each of the nodal coordinates from phase 0 to each of the respective phases, were obtained using the 'Scattered Transform' module [16]. The module interpolates displacements at nodes using a BSpline Algorithm. Once the transformation matrices were obtained, the 4D synthetic dataset was created using the 'Data' module. The initial CT scan was warped by each of these transformation matrices after dragging and dropping it onto the relevant transform. The new CT frames were then saved by hardening the transforms onto the volume. This resulted in a stack of synthetic CTs corresponding to each phase of the pulsating biomechanical model.

2.2. Voxel Displacement Tracking

As an alternative to producing an in-house code for the implementation of the displacement tracking techniques, open-source tools are available, such as those used for the registration of medical scans. Registration is the task of mapping one image to another image. This is typically used by clinicians to align scans of different modalities, or even align scans taken at different points in time such as for follow up procedures. Registration can therefore also be used to determine displacements of the aneurysm wall from scans at different points in time during the cardiac cycle.

Thirion proposed the Demons algorithm for non-rigid registration [17]. The Diffeomorphic Demons algorithm minimizes the sum of square differences of intensity, contains a smoothness constraint and additionally limits the transformation to be one-to-one. The Demons algorithm embodies a computationally efficient simplification of the optical flow problem.

The Demons Diffeomorphic Registration was implemented in 3D Slicer using the 'BRAINSDemonWarp' module. A course-to-fine pyramidal approach was utilized using 5 pyramid levels. A shrink factor of 16 and iteration count of 300, 50, 30, 20 and 15 for each respective pyramid level was employed. Linear interpolation and a Diffeomorphic Registration Filter were used. These parameter settings produced the most accurate results when visually compared with ground truth.

Each synthetic CT frame was registered to the initial frame. The outputs of these registrations were transformation matrices mapping points from one image to the next. The transformation matrices were then converted to displacement fields in the 'Transforms' module. Using the 'Probe Volume' module, the displacement field was then overlayed onto the surface of the segmented aneurysm geometry.

2.3. Determining Maximum Principal Stretch

The point coordinates of the AAA surface and the displacements at these nodes were read into MATLAB. An in-house modified moving least squares (MMLS) code was utilized in order to determine the deformation gradient from these nodal displacements [18].The deformation gradient (F) was obtained by determining the derivative of the displacement vectors with respect to the undeformed configuration (X) and adding the identity matrix (I):

$$F = I + \frac{\partial u}{\partial X} \tag{2}$$

Additional code was added in order to determine the principal stretches. We computed the right Cauchy Green strain tensor: $C=F^TF$. Eigenvalues of the right Cauchy Green strain tensor are the square of the principal stretches. The maximum principal tangential stretches and its directions were obtained after aligning the minimum eigenvectors with the surface normals. This is compatible with reality whereby the aorta wall will compress radially but stretch tangentially when it is inflated by the blood pressure.

2.4. Determining Maximum Principal Tension

The Maximum Principal Tension was determined via BioPARR utilizing the following inputs: a constant wall thickness of 1 mm, 16 kPa pressure applied to the interior AAA surface representing the patient's mean arterial blood pressure and a

ten-node tetrahedral hybrid element (C3D10H) mesh. The ‘no ILTP’ case was modelled. This case ignores the intraluminal thrombus and loads the interior surface of the AAA with blood pressure. This was done for simplicity and because the ILT was neglected when modelling the AAA motion.

2.5. New Rupture Risk Index

The MATLAB code was additionally updated to read-in the maximum principal tensions obtained from BioPARR. A structural integrity index (SII) was created by dividing the maximum principal tension by the largest maximum principal stretch during the cardiac cycle. A relative structural integrity index map (RSII) was created by dividing the SII map by the maximum structural integrity index over the AAA volume. This enables clear visualization of weakened areas by comparing all the structural integrity indices over the AAA volume with the strongest tissue present.

2.6. Validation of Techniques

The technique was validated by correlating displacements and maximum principal stretches obtained from 4D CT registration with the ground truth values obtained from Abaqus. This was implemented for each phase of the cardiac cycle. A Pearson correlation test was conducted in Excel with significance evaluated using a p-value of 0.05. Similarity to ground truth was also observed by visualizing displacements and maximum principal stretches in Paraview, an open-source data analysis and visualization application.

This new rupture risk predictor was then validated by determining if the randomly located purposely weakened area of the model was detected. This was achieved by visualizing relative structural integrity indices below 0.15 using Paraview. This represents the weakest 15 % of tissue within the AAA.

3. Results

3.1. Validation of Displacement tracking

A high similarity was observed between the ground truth displacement fields obtained via Abaqus and that obtained from registration of the synthetic 4D CT scans. This is depicted in Figure 2 which displays the tangential displacement fields of the abdominal aortic aneurysm model during one phase of the cardiac cycle. This is additionally indicated by the high Pearson's correlation coefficients of displacement magnitudes (R=0.986, 0.990, 0.993, 0.996, 0.998, $p<0.001$) and directions for each of the respective phases analysed (Table 1).

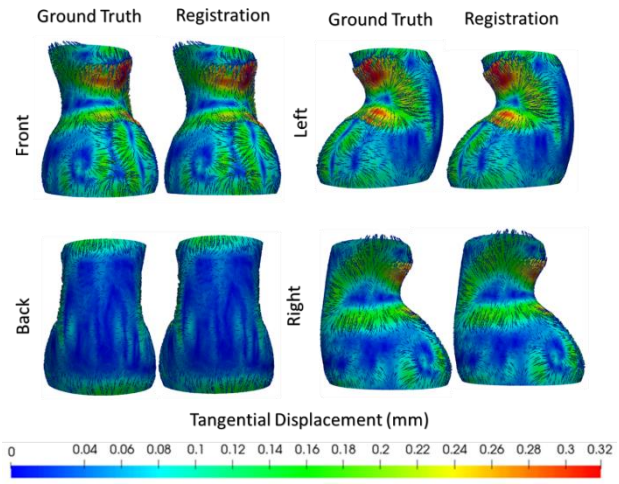

Figure 2. Tangential displacements of the abdominal aortic aneurysm model during one phase of the cardiac cycle.

Table 1. Correlation coefficients for each phase of the cardiac cycle

Frame	Correlation (X)	Correlation (Y)	Correlation (Z)	Correlation (magnitude)	P-value
1	0.99961	0.99930	0.99575	0.98571	P<0.001
2	0.98952	0.99934	0.99628	0.98952	P<0.001
3	0.99971	0.99952	0.99674	0.99347	P<0.001
4	0.99976	0.99966	0.99722	0.99602	P<0.001
5	0.99975	0.99965	0.99684	0.99750	P<0.001

3.2. Maximum Principal Stretches

A high similarity was also observed between maximum principal stretches obtained from registered synthetic 4D CT scans and ground truth stretches obtained via Abaqus. This is evident in Figure 3, where for each of the phases analyzed, stretch magnitudes and patterns obtained via registration are comparable to ground truth.

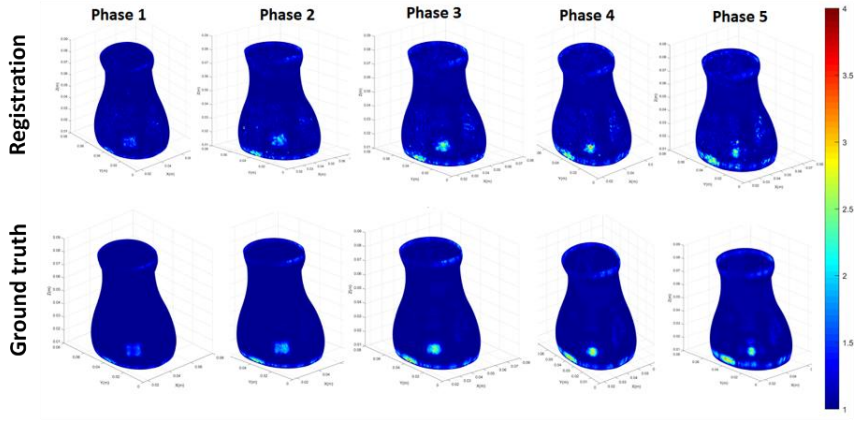

Figure 3. Maximum Principal Tangential Stretch of the abdominal aortic aneurysm model during each phase, obtained via Abaqus (bottom) and registration of 4D synthetic CT scans (top).

3.3. Relative Structural Integrity Index (RSII)

The largest maximum principal stretch during the cardiac cycle was then paired with the maximum principal tension obtained from BioPARR to compute the relative structural integrity index (RSII). A correlation analysis between the ground truth and registered RSII distributions indicated that good agreement was obtained ($R=0.98$, Pearson's correlation, $p<0.001$). As evident in Figure 4, an illustration of the lowest 15 % of RSII successfully identifies the purposely locally weakened tissue depicted in Figure 1.

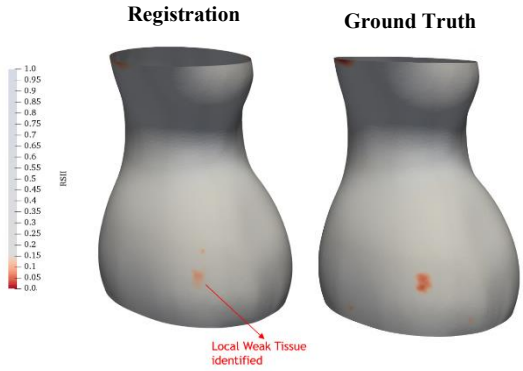

Figure 4. Lowest 15 % of relative structural integrity indices (RSII) of the aneurysm model

4. Discussion

This study has successfully developed a procedure to accurately determine surface stretches within the AAA wall using methods compatible with clinical practices.

Most researchers have focused on utilizing time-resolved ultrasound to determine deformation of AAAs. This study has highlighted the feasibility of using 4D CT as an alternative. This is compatible with clinical workflow due to the current practice of employing 3D CT angiography for preoperative imaging of the AAA. Unlike ultrasound, 4D CT additionally enables quick, repeatable acquisition of the full volume of the AAA.

The use of the Demons Diffeomorphic registration technique to track deformation during the cardiac cycle from 4D CT scans was validated. The obtained displacements and resulting stretches were highly accurate with strong correlation to ground truth.

This novel study has introduced a new and improved rupture risk metric. The RSII utilizes a holistic engineering approach by accounting for both local stretches and tensions to enable the characterization of tissue integrity local to the AAA. This enables a patient specific measure of wall strength that other procedures have not considered. Even if stresses are computed correctly, high stresses alone cannot be interpreted as a loss of wall structural integrity without knowledge of local wall strength. i.e. clearly high wall stress is not an issue if it is present in a strong wall. Similarly, methods utilizing only high stretch as a measure of tissue integrity are flawed. These local high stretches may be generated by local high tensions and may

not be due to weakened tissue. The RSII was validated by illustrating that a randomly located, purposely weakened area of the model was detected with high accuracy. These findings have advanced the state of the art of AAA management.

This method of creating a synthetic 4D CT sequence has granted access to the required data to test the feasibility of determining surface stretches within the AAA wall, without reliance on a clinic. It additionally enabled accurate knowledge of ground truth values and thus the ability to reliably assess the novel techniques used. This essential validation step would not have been possible with real patient data where access to exact ground truth is unattainable. Synthetic data provides a reference displacement field that is unbiased to any motion estimation algorithm. This is unlike that required by intermodal registration reference methods and techniques relying on the tracking of implanted markers. Unlike previous methods that utilise sparsely located reference markers, the technique used in this study provides knowledge of exact deformation at each voxel. Furthermore, the simple, low cost computer-based biomechanical model is more realistic compared to other mock-ups such as complicated physical phantoms, due to easier control of material properties and pressures. This opens the door to the generation of a wide range of synthetic data, from normal to varying diseased states, as demonstrated by this AAA study. The usefulness of synthetic data as a validation tool, however, is highly dependent on the degree of realism of the generated sequence. Unlike synthetic datasets created using projection algorithms, this study uses methods that produce realistic synthetic data. This was achieved by using real scans to extract exact patient anatomy and to simulate the heterogenous voxel intensities of imaged tissue.
The simple and easily accessible methods developed in this study can similarly be used by other researchers to progress pilot studies without being impeded by clinical bureaucracy. Additionally, the flexibility offered by this simple technique provides a platform to optimize and validate emerging technologies and methods without being impeded by the multitude of external restrictions imposed by the other validation techniques discussed.

Limitations, however, do exist in the presented work. This method of synthetic CT creation does not completely take the physics of image acquisition into account. Instead it re-uses the same texture of the initial CT, which is warped according to the differences between the original scan and the simulated motion. Changes in the geometry of the moving organ, however, will alter the path length along which the radiation travels through the organ. This will cause variations in voxel intensity throughout the cardiac cycle. The change in voxel intensity during deformation is not reflected in the synthetic data creation technique discussed.

One method discussed in the literature partly accounts for this by using a template 4D DICOM dataset to partially increase the degree of realism of the generated synthetic sequence [19]. This is achieved by spatio-temporal alignment of the template

sequence with the biomechanical model. In this method instead of warping a single static scan at the initial phase of the cardiac cycle, the template scan is warped by the biomechanical model at each of the respective phases. This partially accounts for the change in intensities that will be present as a result of deformation because it reduces the difference between the reference and deformed frames. The risk of unrealistic texture warping does, however, still exist with this method when the simulated motion of the model deviates too far from the template motion. That method, however, requires the presence of an initial 4D dataset. In novel studies such as this one, access to an initial 4D dataset is not always possible. A 4D CT protocol of the AAA is not yet utilized in the clinic. Once access to real data from this protocol is achieved, a future study can further validate the methods used by implementing this improved technique.

A basic assumption made using the Demons algorithm is that the intensity of voxels remains constant through time. The geometry of the aneurysm, however, will be changing during the cardiac cycle, which, as discussed, will alter voxel intensities. Since this synthetic data is slightly unrealistic in that the intensity of voxels remains constant despite motion, the methods used on this artificial dataset are acceptable. When using real data, however, this may not remain true. An option for dealing with this issue could be to not register each frame to the initial frame, as was done using this synthetic dataset. Instead one could register each frame to the previous frame but use the preceding transform as an initialization to the registration. This would enable the constant intensity assumption to hold true as the geometry between consecutive frames would not change significantly.

The next step required to progress this novel technique into normal clinical practice is an initial pilot study using real patient data. Further studies will need to establish the relationship between RSII and the progression of abdominal aortic aneurysms using follow up analyses.

Acknowledgements The authors wish to acknowledge help from Dr Grand Roman Joldes, Dr Mark Teh (Director of Training, Radiology, SCGH), Dr Benjamin Khoo (Medical Physicist, SCGH), Dr Toby Richards (HoD of Vascular Surgery, Fiona Stanley Hospital), Dr Hozan Mufty (Vascular Surgeon, UZ Leuven academic hospital) and Dr Abdul Maher (Vascular Surgeon, SCGH).

References

1. Hoornweg, L.L., et al., *Meta Analysis on Mortality of Ruptured Abdominal Aortic Aneurysms.* European Journal of Vascular and Endovascular Surgery, 2008. **35**(5): p. 558-570.

2. Doyle, B.J., et al., *On the influence of patient-specific material properties in computational simulations: A case study of a large ruptured abdominal aortic aneurysm.* International Journal for Numerical Methods in Biomedical Engineering, 2013. **29**(2): p. 150-164.
3. Farotto, D., et al., *The role of biomechanics in aortic aneurysm management: requirements, open problems and future prospects.* J Mech Behav Biomed Mater, 2018. **77**: p. 295-307.
4. Nicholls, S.C., et al., *Rupture in small abdominal aortic aneurysms.* Journal of Vascular Surgery, 1998. **28**(5): p. 884-888.
5. Sakalihasan, N., et al., *Positron Emission Tomography (PET) Evaluation of Abdominal Aortic Aneurysm (AAA).* European Journal of Vascular and Endovascular Surgery, 2002. **23**(5): p. 431-436.
6. Gasser, T.C., et al., *A novel strategy to translate the biomechanical rupture risk of abdominal aortic aneurysms to their equivalent diameter risk: method and retrospective validation.* Eur J Vasc Endovasc Surg, 2014. **47**(3): p. 288-95.
7. Vorp, D.A., *Biomechanics of abdominal aortic aneurysm.* J Biomech, 2007. **40**(9): p. 1887-902.
8. Vande Geest, J., et al., *Towards A Noninvasive Method for Determination of Patient-Specific Wall Strength Distribution in Abdominal Aortic Aneurysms.* Annals of Biomedical Engineering, 2006. **34**(7): p. 1098-1106.
9. Karatolios, K., et al., *Method for aortic wall strain measurement with three-dimensional ultrasound speckle tracking and fitted finite element analysis.* Ann Thorac Surg, 2013. **96**(5): p. 1664-71.
10. Gasser, T.C., *Biomechanical Rupture Risk Assessment: A Consistent and Objective Decision-Making Tool for Abdominal Aortic Aneurysm Patients.* AORTA Journal, 2016. **4**(2): p. 42-60.
11. Joldes, G., et al., *BioPARR: A software system for estimating the rupture potential index for abdominal aortic aneurysms.* Sci Rep, 2017. **7**(1): p. 4641-4641.
12. Lowther, N., et al., *Investigation of the XCAT phantom as a validation tool in cardiac MRI tracking algorithms.* Physica Medica: European Journal of Medical Physics, 2018. **45**: p. 44-51.
13. Clarysse, P., et al., *Simulation based evaluation of cardiac motion estimation methods in tagged-MR Image sequences.* Journal of Cardiovascular Magnetic Resonance, 2011. **13**(Suppl 1): p. P360-P360.
14. Raghavan, M.L. and D.A. Vorp, *Toward a biomechanical tool to evaluate rupture potential of abdominal aortic aneurysm: identification of a finite strain constitutive model and evaluation of its applicability.* Journal of Biomechanics, 2000. **33**(4): p. 475-482.
15. Satriano, A., et al., *In vivo strain assessment of the abdominal aortic aneurysm.* Journal of Biomechanics, 2015. **48**(2): p. 354-360.

16. Joldes, G.R., et al., *Performing brain image warping using the deformation field predicted by a biomechanical model*. 2012: Springer New York. 89-96.
17. Thirion, J.P., *Image matching as a diffusion process: an analogy with Maxwell's demons.* Medical Image Analysis, 1998. **2**(3): p. 243-260.
18. Joldes, G.R., et al., *Modified moving least squares with polynomial bases for scattered data approximation.* Applied Mathematics and Computation, 2015. **266**(C): p. 893-902.
19. Duchateau, N., et al., *Model-Based Generation of Large Databases of Cardiac Images: Synthesis of Pathological Cine MR Sequences From Real Healthy Cases.* IEEE Trans Med Imaging, 2018. **37**(3): p. 755-766.

Pipeline for 3D reconstruction of lung surfaces using intrinsic features under pressure-controlled ventilation

Samuel Richardson[a], Thiranja P. Babarenda Gamage[a] , Toby Jackson[a], Amir HajiRassouliha[a], Alys Clark[a], Martyn P. Nash[a,b], Andrew Taberner[a,b], Merryn H. Tawhai[a], Poul M.F. Nielsen[a,b]

a Auckland Bioengineering Institute, University of Auckland, New Zealand
b Department of Engineering Science, University of Auckland, New Zealand

Abstract

The measurement of whole lung mechanics forms the basis of diagnostic measurements for many respiratory diseases. Despite this, there are currently no quantitative methods to link alterations in pulmonary microstructures to measurements of whole lung function. The normal decline in the lung's microstructure that occurs with age is virtually indistinguishable from early disease on imaging or standard lung function measurements, leading to frequent misdiagnosis in the elderly. Accurate characterisation of lung mechanics across spatial scales has the potential to assist distinguishing age from pathology, which would benefit patients across a range of medical conditions and procedures. While computational modelling promises to be a useful tool for improving our understanding of lung mechanics, there is currently no unified structure-function computational model that explains how age-dependent structural changes translate to decline in whole lung function. This paper presents novel instrumentation and imaging techniques for measurements of intact *ex vivo* lung tissue mechanics. We seek to address problems of weak parameterisation that existing models suffer from, due to lack of reliable measurements. To begin addressing this issue, we have developed a full-field stereoscopic imaging system for tracking surface deformation of the rat lung during pressure-controlled ventilation. This study presents a pipeline for the reconstruction and tracking of the intact left lobe of a rat lung during inflation, *ex vivo*. Model-based 3D reconstruction of the lungs enabled the 3D shape of a surface patch of the imaged lung to be determined. The 3D reconstruction and tracking of the fresh lung surface patch in this study was completed with three cameras across 21 pressure steps, encompassing a total pressure change from 2069 Pa to 2386 Pa. This approach shows that reconstructing intact *ex vivo* fresh lungs, with no additional surface markers, is feasible.

1. Introduction

Despite the importance of the lungs in delivering oxygen to the body, aspects of their mechanics remain poorly understood [1]. A key reason for this is that any disruption of the lung structure results in a change in the mechanical response of the tissue, making traditional mechanical testing poorly suited to investigating lung tissue [2]. Many studies have attempted to characterise the mechanics of lung tissues, however, it was not until the middle-to-late 20th century that respiratory mechanics began to be studied as a separate field, and it was during this time that the majority of our understanding was developed [3, 4]. Despite advances in imaging technologies, fundamental questions concerning key processes that occur in the lungs remain unanswered. For example, there is no unifying theory for alveolar dynamics and recruitment during respiration. It remains unclear if the alveoli expand isotropically, heterogeneously, or by a combination of both [5]. This has been debated in the literature, with consensus being hindered by difficulties in imaging the small and constantly moving alveoli during respiration.

Computational modelling may prove to be a useful tool for improving our understanding of lung mechanics, and several computational models have been proposed for the mechanics of lung tissue. However, there is currently no unified structure-function computational model that explains how age-dependent structural changes translate to decline in whole lung function. Existing models suffer from weak parameterisation due to lack of available data. In this study, we designed a real-time full field stereoscopic imaging system for tracking lung surface deformation under pressure-controlled inflation. This system will enable us to acquire rich, accurate, robust, and previously unavailable physiological data on lung tissue mechanics from whole rat lungs, that can ultimately be used to parameterise computational models of lung mechanics.

2. Methodology

2.1 Lung Ventilation

Fresh post-mortem lungs were acquired from female (350 ± 50) g Sprague-Dawley rats, after the animals were sacrificed following separate experimental studies that did not involve the chest cavity. The Sprague-Dawley strain was chosen for two key reasons: similarities to humans in alveolar air-space enlargement with age [6]; and their relatively large alveoli (~90 μm diameter) [6] compared with lung size (~20 mL). A cannulated rat lung is shown in Fig 1.

A CompactRio (National Instruments) based real time pressure control system was developed to control the inflation of the lungs. A syringe pump enabled real time pressure control, with volume and pressure resolutions of ±5 μl and ±5 Pa

respectively. A 100 ml glass syringe was mounted and actuated by a Physik Instrumente DC-Mike linear actuator that has an encoder resolution of 0.0592 µm.

During stereoscopic imaging of the lungs, images were captured at regular intervals corresponding to increments/decrements in pressure of 15 Pa. Fig 2 shows the pressure-volume (PV) loops from the stereoscopic measurement of the lung lobe. The imaged inflation cycle (red in Fig 2) shows three cycles between 2000 Pa and 3000 Pa. The PV loops between 2000 Pa and 3000 Pa are approximately linear, with a small amount of hysteresis visible between 2800 Pa and 3000 Pa. There was an increase in lung volume of 0.2 mL across the three loops, when comparing the volumes at 2000 Pa.

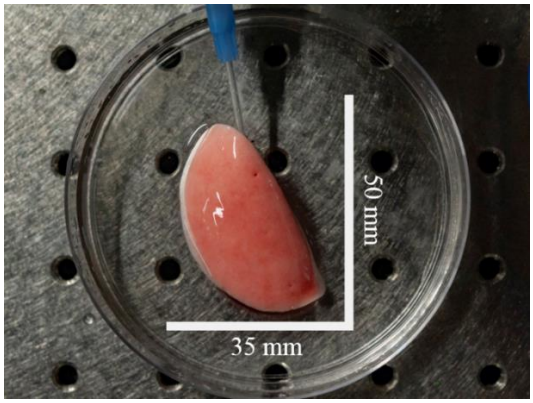

Fig 1. Inflated left lung lobe held at 3000 Pa, in a Petri dish full of phosphate buffered saline solution and cannulated with a plastic 16 Gauge blunted needle.

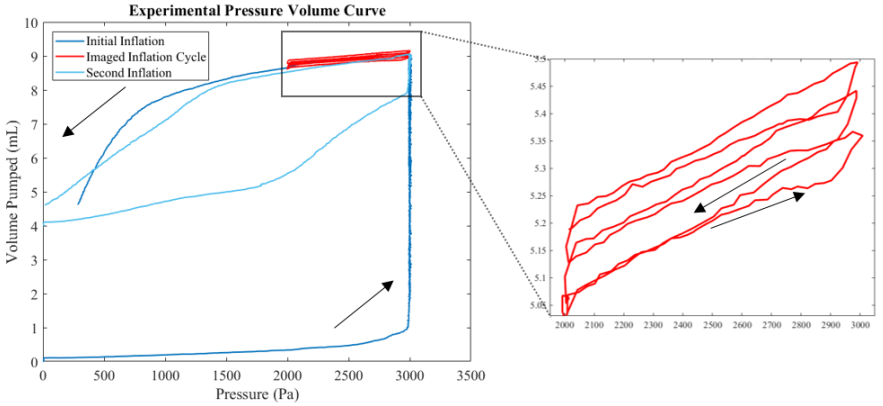

Fig 2. Left, PV loops from two full range inflations and an imaging cycle of three PV loops from 2000 Pa to 3000 Pa and back. Arrows depict the direction of increasing time. Right, expanded view of the three PV loops used for imaging.

2.2 Lung Surface Imaging

A 12 camera full field stereoscope was designed and built in-house to enable imaging of the surface displacement of the lung during pressure-controlled inflation. FLIR BlackflyS monochrome cameras that feature a SONY IMX250 sensor were selected for imaging the lung due to their high quantum efficiency and high signal to noise ratio (4760 signal to noise ratio or 73 dB dynamic range). The sensors had a 2448 pixel × 2048 pixel resolution (5.0 MP) with a 3.45 µm pixel size and were capable of imaging at 75 frames per second. The control code for these cameras was written in LabView (National Instruments), enabling data from all 12 cameras to be saved concurrently.

To ensure accurate 3D reconstruction of the imaged objects, the cameras were calibrated to find their intrinsic and extrinsic parameters, and the mounting of the cameras was designed for rigidity, to ensure that the cameras remain fixed relative to one another. The design and construction of this stereo system has been described previously for eight cameras [7]. Several modifications have been made since this was previously reported and are presented in the following sections.

2.2.2 Stereo Rig Construction

A rigid camera frame was designed in Solidworks. To ensure sufficient rigidity between the cameras, the geometry of the camera frame was designed as a regular octahedron, as shown in Fig 3. To ensure consistent lighting, eight high-power 1270 lm LED Engin LZ1-10R200 light emitting diodes were used with diffusers to ensure even lighting and to reduce noise in the camera images. Image acquisition from the cameras was performed in LabVIEW and the cameras were synchronized using a hardware trigger from the pressure control FPGA. This enabled images to be triggered, based on changes in pressure.

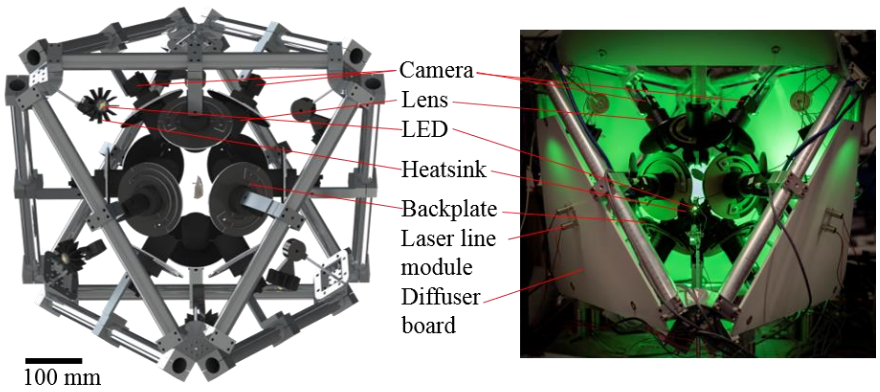

Fig 3. Frame constructed for performing full-field imaging of the lung surface during pressure-controlled inflation experiments. Left shows a CAD rendering of the stereo rig, Right shows the physical rig.

Lungs were dissected from the rats *en bloc*, with the heart and trachea attached. The heart and right lobes were removed, leaving the left lobe and a length of bronchus for cannulation. After cannulation of the lungs onto a blunted needle, they were attached to the syringe pump system. This enabled the initial inflation of the lungs from their collapsed state. The lungs were inflated to a pressure of 3000 Pa and held at that pressure until fully inflated. After a full inflation/deflation cycle, the lungs were bathed in phosphate buffered saline (PBS) to ensure that they remained hydrated. Post hydration, the lungs were mounted into the centre of the stereo camera system.

2.2.3 Stereo Rig Calibration

Camera calibration is necessary to achieve high accuracy imaging and 3D reconstruction. The accuracy of any 3D measurement made with a stereo imaging system depends, in part, on the accuracy of the calibration of the stereo cameras. The process of calibrating a camera system is a complex problem, which grows in complexity with every additional camera. The calibration method used in this study was developed by HajiRassouliha *et al* [8] using a checkerboard calibration template. This has been described by HajiRassouliha *et al* in [8] for cameras where all cameras could see the same calibration template. In this study, we extended the calibration approach to allow for calibration of all cameras in the stereo rig. This involved calibrating overlapping groups of four cameras, followed by an alignment of the calibrated cameras sets using a 3D triangular template with three white cellulose precision microspheres of a known diameter attached to each of its vertices. The diameters and spacing between spheres were identified using micro-CT imaging with a resolution of 2.7 μm.

2.2.4 Initial Surface Reconstruction

The first step in an inflation was to acquire images of the *ex vivo* lung while it was illuminated by a laser line, as depicted in Fig 4. Images including laser lines were acquired without LED illumination These data were used to generate an initial 3D reconstruction of the lung shape. This involved segmenting and fitting the laser lines on the lung lobe using piecewise cubic splines in each of the 2D images from each camera view. The pixel coordinates of these splines were triangulated into 3D space by determining their locations across multiple cameras using an intersecting ray approach, as described in [11], with the requirement that four rays intersect for a point to be considered valid. This resulted in a 3D point cloud which described the surface of the lung.

Immediately after laser line data acquisition, the lungs were cyclically inflated and deflated for imaging.

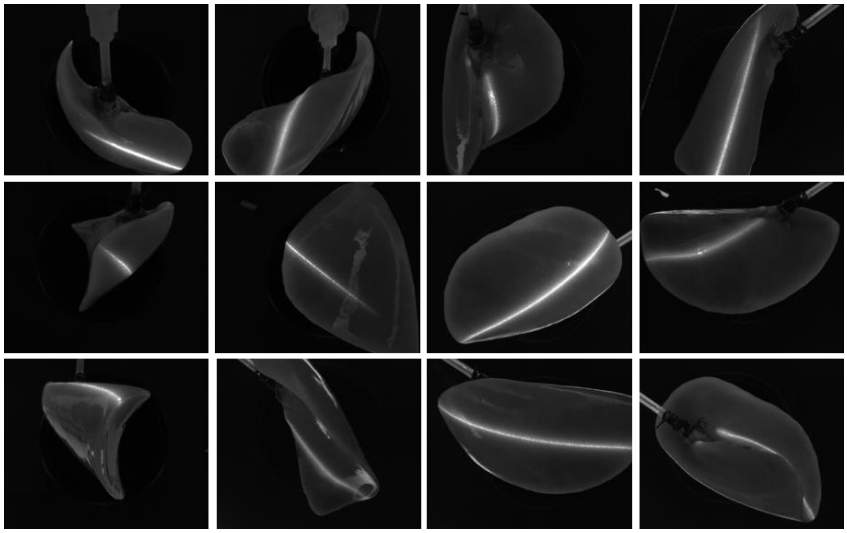

Fig 4. Examples of laser line images. The lungs were held at a fixed pressure while each line was acquired individually. In this data set, the lungs were held at 2000 Pa. Firstly, images of the lungs were taken at different levels of illuminations from LEDs, then 22 images were recorded of individual laser lines on the lungs.

2.3 Lung Fixing and Micro Computed Tomography (CT) Imaging

To obtain an initial estimate of the 3D shape of the lungs, after stereoscopic imaging, lungs were fixed and imaged using a Bruker SkyScan 1272, micro-CT scanner at a pixel resolution of 25 μm. The lungs were fixed by inflating the lungs with 2.5 % glutaraldehyde buffered with phosphate buffered saline solution, up to a pressure of 2450 Pa (25 cmH_2O). Tissue samples fixed in glutaraldehyde are extensively cross-linked, providing excellent ultrastructural stiffening that maintains the structure of the alveoli, enabling imaging with micro-CT [9]. This process was carried out after stereoscopic imaging, as cross-linking reactions of glutaraldehyde are largely irreversible [10].

The lungs were held at the fixation pressure for 24 h. After 24 h the lungs were attached to a regulated air source, which maintained an even pressure of 2450 Pa (25 cmH_2O) to air dry the fixed lungs. The result of this process was a dried lung lobe, with no living tissues, and with the structural proteins cross-linked to maintain the lung structures. An example of this can be seen in Fig 5.

The micro-CT image of the lung lobe, shown in Fig 5, enabled the creation of a mesh of the lung lobe. This process started with thresholding of the 2D images to create binary masks. Any holes in the masks were corrected manually. An ITK-based marching cubes algorithm was then implemented to convert each binary mask into a 3D isosurface, which was converted into a point cloud that represented the surface of the lungs from the micro-CT data. While some discrepancies were

introduced by the cross-linking procedure and shrinkage during the air-drying process, the mesh of the fixed lung generated from micro CT imaging provided a close approximation to the shape of the unfixed lung.

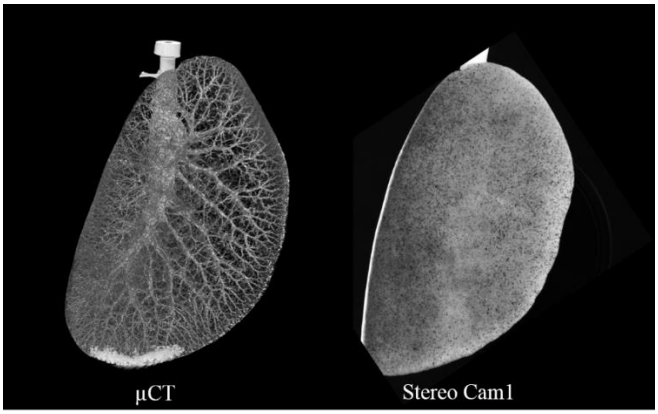

Fig 5. Left, Micro-CT of the fixed lung lobe. Right, view of fixed speckled lung from a single camera.

2.4 Improving Lung Surface Reconstruction and Tracking Motion

The dense point cloud created from the segmented micro-CT data described in Section 2.3 was aligned to the sparsely reconstructed laser line data acquired from the stereo rig described in Section 2.2.4 using a coherent point drift algorithm to rigidly translate, rotate, and scale the point cloud.

A quadratic Lagrange surface mesh was fitted to the aligned micro-CT point cloud using the fitting algorithms in GIAS2 [12], which minimises the weighted sum of the projections of the point cloud onto the surface. The result of this procedure was an initial surface mesh that was aligned with the position of the stereo-imaged lung, as shown in Fig 6.

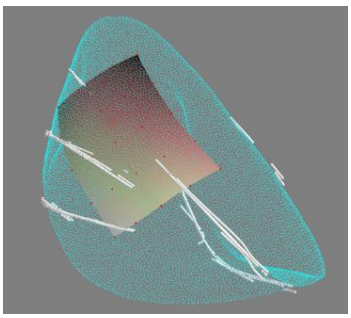

Fig 6. Fresh lung meshes. Laser line points are white. The micro-CT point cloud is green, and the quadratic patch Lagrange patch is gold to black.

A model-based reconstruction approach was then used to improve upon the initial reconstruction, by mapping texture information across camera views to generate a dense set of corresponding 3D points on the lung surface [11]. In this case, the micro-CT surface mesh was used as a prior model to aid reconstruction of the lung surface. This involved projecting pixels from a reference camera (in this case, Camera 1) onto the quadratic Lagrange micro CT surface mesh. These points were then backprojected to another camera's sensor (in this case, Camera 2) and resampled to generate a new image, which closely resembled the real view from Camera 2. Cross-correlation techniques were then used to identify corresponding points between the resampled image and the real image from Camera 2. These corresponding points were then triangulated to generate a 3D reconstruction of the surface. This operation requires knowledge of the positions of the cameras, which were found during the camera calibration procedure.

The lung surface was reconstructed in this manner at the same inflation pressure used for fixing the lung. The motion of the lung surface during subsequent inflation pressure steps was tracked by performing 2D cross-correlation of the reconstructed corresponding points across the images acquired from each individual camera. These tracked image points were then triangulated to provide a 3D surface reconstruction at each of the inflation pressures.

3 Results

3.1 Tracking of Intrinsic Features

One of the primary concerns with reconstructing and tracking the motion of the fresh lung lobes was the lack of surface texture. To test the ability of the 2D subpixel image registration code [13] to track the intrinsic features of the fresh lung lobe, tracking was performed on a single camera view of a lung across several pressure steps, as shown in Fig 7.

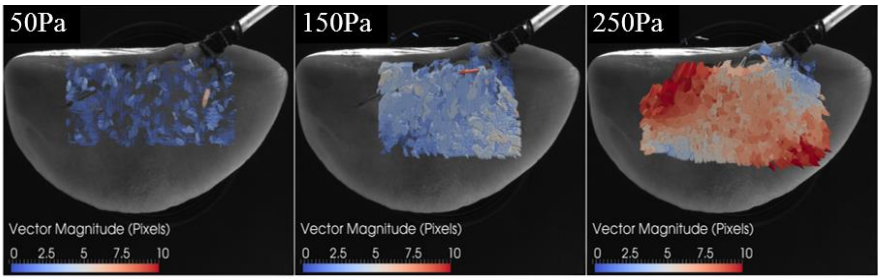

Fig 7. Single camera tracking of the intrinsic features of a left lung lobe. The pressure difference between the reference image and tracked image is shown in the top left.

Confidence thresholds [13] were set to remove points that did not have a strong correlation peak. Fig 7 illustrates that the subpixel image registration method is capable of tracking intrinsic features on the surface of the fresh lung. Failure of the

2D subpixel image registration algorithm would result in no or randomly oriented vectors being returned. The patchy, non-uniform pattern visible in Fig 7 is a result of the single camera tracking not having sufficient data to capture the displacements of the complex 3D surface of the lung.

3.1 3D Reconstruction Results

To test that reconstruction was effective on fresh lung, a region of interest (ROI) on the back of the lung, which had few specular reflections, was selected, as can be seen in Fig 8.

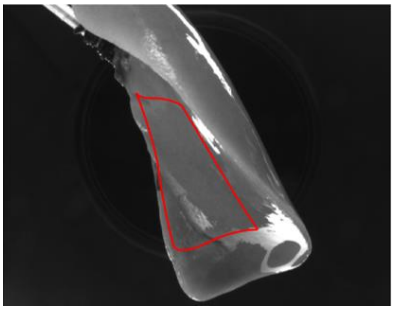

Fig 8. Region of interest for a reference camera selected on fresh lung. In the reference state the lung was inflated to 2069 Pa.

The model-based reconstruction approach described in Section 2.4 was then applied to determine corresponding points with the region of interest across the other cameras in the rig that could see the same region. For the selected ROI, two other cameras could see the same region. The resulting set of corresponding points were then triangulated to find their 3D locations, as seen in Fig 9.

The 3D locations of these points were then tracked across a range of inflation pressures. This resulted in a 3D deformation field, such as that seen in Fig 9 and Fig 10.

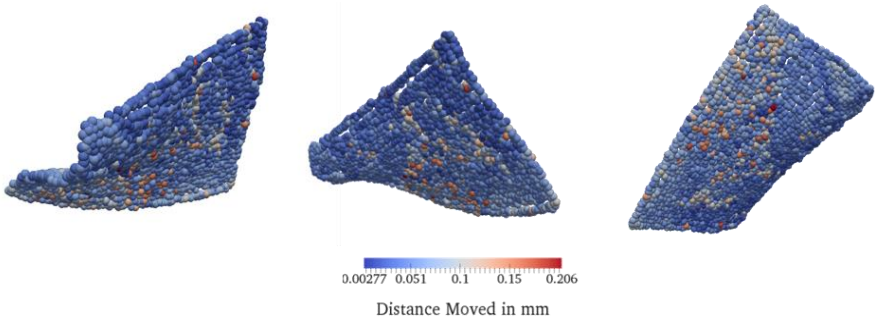

Fig 9. Reconstructed lung surface points displayed as spheres, coloured by displacement magnitude, viewed from three angles to display the surface curvature.

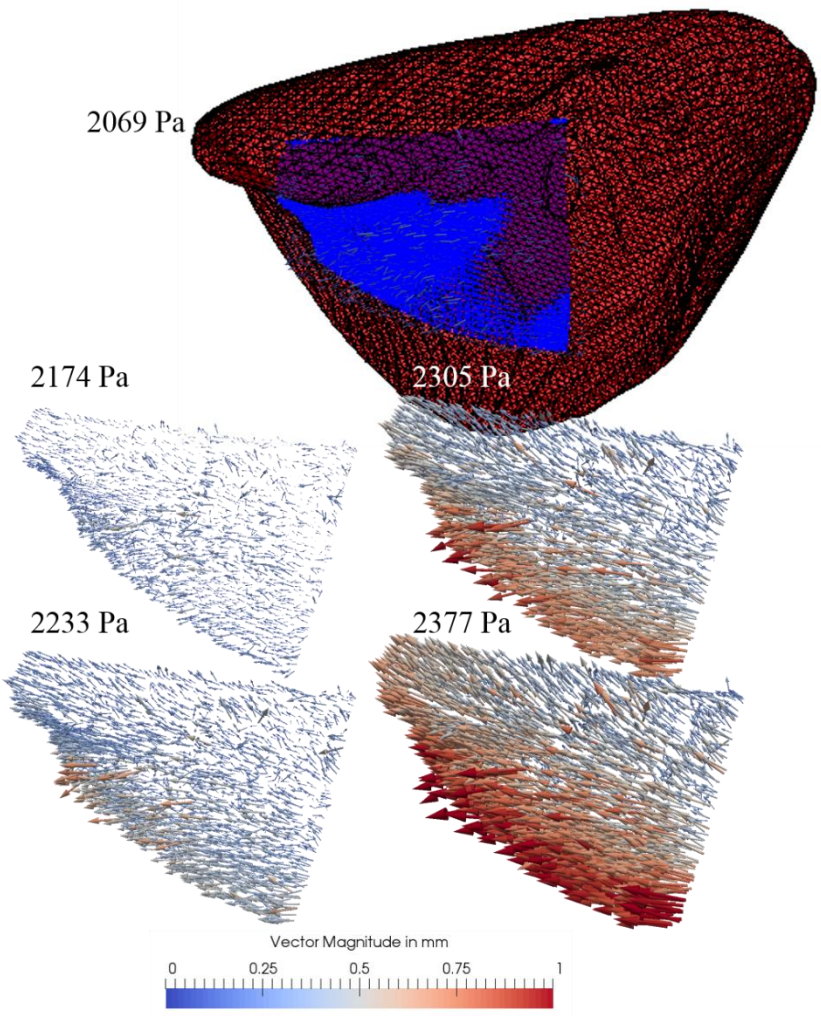

Fig 10. 3D location of the fresh lung surface tracked during inflation. The first frame is shown overlaid on the quadratic Lagrange mesh.

The 3D reconstruction of the fresh lung enabled tracking of the motion of the lung as a result of pressure increases. In this study, the fresh lung was tracked across a pressure change of 317 Pa. Over this range, the mean magnitude of the 3D motion (0.525 mm) was computed by determining the Euclidean distances between point positions at each pressure. Areas of non-uniformities in the displacement vectors are likely due failure to identify corresponding points across the three cameras. Spurious vectors could be eliminated by adjusting the cross-correlation confidence thresholds to be appropriate for 3D tracking.

4. Summary

This paper presents a pipeline for the reconstruction and tracking of the 3D motion of the *ex vivo*, intact, left lobe of a rat lung, as a result of changes in pressure. Model-based 3D reconstruction of the lungs enabled corresponding points to be found between camera views of the fresh lungs. From these, the 3D shape of a patch of the imaged lung could be determined.

The 3D reconstruction of the fresh lung patch in this study was completed with three cameras across 21 pressure steps, encompassing a total pressure change of 317 Pa. The 317 Pa pressure increase resulted in the total mean magnitude of the motion of the lung being 525.7 μm.

This study shows that the 3D reconstruction of the surface of the lungs, using only intrinsic features, is a viable approach to determine 3D shape. A prior 3D mesh was generated from a micro-CT reconstruction of a fixed lung. This mesh was aligned with sparse stereoscopic points identified using a combination of laser line identification and boundary identification on the fresh lung in the stereo-imaging rig. It was shown in this study that a combination of laser line and boundary point identification was sufficient to align the stereoscopic data with the mesh. A model-based reconstruction approach was then used to map texture information across camera views to generate a dense set of corresponding 3D points on the lung surface.

The reconstruction in this study focused on using three cameras to reconstruct a patch of the lung. This demonstrated the feasibility of using such a pipeline for the reconstruction and tracking of fresh lung tissue across a range of pressures without the need for additional surface markers.

The pipeline presented in this chapter represents the first stereoscopic imaging of *ex vivo* lungs. In addition, this work provides the first 3D tracking of the surface motion of the lungs using only intrinsic features.

As part of future work, we aim to extend the reconstruction to the whole lung, making use of all 12 cameras. This will enable 3D tracking of whole lung motion. From this, it will be possible to determine the volume change in the lung as a result of changes in pressure. This will, in turn, enable the assessment of the accuracy of the reconstruction, as volume change in the inflation system is directly measured. Future studies will apply these methods of measuring 3D deformations to identify and model the constitutive properties of the intact lung tissue.

Acknowledgments

The authors are grateful for financial support from the Royal Society of New Zealand Marsden Fund, the Medical Technologies Centre of Research Excellence, and the Auckland Bioengineering Institute.

References

[1] E. Roan and C. M. Waters, "What do we know about mechanical strain in lung alveoli?," *Am. J. Physiol. Lung Cell. Mol. Physiol.*, vol. 301, no. 5, pp. L625-35, Nov. 2011.

[2] J. C. Debes and Y. C. Fung, "Effect of temperature on the biaxial mechanics of excised lung parenchyma of the dog.," *J. Appl. Physiol.*, vol. 73, no. 3, pp. 1171–80, 1992.

[3] J. B. West, "History of respiratory mechanics prior to world war II," *Compr. Physiol.*, vol. 2, no. 1, pp. 609–619, 2012.

[4] W. Mitzner, "Mechanics of the lung in the 20th century," *Compr. Physiol.*, vol. 1, no. 4, pp. 2009–2027, 2011.

[5] L. Knudsen and M. Ochs, "The micromechanics of lung alveoli: structure and function of surfactant and tissue components The structural components for gas exchange," *Histochem. Cell Biol.*, vol. 150, pp. 661–676, 2018.

[6] J. S. Kerr, S. Y. Yu, and D. J. Riley, "Strain specific respiratory air space enlargement in aged rats," *Exp. Gerontol.*, vol. 25, no. 6, pp. 563–574, 1990.

[7] S. Richardson *et al.*, "Towards a Real-Time Full-Field Stereoscopic Imaging System for Tracking Lung Surface Deformation Under Pressure Controlled Ventilation," in *Computational Biomechanics for Medicine*, Cham: Springer International Publishing, 2019, pp. 119–130.

[8] A. HajiRassouliha, "A Toolbox for Precise and Robust Deformation Measurement," 2017.

[9] C. C. W. Hsia, D. M. Hyde, M. Ochs, E. R. Weibel, and ATS/ERS Joint Task Force on Quantitative Assessment of Lung Structure, "An Official Research Policy Statement of the American Thoracic Society/European Respiratory Society: Standards for Quantitative Assessment of Lung Structure," *Am. J. Respir. Crit. Care Med.*, vol. 181, no. 4, pp. 394–418, Feb. 2010.

[10] I. Eltoum, J. Fredenburgh, R. B. Myers, and W. E. Grizzle, "Introduction to the Theory and Practice of Fixation of Tissues," *J. Histotechnol.*, vol. 24, no. 3, pp. 173–190, 2013.

[11] T. P. Babarenda Gamage, "Constitutive parameter identifiability and the design of experiments for applications in breast biomechanics," The University of Auckland, 2016.

[12] J. Zhang, J. Hislop-Jambrich, and T. F. Besier, "Predictive statistical models of baseline variations in 3-D femoral cortex morphology," *Med. Eng. Phys.*, vol. 38, no. 5, pp. 450–457, May 2016.

[13] A. HajiRassouliha, A. J. Taberner, M. P. Nash, and P. M. F. Nielsen, "Subpixel Phase-based Image Registration Using Savitzky-Golay Differentiators in Gradient-Correlation," *Comput. Vis. Image Underst.*, vol. 170, no. 170, pp. 28–39, 2018.

A Flux-Conservative Finite Difference Scheme for Anisotropic Bioelectric Problems

George C. Bourantas[1], Benjamin F. Zwick[1], Simon K. Warfield[2], Damon E. Hyde[2], Adam Wittek[1], Karol Miller[1]

[1]Intelligent Systems for Medicine Laboratory, School of Mechanical and Chemical Engineering, The University of Western Australia, 35 Stirling Highway, Perth, WA 6009, Australia
[2]Computational Radiology Laboratory, Children's Hospital Boston, and Harvard Medical School, 00 Longwood Ave., Boston, MA 02115, USA

Abstract

We present a flux-conservative finite difference (FCFD) scheme for solving inhomogeneous anisotropic bioelectric problems. The method applies directly on the raw medical image data without the need for sophisticated image analysis algorithms to define interfaces between materials with different electrical conductivities. We demonstrate the accuracy of the method by comparison with analytical solution. Results for a patient-specific head model highlight the applicability of the method.

Keywords: Flux-Conservative Finite Difference, Anisotropic electrical conductivity, Bioelectric field, Epilepsy

1 Introduction

Epilepsy is a neurological condition of recurrent or unprovoked seizures that is thought to affect 1% of children [1]. Antiepileptic drugs serve as the primary treatment [2]. Treatment strategy relies on two key issues. First, the quality of life of an epileptic patient fails to improve until the permanent cessation of seizures. Second, one third of patients experience drug resistance [2, 3]. Surgery to remove or alter the region of the brain where seizures originate is recommended to patients who fail to respond to antiepileptic drug therapy [4].

Around 100,000-500,000 patients in the United States of America with drug-resistant epilepsy are surgical candidates each year [2]. However, due to the high risk associated with the surgical procedure, less than 1% of patients are treated this way [2]. For surgical epileptic seizure management, there are two realistic options available: focal resection; or disconnection of the epileptogenic cortex [3]. Of these two options, only complete focal resection of the epileptic lesion offers the possibility of eliminating seizures.

Success of the surgical intervention depends on the ability to accurately identify the seizure onset zone (SOZ), which is to be resected. Intracranial electrodes help to identify the SOZ and map eloquent areas of the brain [6]. Currently, the clinical standard for identifying the SOZ are invasive electroencephalography (iEEG) grids and strips, or stereo-EEG (sEEG) electrodes, deployed stereotactically through holes in the skull [5]. The iEEG or sEEG data recorded during the day is collected and manually interpreted by expert neurophysiologists to identify the electrode(s) most implicated in seizure onset.

Patients (usually young) unable to tolerate conscious cortical mapping for resection are candidates for intracranial electrode-mediated extra-operative mapping [3]. The aim of this mapping is to identify the epileptogenic zone. This zone, which is characterized by low-voltage, fast-current neuronal activity, represents the minimum amount of cortex that must be resected to eliminate seizures [7]. Magnetic resonance images (MRIs) are routinely used to determine the

distribution of various tissue types throughout the brain. EEGs are used to localize the SOZ and the corresponding area of the brain, which is known as the eloquent cortex [8]. Following the initial MRI, patients undergo a craniotomy to implant intracranial EEG electrodes to the edges of the dura [3]. A low-resolution computed tomography (CT) scan is then used to locate the electrodes within the deformed brain [9].

Source localization of the epileptic zone can be enhanced using computational methods combined with the available imaging modalities. The pre-surgical planning capabilities for resection of the epileptogenic cortex will then be more accurate. Calculating the voltage distribution throughout a patient-specific head model is a key component of the forward problem of EEG source localization. The forward problem has been solved in previous studies using a pre-operative brain model [4, 7, 10-11]. However, a more efficient method for computing the voltage terms is required for patient-specific applications and efficient implementation into the clinical workflow. Previous studies employed finite element methods or boundary element methods to localize the epileptogenic source [12-14]. These methods, however, are limited by their dependence on meshes that sufficiently capture the discontinuity of electrical conductivities between the differing media within the head [15]. Another issue with mesh-based methods is their reliance on pre-determined boundary positions at patient-specific conductivity interfaces within the cortex. Although a high-quality mesh will provide a simple solution to the forward problem, it requires an experienced analyst, thereby decreasing the practicality of implementing this technology into clinical practice.

In this study, we apply the flux-conservative finite difference (FCFD) method to numerically solve the forward problem of EEG source localization. The bioelectric problem is described by a set of partial differential equations. FCFD method discretizes these equations into a system of linear algebraic equations. The numerical solution of the linearized system determines the electric potential distribution throughout a patient-specific conducting volume (head model). The FCFD method applies to the rectangular grid of material properties extracted from patient data. This eliminates image segmentation and meshing that is required in mesh-based methods. The conductivity assigned to each node is used to form a system of linear equations that is then solved to compute the voltage term. We apply an anisotropic tensor for the electrical conductivity. We solve a simple problem with analytical solution to highlight the accuracy of the proposed scheme before applying it to a patient-specific head model of an epilepsy patient.

2 Methods

2.1 Electromagnetic Modeling Using the Flux-Conservative Finite Difference Method

2.1.1 Governing equations

Source localization methods usually use a linear model, often called leadfield matrix, to correlate measured electrode voltages to their cerebral current sources. Computing the leadfield matrix requires the numerical solution of Maxwell's equations within the head (conducting medium). Since the frequencies employed for EEG are typically less than 100 Hz, transient signals are negligible, and the quasi-static approximation can be employed [4]. Therefore, the relationship between current sources and the induced voltage field is given as:

$$\nabla \cdot \left(\bar{\bar{\sigma}}(\boldsymbol{x}) \nabla \Phi(\boldsymbol{x})\right) = \nabla \cdot \boldsymbol{J}(\boldsymbol{x}) \tag{1}$$

with $\Phi(\boldsymbol{x})$ being the voltage potential at location $\boldsymbol{x}$ in the spatial domain Ω, $\bar{\bar{\sigma}}(\boldsymbol{x})$ the spatially varying conductance of the volume, and $\boldsymbol{J}(\boldsymbol{x})$ the current source density at the nodes of the volume. The inhomogeneous conductivity tensor $\bar{\bar{\sigma}}(\boldsymbol{x})$ can be represented by a 3×3 matrix as

$$\bar{\bar{\sigma}}(\boldsymbol{x}) = \begin{bmatrix} \sigma_{xx} & \sigma_{xy} & \sigma_{xz} \\ \sigma_{yx} & \sigma_{yy} & \sigma_{yz} \\ \sigma_{zx} & \sigma_{zy} & \sigma_{zz} \end{bmatrix} \tag{2}$$

while the left-hand side of Eq. (1) in its expanded form is given as

$$\begin{aligned} \nabla \cdot \left(\bar{\bar{\sigma}}(\boldsymbol{x})\nabla\Phi(\boldsymbol{x})\right) = & \frac{\partial}{\partial x}\left(\sigma_{xx}\frac{\partial\Phi}{\partial x} + \sigma_{xy}\frac{\partial\Phi}{\partial \mathrm{y}} + \sigma_{xz}\frac{\partial\Phi}{\partial z}\right) + \\ & \frac{\partial}{\partial y}\left(\sigma_{yx}\frac{\partial\Phi}{\partial x} + \sigma_{yy}\frac{\partial\Phi}{\partial \mathrm{y}} + \sigma_{yz}\frac{\partial\Phi}{\partial z}\right) + \\ & \frac{\partial}{\partial z}\left(\sigma_{zx}\frac{\partial\Phi}{\partial x} + \sigma_{zy}\frac{\partial\Phi}{\partial \mathrm{y}} + \sigma_{zz}\frac{\partial\Phi}{\partial z}\right) \end{aligned} \tag{3}$$

Using the Taylor series expansion and applying the flux-conservative finite difference scheme we can compute the spatial derivatives of Eq. (3). In the FCFD method, we can efficiently and accurately deal with the anisotropy and the discontinuities in the electrical conductance of the different materials (e.g. bone, soft tissue) in the brain. In the FCFD method we do not apply the chain rule in the computation of the spatial derivatives in Eq. (3), instead we treat the terms in the parenthesis for the spatial derivatives $\frac{\boldsymbol{\partial}}{\boldsymbol{\partial x}}, \frac{\boldsymbol{\partial}}{\boldsymbol{\partial y}}, \frac{\boldsymbol{\partial}}{\boldsymbol{\partial z}}$ as the unknow field functions. Therefore, the typical methodology applied in the classical FD methods is extended to account for the anisotropy of the field variables.

2.1.2 Flux-Conservative Finite Difference Method

The FD method works efficiently on Cartesian grids (that can be directly obtained from DICOM images) and computes the nonlinear convective term $\nabla \cdot \left(\bar{\bar{\sigma}}(\boldsymbol{x})\nabla\Phi(\boldsymbol{x})\right)$ by applying a flux-conservative scheme. All Flux-Conservative FD formulations give a nodal equation for the potential field $\Phi(\boldsymbol{x})$ at each node of the grid. The nodal equations finally form a linear algebraic system which can be solved using direct or iterative solvers (for FD method several robust solvers exist).

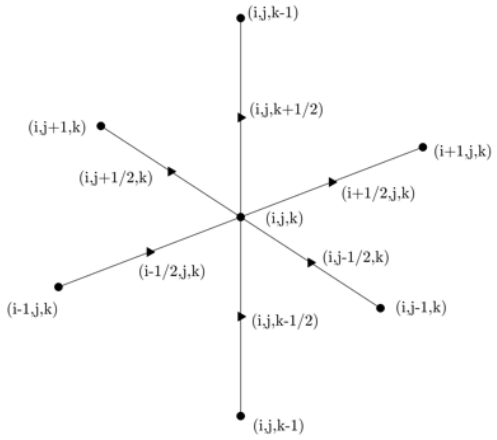

Fig. 1. The 3D stencil configuration used in the flux-conservative finite difference method.

This scheme computes spatial derivatives for the electric field using the stencil defined in Fig. 1. This is identical to the classical FD stencil except that in the FCFD stencil, fluxes in the fictitious grid points ((i+1/2,j), (i-1/2,j), (i,j+1/2), (i,j+1/2)) are preserved. Computation of the diffusion term at the grid points ((i,j), (i-1,j), (i,j+1), (i,j+1), (i,j-1)) will

lead to an erroneous non-conservative FD formulation. Application of classical (non-conservative) FD stencil by directly applying the chain rule to compute the spatial derivatives of the convective term will lead to incorrect calculation of fluxes.

Using the flux conservative approach, the terms at the central node (i,j,k) of the stencil shown in Fig.1 can be written (for the x coordinate) as

$$\frac{\partial Q^x}{\partial x} = \frac{Q^x_{\left(1+\frac{1}{2},j,k\right)} - Q^x_{\left(1-\frac{1}{2},j,k\right)}}{h_x} \tag{4}$$

where

$$Q^x = \sigma_{xx}\frac{\partial \Phi}{\partial x} + \sigma_{xy}\frac{\partial \Phi}{\partial \mathrm{y}} + \sigma_{xz}\frac{\partial \Phi}{\partial z} \tag{5}$$

We compute the terms $\sigma_{xx}, \Phi_{,x}, \sigma_{xy}, \Phi_{,y}, \sigma_{xz}$ and $\Phi_{,z}$ on the off-grid nodes $\left(i+\frac{1}{2},j,k\right)$ and $\left(i-\frac{1}{2},j,k\right)$. The electrical conductance $\sigma_{xx}, \sigma_{xy}, \sigma_{xz}$ values are not defined on the off-grid nodes. Instead, they are computed using interpolating/approximating methods such as arithmetic averaging of the known values for the electrical conductance on the grid nodes, or the harmonic average. The former applies for the case of the σ_{xx} electrical conductance (the same applies for σ_{xy} and σ_{xz}) as

$$\sigma_{xx_{\left(i+\frac{1}{2},j,k\right)}} = \frac{\sigma_{xx_{(i+1,j,k)}} + \sigma_{xx_{(i,j,k)}}}{2} \tag{6}$$

while the latter is written as

$$\sigma_{xx_{\left(i+\frac{1}{2},j,k\right)}} = \frac{2\sigma_{xx_{(i+1,j)}}\sigma_{xx_{(i,j)}}}{\sigma_{xx_{(i+1,j)}} + \sigma_{xx_{(i,j)}}} \tag{7}$$

The two approaches, despite their success in delivering reliable results, may result in decreased accuracy for the numerical solution when steep gradients in material properties (higher than 6 orders of magnitude) are present. This is because only the two nodes adjacent to the fictitious point are used in the computation, disregarding all the other nodes in the close vicinity. High order methods can be used to provide more accurate results but these increase the computational cost.

Furthermore, we need to compute the spatial derivatives of the electrical potential $\Phi(\boldsymbol{x})$ on the off-grid nodes. The derivative $\Phi_{,x}$ on the $\left(i+\frac{1}{2},j,k\right)$ and $\left(i-\frac{1}{2},j,k\right)$ nodes is given as

$$\frac{\partial \Phi_{(i+1/2,j,k)}}{\partial x} = \frac{\Phi_{(i+1,j,k)} - \Phi_{(i,j,k)}}{h_x} \tag{8}$$

and

$$\frac{\partial \Phi_{(i-1/2,j,k)}}{\partial x} = \frac{\Phi_{(i,j,k)} - \Phi_{(i-1,j,k)}}{h_x} \tag{9}$$

The derivative $\Phi_{,y}$ on the $\left(i+\frac{1}{2},j,k\right)$ and $\left(i-\frac{1}{2},j,k\right)$ nodes is given as

$$\frac{\partial\Phi_{(i+1/2,j,k)}}{\partial y}=\frac{\Phi_{\left(i+\frac{1}{2},j+1/2,k\right)}-\Phi_{\left(i+\frac{1}{2},j-1/2,k\right)}}{h_y} \tag{10}$$

and

$$\frac{\partial\Phi_{(i-1/2,j,k)}}{\partial y}=\frac{\Phi_{\left(i-\frac{1}{2},j+1/2,k\right)}-\Phi_{\left(i-\frac{1}{2},j-1/2,k\right)}}{h_y} \tag{11}$$

where

$$\Phi_{\left(i+\frac{1}{2},j+1/2,k\right)}=\frac{\Phi_{(i,j,k)}+\Phi_{(i+1,j,k)}+\Phi_{(i+1,j+1,k)}+\Phi_{(i,j+1,k)}}{4} \tag{12}$$

$$\Phi_{\left(i+\frac{1}{2},j-1/2,k\right)}=\frac{\Phi_{(i,j,k)}+\Phi_{(i+1,j,k)}+\Phi_{(i+1,j-1,k)}+\Phi_{(i,j-1,k)}}{4} \tag{13}$$

$$\Phi_{\left(i-\frac{1}{2},j+1/2,k\right)}=\frac{\Phi_{(i,j,k)}+\Phi_{(i,j+1,k)}+\Phi_{(i-1,j+1,k)}+\Phi_{(i-1,j,k)}}{4} \tag{14}$$

$$\Phi_{\left(i-\frac{1}{2},j-1/2,k\right)}=\frac{\Phi_{(i,j,k)}+\Phi_{(i,j-1,k)}+\Phi_{(i-1,j,k)}+\Phi_{(i-1,j-1,k)}}{4} \tag{15}$$

Finally, the derivative $\Phi_{,z}$ on the $\left(i+\frac{1}{2},j,k\right)$ and $\left(i-\frac{1}{2},j,k\right)$ nodes is given as

$$\frac{\partial\Phi_{(i+1/2,j,k)}}{\partial z}=\frac{\Phi_{\left(i+\frac{1}{2},j,k+1/2\right)}-\Phi_{\left(i+\frac{1}{2},j,k-1/2\right)}}{h_z} \tag{16}$$

and

$$\frac{\partial\Phi_{(i-1/2,j,k)}}{\partial z}=\frac{\Phi_{\left(i-\frac{1}{2},j,k+1/2\right)}-\Phi_{\left(i-\frac{1}{2},j,k-1/2\right)}}{h_z} \tag{17}$$

where

$$\Phi_{\left(i+\frac{1}{2},j+1/2,k\right)}=\frac{\Phi_{(i,j,k)}+\Phi_{(i+1,j,k)}+\Phi_{(i+1,j+1,k)}+\Phi_{(i,j+1,k)}}{4} \tag{18}$$

Consequently, for computing the partial derivative with respect to x for the Q^x term, eight neighbors are involved. Figure 2 shows the grid nodes used in the computation of the term $\frac{\partial}{\partial x}\left(\sigma_{xx}\frac{\partial\Phi}{\partial x}+\sigma_{xy}\frac{\partial\Phi}{\partial y}+\sigma_{xz}\frac{\partial\Phi}{\partial z}\right)$.

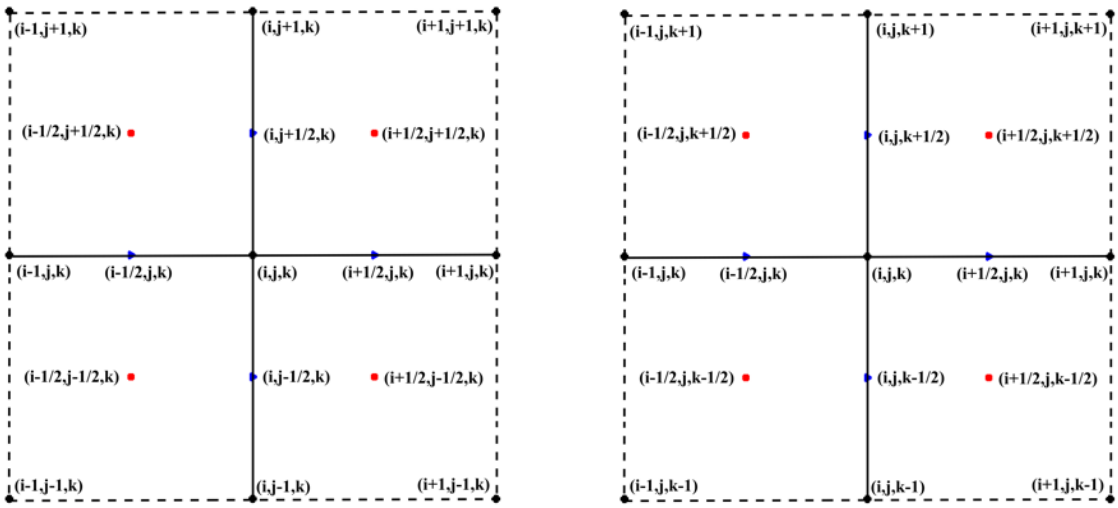

Fig. 2. The 3D stencil configuration used in the flux-conservative finite difference method.

The same procedure applies for the other two partial derivatives $\frac{\partial}{\partial y}\left(\sigma_{yx}\frac{\partial \Phi}{\partial x}+\sigma_{yy}\frac{\partial \Phi}{\partial y}+\sigma_{yz}\frac{\partial \Phi}{\partial z}\right)$ and $\frac{\partial}{\partial z}\left(\sigma_{zx}\frac{\partial \Phi}{\partial x}+\sigma_{zy}\frac{\partial \Phi}{\partial y}+\sigma_{zz}\frac{\partial \Phi}{\partial z}\right)$ in Eq. (3). Therefore, twenty-seven neighboring nodes form the stencil for computing the left-hand side in Eq. (1). The right-hand side ($\boldsymbol{\nabla}\cdot\boldsymbol{J}(\boldsymbol{x})$) is also defined on the grid nodes and can be defined as a continuous function, discretized over the nodes, or as point sources.

3 Results

3.1 Verification of the FCFD scheme

To demonstrate the accuracy of the proposed FCFD scheme we solve the Laplace equation for an inhomogeneous anisotropic medium in a unit volume box. The problem has an analytical solution of the form

$$\Phi(\boldsymbol{x}) = e^{x+y+z} \tag{19}$$

For an inhomogeneous anisotropic medium, the conductivity tensor giving the the analytical solution has the form

$$\bar{\bar{\boldsymbol{\sigma}}}(\boldsymbol{x}) = \begin{bmatrix} e^{x+y+z} & -0.25e^{x+y+z} & -0.75e^{x+y+z} \\ -0.25e^{x+y+z} & 1.5e^{x+y+z} & -1.25e^{x+y+z} \\ -0.75e^{x+y+z} & -1.25e^{x+y+z} & 2e^{x+y+z} \end{bmatrix} \tag{20}$$

We apply Dirichlet boundary conditions on the boundary nodes, according to the analytical solution (Eq. 19).

The linear system of the Laplace equation can be solved using direct or iterative solvers. The former are extremely accurate but have memory limitations, especially for 3D problems with large number of nodes. The latter do not always converge but are extremely efficient and have less computational cost compared to direct solvers. For the systems used in the present study, we use the minimum residual method, which applies to nonsymmetric systems. We used an Intel i7 quad core processor with 16 GB RAM for our simulations.

We compare the numerical solution against the analytical one using the Normalized Root Mean Square Error defined as $NRMSE = \frac{\sqrt{\frac{1}{N}\sum_{i=1}^{N}\left(u_i^{numerical} - u_i^{analytical}\right)^2}}{u_{max}^{analytical} - u_{min}^{analytical}}$. To study the convergence of the solution, we used successively denser grids starting from $51 \times 51 \times 51$ up to $201 \times 201 \times 201$.

Table 1. Maximum relative error and normalized root mean square error (NRMSE) for increasing grid resolution.

Grid resolution	Solution time (s)	L_∞	NRMSE
$51 \times 51 \times 51$	13	2.21×10^{-5}	2.13×10^{-6}
$101 \times 101 \times 101$	228	1.02×10^{-5}	7.08×10^{-7}
$201 \times 201 \times 201$	3363	6.72×10^{-6}	6.59×10^{-7}

The results (Table 1) suggest that both the maximum relative error and NRMSE will converge to zero as the number of nodes increases, confirming the accuracy of the FCFD scheme for solving anisotropic, three-dimensional, bioelectric field problems. Figure 3 shows the potential distribution computed by the analytical solution at plane z=0.5 and a histogram displaying the differences, node by node, of the numerical solution with the analytical one for a grid resolution of 101^3.

.

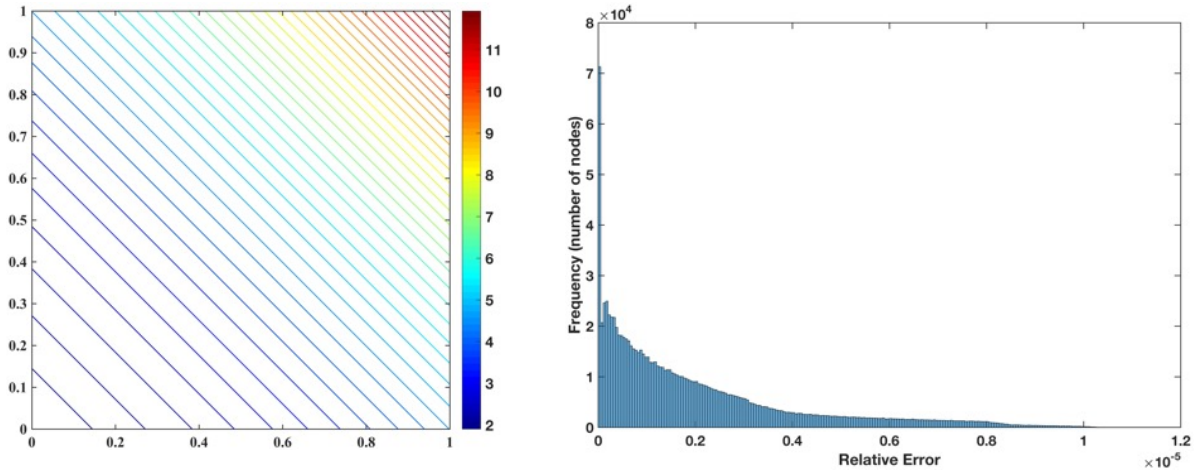

(a) **(b)**

Fig. 3. Axial view of the **(a)** numerical solution and **(b)** histogram of the differences with the analytical solution using the flux-conservative finite difference method for the for inhomogeneous anisotropic medium verification problem.

For source localization, the computational time needed to solve the forward problem is crucial because multiple forward problems must be solved. Therefore, the accuracy and efficiency provided from the proposed scheme makes it a strong candidate to be used in clinical practice.

3.2 Patient-specific head model

In this section, we apply the FCFD method to a patient-specific head model of a five-year old epilepsy patient. The electrical conductivities were extracted from the patient's diffusion-weighted MRI using the method described in [16]. A node was assigned to the corner of each voxel to create a $160 \times 192 \times 192$ grid comprised of 5,898,240 points. An anisotropic conductivity was assigned to all nodes inside the conducting volume. The three-dimensional finite difference brain volume was comprised of white and grey matter, as well as cerebrospinal fluid and air. We model air, grey

matter and cerebrospinal fluid conductivities using isotropic tensors, while white matter fibers were assigned anisotropic tensors. Using the Cartesian grid (voxels) directly from the raw data we avoid the need for image segmentation to assign constitutive properties.

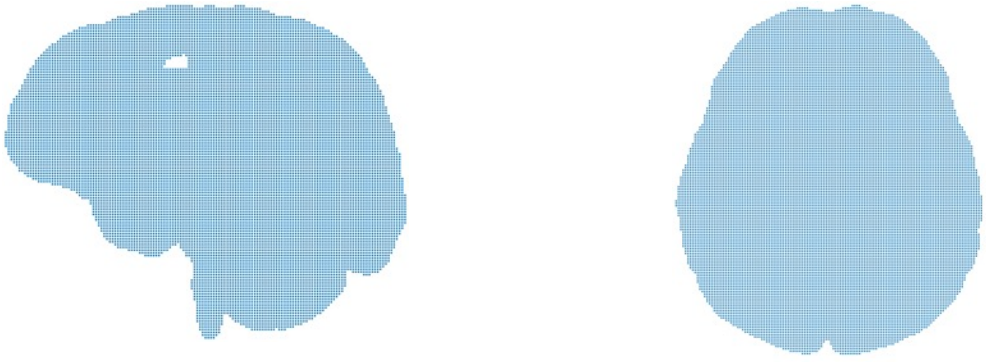

(a) **(b)**

Fig. 4. (a) Sagittal and **(b)** axial view of the brain raw data

We compute the electric potential distribution throughout the brain volume by applying the point electrode model. We selected electrodes as the source and sink. We apply a current of 1 A at the source, and we remove 1 A at the sink. In the presence of any external current source, Poisson's equation (Equation 10) governs the potential distribution within the head volume incorporating anisotropic conductivity. At the boundaries, we enforce Neumann boundary conditions (Equation 2). We numerically solve the linear system of equations using the minimum residual method. We model air using an isotropic conductivity of 10^{-9} (S/m), assigning this to all voxels outside of the head volume. This is demonstrated in Figures 5(a)-(c) as the voltage approaches zero outside the skull-air interface boundary.

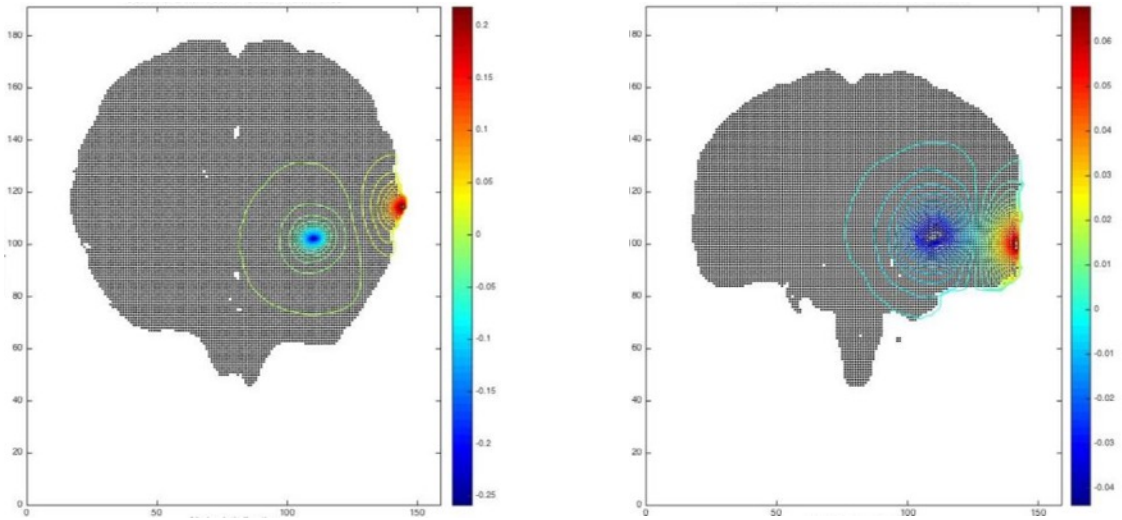

(a) **(b)**

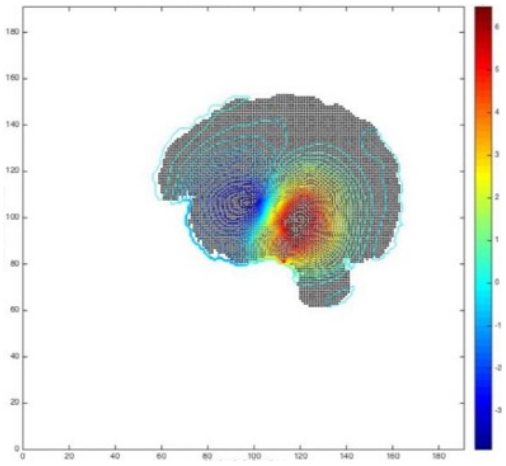

(c)

Fig. 5. Electric potential distribution throughout the brain in (a) axial plane 103, (b) coronal plane 108, and (c) sagittal plane 127.

Figure 5 shows the electric potential distribution throughout the brain in the axial, coronal and sagittal planes. These slices center around the midpoint of the preselected source/sink configuration to best illustrate the voltage distribution (we positioned the source at (143, 114, 101) and the sink at (110, 102, 104)). As expected, the source and sink generate a voltage inside the conducting volume that is greatest close to the corresponding electrodes and approaches zero as the distance from these regions increases.

4 Conclusion

In this study, we successfully applied the FCFD method to numerically solve the bioelectric problem to obtain the voltage distribution throughout the head. We first applied the FCFD method to a simple problem with an analytic solution. Following verification, the proposed scheme has been applied to a patient-specific head model (created using raw medical image data) to compute the electric potential distribution throughout the conducting volume for a specified source/sink configuration.

The accuracy of the patient-specific head model may be improved by using a complete electrode model instead of the point-electrode model used in the present study. The complete electrode model incorporates the size of the electrodes, their shape and the contact impedance, providing a better approximation of the electrode-tissue interface. With the point-electrode model, currents in the electrodes are not considered in the numerical solution. Therefore, the voltages close to the electrodes are of greater amplitude compared to those expected in real-world cases.

Successful application of the proposed scheme enhances current pre-surgical planning capabilities for resection of the epileptogenic cortex. In contrast to traditional mesh-based methods such as the finite element and boundary element methods, with our method there is no need for image segmentation and mesh generation.

5 Acknowledgements

This research was supported by the Australian Government through the Australian Research Council's *Discovery Projects* funding scheme (project DP160100714) and National Health and Medical Research Council Project Grant APP1162030

References

1. Devinsky, O.: Epilepsy: A patient and family guide, Demos Medical Publishing, New York (2007)
2. Ravindra, VM, Sweney, MT, Bollo, RJ: 'Recent developments in the surgical management of paediatric epilepsy', Archives of Disease in Childhood, vol. 102, no. 8, pp. 760-776 (2017).
3. Husain, AMMD Practical Epilepsy, 1st ed. edn, Springer Publishing Company, New York (2015).
4. Hyde, DE, Tomas-Fernandez, X, Stone, SS, Peters, J & Warfield, SK 2017, 'Localization of stereo-electroencephalography signals using a finite difference complete electrode model', in Engineering in Medicine and Biology Society (EMBC), 2017 39th Annual International Conference of the IEEE, IEEE, pp. 3600-3603.
5. Vega, R.A., Holloway, K.L., Larson, P.S.: Image-Guided Deep Brain Stimulation. Neurosurg Clin N Am 25, 159-172 (2014)
6. Hallez, H, Vanrumste, B, Grech, R, Muscat, J, De Clercq, W, Vergult, A, D'Asseler, Y, Camilleri, KP, Fabri, SG, et al. 2007, 'Review on solving the forward problem in EEG source analysis', Journal of NeuroEngineering and Rehabilitation, vol. 4, no. 1, pp. 46-75.
7. David, O, Blauwblomme, T, Job, A-S, Chabardès, S, Hoffmann, D, Minotti, L & Kahane, P 2011, 'Imaging the seizure onset zone with stereo-electroencephalography', Brain: A Journal of Neurology, vol. 134, no. 10, pp. 2898-2911.
8. Taimouri, V, Akhondi-Asl, A, Tomas-Fernandez, X, Peters, JM, Prabhu, SP, Poduri, A, Takeoka, M, Loddenkemper, T, Bergin, AMR, et al. 2014, 'Electrode localization for planning surgical resection of the epileptogenic zone in pediatric epilepsy', International journal of computer assisted radiology and surgery, vol. 9, no. 1, pp. 91-105.
9. Hermes, D, Miller, KJ, Noordmans, HJ, Vansteensel, MJ & Ramsey, NF 2010, 'Automated electrocorticographic electrode localization on individually rendered brain surfaces', Journal of neuroscience methods, vol. 185, no. 2, pp. 293-298.
10. Brodbeck, V, Spinelli, L, Lascano, AM, Wissmeier, M, Vargas, M-I, Vulliemoz, S, Pollo, C, Schaller, K, Michel, CM, et al. 2011, 'Electroencephalographic source imaging: a prospective study of 152 operated epileptic patients', Brain, vol. 134, no. 10, pp. 2887-2897.
11. Erem, B, Hyde, DE, Peters, JM, Duffy, FH & Warfield, SK 2017, 'Dynamic electrical source imaging (desi) of seizures and interictal epileptic discharges without ensemble averaging', IEEE transactions on medical imaging, vol. 36, no. 1, pp. 98-110.
12. Dannhauer, M, Lanfer, B, Wolters, CH & Knösche, TR 2011, 'Modeling of the human skull in EEG source analysis', Human brain mapping, vol. 32, no. 9, pp. 1383-1399.
13. Pursiainen, S, Lew, S & Wolters, CH 2016, 'Forward and inverse effects of the complete electrode model in neonatal EEG', Journal of neurophysiology, vol. 117, no. 3, pp. 876-884.
14. Rullmann, M, Anwander, A, Dannhauer, M, Warfield, SK, Duffy, FH & Wolters, CH 2009, 'EEG source analysis of epileptiform activity using a 1 mm anisotropic hexahedra finite element head model', NeuroImage, vol. 44, no. 2, pp. 399-410.
15. Hédou-Rouillier, V 2004, 'A finite difference method to solve the forward problem in electroencephalography (EEG)', Journal of Computational and Applied Mathematics, vol. 167, no. 1, pp. 35-58.
16. Tuch, DS, Wedeen, VJ, Dale, AM, George, JS & Belliveau, JW 2001, 'Conductivity tensor mapping of the human brain using diffusion tensor MRI', Proceedings of the National Academy of Sciences, vol. 98, no. 20, pp. 11697-11701.